

Institute for Molecules and Materials

Alexander Dolgikh

RADBOUD UNIVERSITY PRESS

Radboud Dissertation Series

Alexander Dolgikh

Alexander Dolgikh

#### Radboud Dissertation Series

ISSN: 2950-2772 (Online); 2950-2780 (Print)

Published by RADBOUD UNIVERSITY PRESS Postbus 9100, 6500 HA Nijmegen, The Netherlands www.radbouduniversitypress.nl

Design: Proefschrift AIO | Guus Gijben Cover: Proefschrift AIO | Guus Gijben

Printing: DPN Rikken/Pumbo

ISBN: 9789465151595

DOI: 10.54195/9789465151595

Free download at: https://doi.org/10.54195/9789465151595

© 2025 Alexander Dolgikh

# RADBOUD UNIVERSITY PRESS

This is an Open Access book published under the terms of Creative Commons Attribution-Noncommercial-NoDerivatives International license (CC BY-NC-ND 4.0). This license allows reusers to copy and distribute the material in any medium or format in unadapted form only, for noncommercial purposes only, and only so long as attribution is given to the creator, see http://creativecommons.org/licenses/by-nc-nd/4.0/.

Proefschrift ter verkrijging van de graad van doctor

aan de Radboud Universiteit Nijmegen

op gezag van de rector magnificus prof. dr. J.M. Sanders,

volgens besluit van het college voor promoties

in het openbaar te verdedigen op

vrijdag 24 oktober 2025 om 10.30 uur precies

door

Alexander Dolgikh geboren op 17 maart 1995 te Moskou (Rusland)

#### **Promotor:**

Prof. dr. A.V. Kimel

### Manuscriptcommissie:

Prof. dr. P.C.M. Christianen

Prof. dr. A. Stupakiewicz (Uniwersytet w Białymstoku, Polen)

Dr. M. Guimaraes (Rijksuniversiteit Groningen)

# **Table of Contents**

Preface	11
CHAPTER 1	
Introduction	17
1.1 State-of-the-art magnetic data storage	18
1.2 Magnetic order	20
1.2.1 Magnetism of atoms	20
1.2.2 Magnetic order and magnetic anisotropy at the atomic level	23
1.2.3 Macrospin approximation	25
1.3 Spin dynamics	28
1.3.1 Ferromagnets	28
1.3.2 Antiferromagnets	30
1.4 Ultrafast magnetism	31
1.4.1 Femtosecond laser pulse as an ultrafast heater	31
1.4.2 Femtosecond laser pulse as an effective magnetic field	32
1.5 Magnetization switching in ferrimagnetic dielectrics	35
1.5.1 Heat-assisted magnetic recording in iron garnet	35
1.5.2 Non-thermal magnetic recording	37
1.6 Open questions and the scope of the thesis	37
Literature	40
CHAPTER 2	
Experimental techniques	45
2.1 Physical principles of optical probing of magnetism	46
2.1.1 Malus' law. Birefringence and dichroism	46
2.1.2 Magneto-optical Faraday effect	48
2.2 Detection methods	51
2.2.1 Magneto-optical imaging	51
2.2.2 Balanced photodetector	53

2.3 Principles of time-resolved measurements	55
2.3.1 Single-shot imaging	56
2.3.2 Pump-probe technique	57
2.4 Double-pump excitation	61
2.5 Experiment Automation	62
Literature	68
CHAPTER 3	
Magneto-optical diffraction of visible light as a probe of nanoscale	
displacement of domain walls at femtosecond timescales	71
3.1 Motivation	72
3.2 Sample	74
3.3 Magneto-optical diffraction	75
3.3.1 Diffraction on a single domain pair	75
3.3.2 Periodic one-dimensional domain pattern as a phase grating	78
3.4 Experimental details	81
3.5 Results and discussion	85
3.6 Conclusions	89
Literature	90
CHAPTER 4	
Ultrafast heat-assisted magnetization dynamics in	
ferrimagnetic insulator	95
4.1 Motivation	96
4.2 Sample	97
4.3 Experimental details	97
4.4 Experimental results	101
4.5 Discussion	109
4.6 Conclusions	113
Literature	115

### CHAPTER 5

rare-earth orthoferrite	119
5.1 Motivation	120
5.2 Sample	123
5.3 Experimental details	126
5.4 Experimental results	127
5.5 Discussion	132
5.6 Conclusions	141
Literature	142
CHAPTER 6	
All polarization dependence of all-optical control on magnetization	
reorientation in (SmTb)FeO <sub>3</sub>	145
6.1 Motivation	146
6.2 Measurement methods	147
6.3 Spin dynamics triggered by a single linear polarized pump pulse	149
6.4 Spin dynamics triggered by circular and linear polarized pumps	152
6.5 Controlling spin reorientation with a linearly polarized pulse	155
6.6 Discussion	157
6.7 Full coherent control of SRT with polarized pulses	158
6.7.1 Experimental data	158
6.7.2 Discussion	161
6.8 Spin dynamics beyond the principle of superposition	162
6.9 Conclusions	166
Literature	168
Summary	173
Samenvatting	177
Research Data Management	183

List of Publications	185
Curriculum Vitae	187

# Preface

My academic journey is coming to an end. This manuscript represents a collection of snapshots of the main projects that shaped my PhD trajectory. Looking at this work, I realize that a PhD requires one to be a director, an actor, and in the end a videographer of one's own dissertation. I am glad that my passion for filming and the experimental direction of my research (imaging) resonated so well with each other. Now I can say that I do not only practice high-speed photography, but also ultrafast photography.

Alexey Kimel, my supervisor, thank you for this. When I first arrived in Nijmegen, I did not know exactly what I wanted to do. Thanks to you, my research became closely connected with my hobby. In our conversations I learned to be more self-aware, and now I greatly value this soft skill. I deeply appreciate that you allowed me to join your group despite my initially modest experimental skills, and gave me the chance to learn how the laboratory works and to carry out projects independently. Now, at the end of my PhD, I can confidently say that I have excellent experimental skills and feel completely at home in the lab. I also hope to gain the same level of confidence in writing scientific articles and proposals. I clearly see how many opportunities for growth I have, and I am grateful for your support throughout my PhD. Even though major changes in the world happened during these years, with your support I was able to attend many conferences, present my data, and explore related research areas. I believe that live communication is not only essential, but also one of the most engaging parts of science.

The writing of this manuscript involved not only me and my supervisor, but also many people who, in one way or another, participated in my research and supported me during my work. I want to thank you all, and I hope I will not forget to mention anyone.

Marilou de Wit, you cannot imagine how many times problems seemed unsolvable until I explained them to you. University work often requires following established bureaucratic procedures, and I was immensely grateful that they always seemed to pass me by, I just had to say, "I forgot," and it was resolved. Sometimes I feel that without your help, I could not have prepared for my defense. Your kindness and responsiveness make you truly the jewel of this group.

I also want to thank the technicians, who not only helped in the laboratory but also taught me, broadening my perspective in working with equipment. I was able to automate my experiments largely thanks to Sergey Semin, who encouraged me to

study our instruments in detail. My hardware and automation skills now occupy a proud place in my CV. Chris Berkhout, thank you for your kindness and responsiveness. Thanks to you, I could look at obstacles and delays in the lab with more ease. Kamyar Saeedi Ilkhchy, you joined the group toward the end of my projects, and we did not have the chance to work together. I sometimes regret this. because I think we would have made a good team.

I am grateful to all my colleagues - many of you helped me with my projects, supported me, and explained things. Kihiro Yamada, the multipump master, it was with you that I first started ultrafast pump-probe experiments. Kiran Prabhakara, I shared the optical table with you, and it was always easy to reach agreement. Fabio Formisano, you seemed to be the most cheerful PhD student I met, and you lifted everyone's spirits. Oiao Li, you always came to help and explained cryogenics to me.

Together with Theo Rasing I worked on one of the articles; he showed me how to phrase my thoughts more concisely and how to describe even unusual experiments clearly. Johan Mentink, I will always remember that data should be stored in the group repository. I hope that in the end I did it properly.

Kirill Grishunin, I was glad to meet you. We not only shared a sense of humor but also worked well together. You revealed to me the secret of how to handle an infinite loop inside another infinite loop in my programs. Now I understand how to use such loops and exit them when necessary, although I also enjoy writing shorter and cleaner code.

Evgeny Mashkovich, I respect the diligence and precision with which you approach your work. You will always remain for me an example of a true scientist. I am also happy to know Kseniya and your children. Board games with you are always in my heart, just as much as the times when we moved large pieces of furniture together.

Anna Gatilova, although our time in the group did not overlap for very long, our friendship more than made up for it. I was very happy at how quickly we connected, though I was nervous in my first year when you asked me to be your paranymph. Matthias Salewski, although we did not work together, my PhD memories will always be connected with you as well.

Xinyue Li, our PhD trajectories were very similar. We started almost at the same time, and soon after COVID locked us at home. Like me, you had a son during this period. We both took a bit longer with our defenses and are now reaching the finish line at nearly the same moment.

In our group, imaging was not only my field – Kshiti Mishra, I always admired your diligence and concentration in finding the perfect alignment of objective and camera, even under the most difficult conditions.

Nikolai Khokhlov, I wish our career paths had crossed earlier. You master many difficult subjects and explain them clearly. I am also glad that we found common ground outside the lab and became friends. Timur Gareev, I remember when you used to visit the group as a guest, and I am glad you later joined as a PhD. Like with Nikolai, we could always talk about our alma mater, and that gave us a shared approach to solving scientific problems.

Dmytro Afanasiev, your understanding of physical problems always impressed me. The flexibility you show in reaching your goals revealed to me how many possibilities exist, even in dead-end situations.

I also want to express my gratitude to the senior colleagues who finished their work in the group during my first year and with whom I had little time to collaborate: Rostislav, Anna, Carl, and Guido. And also to those who joined later: Lucas, Dinar, Victoria, and Vlad – good luck to you! Thomas Blank and Thomas Metzger, you both joined and completed your PhDs while I was still working on my projects, and by your example you showed me how quickly time passes.

It took me some time to find the right words to express my gratitude to Daria. Coming from the same university, we first met five years before my PhD. It was also with you that I did my guest research, which added another thread to our connection. Later we became friends, and the absence of joint projects never stopped us from meeting every year. Maxim, I also hope you will read this thesis and see your name. I am glad I met you, and I think that we often match in our views on life.

A PhD is a significant period of life, during which I met many people important to me. I want to thank you all, and I will be glad if you find your names when you open my thesis. Olga and Andrey, as well as Yulia and Nils. Being parents is difficult, and being expat parents is an order of magnitude harder. You helped me to enjoy my papa-days and not feel lonely with my children. Oliwia and Marchin, I was happy every time we could meet for a board game or a drink. Bektur, it was always interesting to talk with you and discuss physics or ps.

With great warmth I want to thank my family, who supported me throughout my PhD. My beloved Ira, I am very happy that we went through the PhD together. You were always there for me, always believing in me and supporting me. With you I could always discuss all the difficulties of the PhD. I believe that you fully understand the depth of physics - we regularly discussed it, and that always inspired me.

Daniel and Mihail, my children, I am so happy to have you. You were born while I was working on this manuscript. Every day with you is precious to me. I will be glad if, when you grow up, you can read these warm words about you in my thesis.

Мама и папа, спасибо за всё, что вы мне дали. Без вашей поддержки я бы не смог продвинуться так далеко в своих начинаниях. Спасибо за вашу заботу обо мне, а также о ваших внуках. Я счастлив тому, что я ваш сын. Бабушка и дедушка, я безмерно благодарен вам за поддержку с моих самых ранних лет. Я счастлив тому, что вы у меня есть и мне тепло на душе, когда я думаю о вас. Ангелина, сестрёнка, ты так сильно выросла за то время пока я занимался своим манускриптом. Я тебя люблю и очень рад тому, что ты навещала меня каждый год.

Dear Emma, thank you for your support and belief in me. I am happy for your love toward your grandchildren and for the help you gave us in caring for them. Johan, I am glad that we became family, and I am grateful for your openness and cheerfulness.

Dear committee members, thank you for taking the time to read and assess this thesis.

This thesis brings my PhD journey to a close, and I am proud to present it to its readers.

# CHAPTER 1

# Introduction

In this chapter, we discuss the primary reasons for studying ultrafast magnetic dynamics and the optical manipulation of magnetic order in magnetic materials in general and in magnetic dielectrics in particular. The chapter starts with a description of magnetism from the perspective of individual atoms and reviews the main types of magnetic ordering. We discuss the bi-directionality of the interaction between light and spins in magnetic media, leading to magneto-optical and optomagnetic effects, respectively. Lastly, we speculate about the possibilities for control magnetization in magnetic dielectrics with the help of light, highlight the state-of-the-art in the field, and formulate research questions for future studies. The formulated questions have practically become the research questions of this thesis.

## 1.1 State-of-the-art magnetic data storage

Almost every thesis on ultrafast magneto-optics begins with a mention of digital data storage. This focus isn't surprising given the increasing volumes of digital data humans produce every year. The demand for data storage solutions that surpass the speed and density of contemporary storage methods motivates the study of new mechanisms and scenarios allowing to write magnetic information on a storage medium. While many breakthroughs in condensed matter physics have been curiosity-driven, the field has also led to transformative technologies such as the transistor, the solid-state laser, the LED, and the solar cell. Today, with the widespread adoption of neural networks, rapid advances in data transmission, and the globalization of social media and entertainment platforms, fundamental studies of magnetism and condensed matter systems are more crucial than ever for the future of information processing.

Interestingly, the entertainment industry has become one of the major drivers behind the development of advanced big data storage technologies [1]. The demand for streaming high-bitrate content necessitates ever-increasing data readwrite speeds. The surge in consumer use of cloud technologies, especially for video storage, further underscores the need for vast storage capacities. Presently, the dominant methods for large data storage are hard disk drives (HDDs) and flash mainly solid-state drives (SSDs). The former electromechanical means of recording data, while the latter depends solely on electricity. Both methods, despite their advantages, come with significant limitations. The need to spin up HDD read-write heads hinders their speed. SSDs, while surpassing HDDs in speed due to the absence of mechanical movement, have a limited number of write cycles per bit. Current large data storage facilities rival the size of warehouses, and the demand for storage will only grow in the future.

In light of these challenges, numerous magnetic studies are funded with the goal of both increasing the read-write speeds and boosting storage density for future data repositories. One promising direction is the utilization of light instead of electricity for information read-write processes. The potential of such technology is indeed vast [2-4]. Challenges associated with traditional electric architectures stemming from von Neumann limitations might be circumvented by approaching read-write rates near that of optical telecommunication [5]. Although storage density using hard drives has reached impressive levels of 1 Tb/in<sup>2</sup> [6], the potential of optical recording technologies might increase this density by an order of magnitude or even more [7].

Heat Assisted Magnetic Recording (HAMR), employing a combined action of a magnetic field and light-induced heating for recording a single bit, is known as the most advanced data storage technology, which is about to enter the market [6-8]. Magnetic data storage, in general, employs magnets as a storage medium. A magnet with the north pole pointing "up" or "down" is considered as a bit storing "0" or "1", respectively. The magnetic poles are typically reversed with the help of an external magnetic field. In the state-of-the-art HAMR, the fields required to write a single bit are too high and practically cannot be generated at the scale of a commercial hard drive. Instead, the writing of a single bit is performed by a combined action of a moderate magnetic field and a laser-induced heating. When acting alone, such a magnetic field is unable to reverse the magnetization, but due to a partial destruction of the magnetic properties by laser-induced heating, magnetization reversal and magnetic writing become possible (see Fig. 1.1)

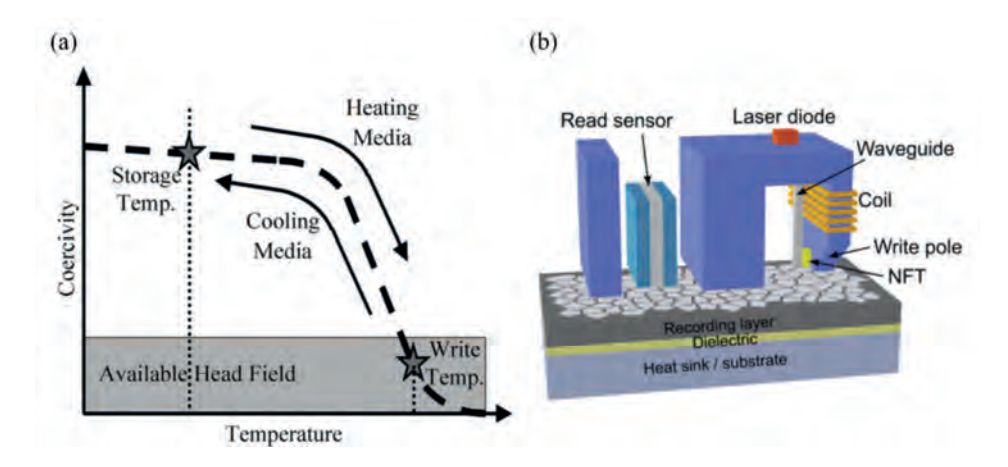


Fig. 1.1. (a) A schematic diagram of the HAMR write process (from [9]). (b) A schematic of the HAMR device. The laser radiation heats the recording layer locally. The coil generates a magnetic field of a given direction, re-magnetizing the heated area of the recording layer. The figure is from [7].

The state-of-the-art HAMR employs a metallic ferromagnet FePt as a storage medium. It is natural to ask if the storage media for HAMR can also be of a dielectric nature. For instance, since dielectrics lack free electrons, the thermal conductivity of magnetic dielectrics is known to be significantly lower than that of metals. Hence, heat locally deposited to write a magnetic bit will not spread to other bits, promising much higher recording densities in dielectric-based HAMR than in the case of metals. Moreover, in magnetic dielectrics, light can effectively control spins via mechanisms that do not rely on heat [10,11], and, as a matter of fact, even the heat-assisted mechanism of magnetic writing in magnetic dielectrics appears to be accompanied by far less dissipation than HAMR in metals [12]. It is also interesting how the process of HAMR is different for ferri- and antiferromagnetic media compared to that in ferromagnets. This thesis aims to answer these questions by focusing on studies of HAMR on antiferromagnetic and ferrimagnetic dielectrics.

### 1.2 Magnetic order

#### 1.2.1 Magnetism of atoms

To understand the nature of magnetism in solids, it is essential to comprehend its origin at the atomic level. Let's first consider a simplified atomic model with a positively charged nucleus at its center and a single electron in the orbit around it. This electron is said to have an orbital moment, which is quantized:

$$p_l = \hbar \sqrt{l(l+1)} \tag{1.1}$$

Where l = 1, 2..., (n-1) is the azimuthal quantum number, and n is the principal quantum number, which determines the number of the energy level of the electron. Different values of l correspond to different atomic orbitals: 0 - s, 1 - p, 2 - d, 3 - f, etc. As a consequence of Maxwell's equations, the movement of a charge (the electron) in its circular orbit results in the generation of a magnetic field. In classical theory, the angular momentum  $p_l$  of the charge is related to its magnetic moment  $\mu_l$  by the following relationship:

$$\mu_l = -\mu_B \frac{p_l}{\hbar}$$
 
$$|\mu_l| = \mu_B \sqrt{l(l+1)}$$
 (1.2)

The orbital magnetic moment of an electron is always oppositely directed to the orbital angular momentum. Overall, the ratio of the magnitude of the magnetic moment to the mechanical momentum in units of  $\mu_B/\hbar$  is termed the gyromagnetic ratio:

$$\frac{\mu_l}{p_l} = g \frac{\mu_B}{\hbar} \tag{1.3}$$

From equation (1.2), for the orbital magnetic and angular momenta of an electron, the dimensionless gyromagnetic ratio is equal to 1, i.e.,  $g_l = 1$ .

Additionally, each electron possesses an intrinsic angular momentum, unrelated to its motion as a whole, known as spin s. The electron's spin is equal to  $\frac{1}{2}$  and the corresponding angular momentum is  $p_s = \hbar \sqrt{s(s+1)}$ . Although the description of spin is not feasible in any classical model,  $p_s$  is a vector and can be added to other angular momenta using the corresponding rules. The intrinsic magnetic moment of the electron is related to the mechanical momentum by the gyromagnetic ratio:

$$\mu_s = -g_s \frac{\mu_B}{\hbar} p_s \tag{1.4}$$

The gyromagnetic ratio for the spin is 2 ( $g_s = 2$ ).

The projections of the orbital magnetic moment and the spin magnetic moment onto any chosen z-axis in space are quantized. In other words, a particle with a spin quantum number s and an orbital quantum number l can exist in one of (2s+1)(2l+1) states. Let's consider this with the example of a d-orbital (s =  $\frac{1}{2}$ , l = 2) in an external magnetic field (Fig. 1.2). The energy of interaction of the particle with the magnetic field is calculated as:

$$E = -\mu_0 \mu \cdot H_{\text{ext}} \tag{1.5}$$

In the case of spin, the energy is minimized if the spin is antiparallel with respect to the external magnetic field, i.e., the corresponding magnetic moment and the field are mutually parallel. To describe an atom, one must consider the contributions of all the electrons orbiting it, plus the magnetic moment of the nucleus  $\mu_N$ , meaning the magnetic moment of the atom is described as follows:

$$\mu = \sum \mu_{l_i} + \sum \mu_{s_i} + \mu_N \tag{1.6}$$

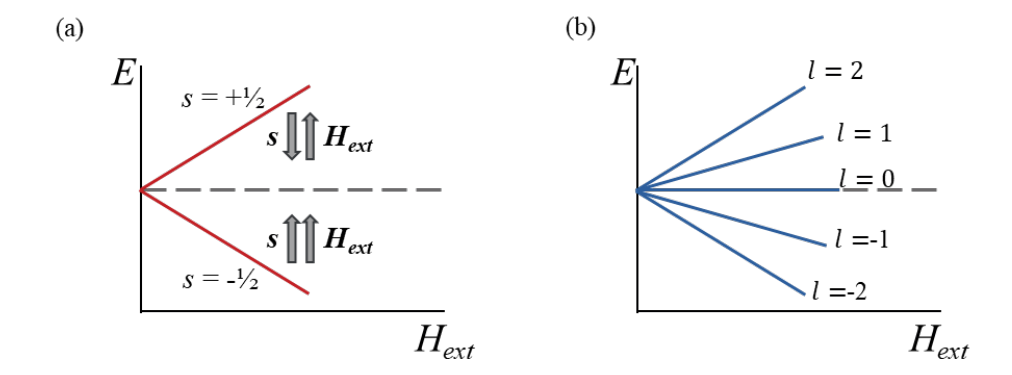


Fig. 1.2. Energy splitting of levels in an external magnetic field with different spin (a) and orbital quantum number (b).

In reality, the magnetic contribution from the nucleus is much weaker than that of the electrons and thus can be neglected.

The relationship between the total magnetic moment of the atom and its total angular momentum is expressed through the Lande g-factor:

$$\mu = g_{\rm J} \frac{\mu_B}{\hbar} p \tag{1.8}$$

Fully filled electron shells have zero net spin and hence do not contribute to the net magnetic moment (see Fig. 1.2(b)). Therefore, it is necessary to consider only partially filled electron shells.

For instance, in the periodic table, one can find quite a few elements with an unfilled electronic shell. Depending on the shell, it is conventional to talk about the 3d elements (Fe, Co, Ni, Mn, etc.), 4d elements (Y, Zr, Nb, Lu, etc.), 4f elements (Ce, Tb, Nd, Sm, etc.), 5d elements (W, Re, etc.), and 5f elements (Th, U, etc.). For instance, the Fe atom has a 1s<sup>2</sup>2s<sup>2</sup>2p<sup>6</sup>3s<sup>2</sup>3p<sup>6</sup>3d<sup>6</sup>4s<sup>2</sup> configuration. Despite the 3d subshell being partially filled and possessing an unbalanced magnetic moment, it is shielded by the filled 4s subshell. Nevertheless, in chemical compounds, the electronic configuration is modified. Iron oxide  $\alpha$ -FeO<sub>3</sub>, for instance, is one of the widespread magnets in nature. It consists of Fe<sup>3+</sup> ions and thus has a  $1s^22s^22p^63s^23p^63d^5$  configuration.

#### 1.2.2 Magnetic order and magnetic anisotropy at the atomic level

Fe, Co and Ni are typical elements in the periodic table which possess magnetic properties at room temperature. They can attract and repel other magnets and historically were called ferromagnets. Initially, ferromagnetism was attempted to be described by artificially introducing an internal magnetic field (Weiss field), which was generated by atoms of the magnetic elements. The origin of the field for a long time was unclear. However, after the discovery of spin, it was realized that electronelectron interaction is not only dependent on electrons' charges but also on their spins. A quantum mechanical explanation of such a spin-dependent interaction was independently proposed by Heisenberg and Frenkel in 1927-1928 [13]. Consider two particles with

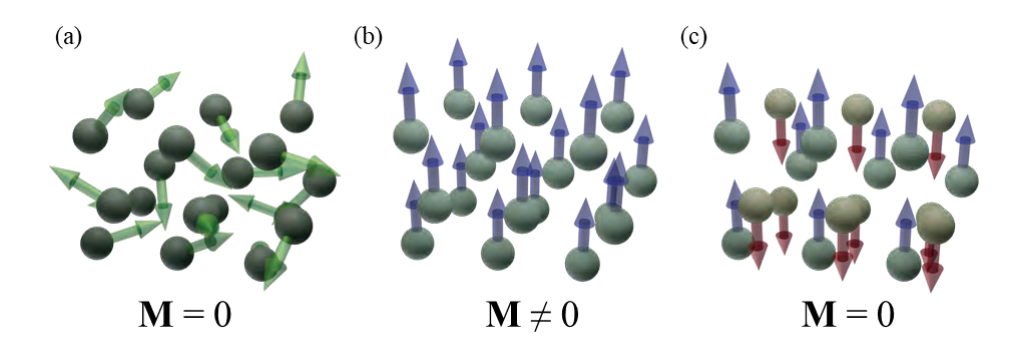


Fig. 1.3. Schematic demonstration of spin alignment in (a) paramagnetic, (b) ferromagnetic and (c) antiferromagnetic media.

spins  $\mathbf{S}_1$  and  $\mathbf{S}_2$ . It can be shown that the spin-dependent part of the Hamiltonian of their interaction is given by:

$$U_{12} = -2J_{12}\mathbf{S}_1\mathbf{S}_2 \tag{1.9}$$

where  $J_{12} = J(|\mathbf{r}_1 - \mathbf{r}_2|)$  is the exchange interaction integral, which depends on the position vectors of the two interacting electrons at positions  $\mathbf{r}_1$  and  $\mathbf{r}_2$ , respectively. The magnitude of the exchange integral rapidly decreases upon increasing the distance between the particles. The exchange interaction of multiple particles is described by the sum:

$$U_{\mathrm{ex}} = -2\sum_{i < k} J_{\mathrm{ik}} \mathbf{S}_i \cdot \mathbf{S}_k$$
 (1.10)

Hence, the exchange interaction favors the alignment of all the spins in the sample and thus forms a ferromagnet if  $J_{12} > 0$ . Interestingly, when  $J_{12} < 0$  the exchange interaction favors mutually antiparallel alignment of neighbouring spins. Such an exchange interaction results in a new type of magnets called antiferromagnets, which were hypothesized by L. Néel and discovered only in the 20<sup>th</sup> century [14]. These materials have no net magnetic moment and thus do not generate any magnetic fields. L. Néel also proposed the third class of magnets with antiferromagnetic exchange interaction, where two antiferromagnetically coupled spins are not equivalent  $|\mathbf{S}_1| \neq |\mathbf{S}_2|$  and thus the net magnetic moment is not equal to zero. These materials are called ferrimagnets.

In the Heisenberg model, the exchange interaction is considered isotropic, meaning it does not depend on the orientation of magnetic moments relative to the crystallographic axes. At the same time, in a magnetically ordered state, magnetic moments are often oriented along a specific crystal direction. The direction along which spins of magnets favour to align is called the easy axis. In order to tilt spins from this axis, one needs to overcome a potential barrier, the height of which is given by the energy of magnetic anisotropy. Typically, directions orthogonal to the easy axis are called hard axes. Sources of anisotropy include dipole-dipole interaction between the magnetic moments of atoms and spin-orbit interaction. In the first case, for two magnetic dipoles at a distance r from each other, the energy of dipole-dipole interaction is equal to [15]:

$$E_{
m dd} = \pm \frac{\mu_1 \mu_2}{r^3} (1 - 3\cos^2 \varphi)$$
 (1.11)

Where  $\varphi$  is the angle between the vector connecting the dipoles and the dipoles themself. Hence, if one considers a one-dimensional chain of magnetic dipoles and assumes that the dipoles are aligned ferromagnetically, dipole-dipole interaction favours aligning them along the chain, and the line connecting the dipoles in the chain becomes the "easy axis". If the dipoles are aligned antiferromagnetically, the dipole-dipole interaction favours an alignment orthogonal to the chain, and the chain direction turns into the "hard axis". The dipole-dipole interaction significantly contributes to the energy of magnetic anisotropy in rare-earth compounds.

Otherwise, the main source of magnetic anisotropy originates from spinorbit interaction.

#### 1.2.3 Macrospin approximation

Although nowadays, theories of magnets at the level of atoms and computational facilities are sufficiently advanced to facilitate ab-initio modelling of magnetic properties, "the perfect computation simply reproduces Nature, does not explain her" [16]. Understanding physical phenomena requires building simple and intuitive models, and for the latter, one needs to develop approximations. The macrospin approximation is probably the main approximation in modern magnetism [17]. In this approximation, ensembles of spins are treated as a single, collective entity. Consequently, the magnetization of the entire material can be regarded as a single uniform vector - a perspective well-suited for ferromagnets, where all spins in the ensemble have the same magnitude and are aligned:

$$\mathbf{M} = \frac{\sum \mathbf{S}_i}{V} \tag{1.12}$$

where V is the volume of the ferromagnet.

To describe more complex magnetic structures, such as antiferromagnets, one can divide the spin ensemble according to the spins' orientations. In the simplest case of an antiferromagnet with two sublattices, each sublattice is represented by its own macrospin  $\mathbf{M}_1$  or  $\mathbf{M}_2$ . The total magnetization of the antiferromagnet is then

$$\mathbf{M} = \mathbf{M}_1 + \mathbf{M}_2 \tag{1.13}$$

Using only the  ${f M}$  vector is obviously insufficient in magnets with different orientations or natures of spins. Such magnets are called multi-sublattice magnets. In particular, in the case of an antiferromagnet  $|\mathbf{M}_1| = |\mathbf{M}_2|$ ,  $\mathbf{M} = 0$ , but the corresponding physics is described in terms of antiferromagnetic Néel vector:

$$\mathbf{L} = \mathbf{M}_1 - \mathbf{M}_2 \tag{1.14}$$

Using the macrospin approximation greatly simplifies the description of magnetic phenomena in general and magnetic anisotropy in particular. For this, one employs the principles of thermodynamics and defines the equilibrium state of a magnet by defining the global minimum of its thermodynamic potential. Magnetic anisotropy contributes to the potential. In the case of a uniaxial magnetic anisotropy, the anisotropy energy can be represented as a series:

$$E_{\rm ani} = \sum k_i \sin^{2i} \alpha \tag{1.15}$$

Where  $k_i$  is the *i*-th anisotropy constants,  $\alpha$  is the angle between  $\mathbf{M}$  and the easy axis of magnetization. Usually, it is sufficient to consider only the first two terms of the series:

$$E_{\rm ani} = k_1 \sin^2 \alpha + k_2 \sin^4 \alpha \tag{1.16}$$

In this context, if  $k_1$  is greater than zero, the ferromagnet has an easy axis type of magnetic anisotropy, while if it is less than zero, the type of magnetic anisotropy is easy plane. In the case of antiferromagnets, the approach to defining the energy of anisotropy is similar, but it is necessary to consider the direction of magnetization for each sublattice. Additionally, when considering the rotation of the sublattice magnetizations, the exchange interactions must be taken into account. The energy of magnetic anisotropy can be written in the following way:

$$E_{\text{ani}} = k_1' \left( \sin^2 \alpha_a + \sin^2 \alpha_b \right) + k_2' \left( \sin^4 \alpha_a + \sin^4 \alpha_b \right) \tag{1.17}$$

Where  $\alpha_a$  and  $\alpha_b$  are the angles that the magnetizations of the sublattices make with the antiferromagnetic axis. If the sublattices are equivalent, we obtain an expression analogous to (1.16):

$$E_{\rm ani} = 2k_1' \sin^2 \alpha + 2k_2' \sin^4 \alpha$$
 (1.18)

This approach will be used in Chapter 6 for theoretical modelling of the spinreorientation transition in orthoferrites. During the spin-reorientation transition in rare-earth orthoferrites, the direction of the antiferromagnetic vector relative to the crystallographic axes depends on temperature. This dependence arises due to the temperature dependence of  $k_1^{'}=k_1^{'}(T)$ , while the coefficient  $k_2^{'}$  is assumed to be constant [18-20].

Finally, we would like to note that antiferromagnetic ordering doesn't automatically imply that the net spontaneous magnetization of the compound is zero. For instance, if the sublattices of an antiferromagnet are canted from a pure antiparallel state, the net magnetization is, obviously, non-zero  $\mathbf{M}_0 
eq 0$ (Fig. 1.4(a)). Canted antiferromagnets are different from ferrimagnets, where antiferromagnetically coupled sublattices have magnetizations of different magnitudes (Fig. 1.4(b)). Canted antiferromagnets, as well as ferrimagnets, exhibit the phenomenon of magnetic hysteresis and remanent magnetization and, on a macro scale, behave similarly to ferromagnets. The magnitude of the magnetic moment in each sublattice composing a ferrimagnet or an antiferromagnet typically varies with temperature. As sublattices of a ferrimagnet are different, the temperature dependencies of their magnetizations are also different. In particular, it is possible that at a certain temperature  $T_{
m M}$ , the magnetizations of the two sublattices cancel each other out. There also must be a point  $T_{
m A}$  at which the total angular momentum of the sublattices is zero. If the sublattices have different gyromagnetic ratios, these two temperatures are different  $T_{\rm M} \neq T_{\rm A}$  [21]. In this thesis, a ferrimagnetic material with a compensation point, iron garnet, and a canted antiferromagnet, rare-earth orthoferrite, are discussed.

In the case of a uniaxial crystal with non-zero magnetization, the minimum of the thermodynamic potential favours a splitting of the magnet into magnetic domains. If we consider a ferro-, ferri or canted antiferromagnet with uniform orientation of magnetization vector throughout its entire volume, such a magnet produces a stray field. The stray fields will also affect the magnet itself, interacting with its net magnetization. The energy of interaction can be minimized by dividing the magnet into opposite domains with magnetization vectors oriented in opposite directions. The size of the domains is defined by the interplay between the benefit in the magnetostatic energy and the loss in the energy required to form the wall between domains with opposite magnetization directions.

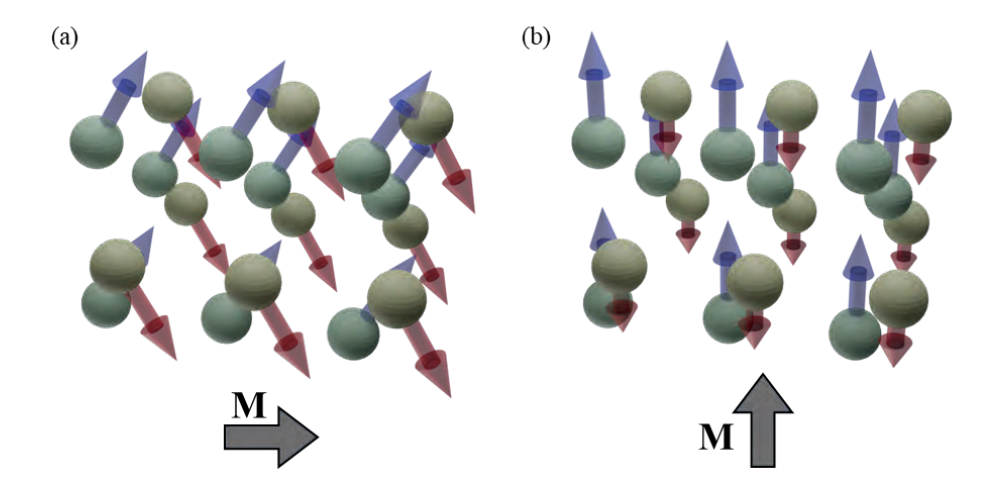


Fig. 1.4 . Schematic representation of spin alignment in (a) canted antiferromagnetic and (b) ferrimagnetic materials. Despite the antiferromagnetic coupling between the sublattices, the total magnetization is not zero.

# 1.3 Spin dynamics

#### 1.3.1 Ferromagnets

When one writes a magnetic bit, the magnetization orientation of a magnet is switched between two stable bit-states. Conventionally, the switching requires an external magnetic field. The field, in fact, produces a torque acting on the magnetization:

$$\mathbf{T} = \mathbf{M} \times \mathbf{H} \tag{1.19}$$

On the other hand, the torque can be expressed through the law of conservation of angular momentum **J**:

$$\frac{\partial \mathbf{J}}{\partial t} = \mathbf{T} \tag{1.20}$$

In turn, the angular momentum and the magnetization are related by the gyromagnetic ratio. In this case we have:

$$\frac{\partial \mathbf{M}}{\partial t} = -\gamma \mathbf{M} \times \mathbf{H} \tag{1.21}$$

This equation describes the motion of magnetization in an external magnetic field. If both sides of the equation are multiplied by  ${f M}$ , the following expression is obtained:

$$\frac{\partial \mathbf{M}^2}{\partial t} = 0 \tag{1.22}$$

From this, it follows that the magnitude of the magnetization vector remains constant. Equation (1.21) also implies that  $\partial \mathbf{M}$  is perpendicular to both  $\mathbf{M}$  and  $\mathbf{H}$ , which corresponds to the precession of the vector  $\mathbf{M}$  around the external magnetic field. To account for the damping of the precession, an additional term can be added to equation (1.21). Landau and Lifshitz proposed to account for damping by introducing a phenomenological term having the same symmetry as the other two:

$$\frac{\partial \mathbf{M}}{\partial t} = -\gamma \mathbf{M} \times \mathbf{H} - \frac{\gamma \lambda}{M^2} \mathbf{M} \times (\mathbf{M} \times \mathbf{H})$$
(1.23)

This equation is known as the Landau-Lifshitz equation, where  $\gamma$  is the gyromagnetic ratio and  $\lambda$  is a phenomenological damping parameter. The damping was further elaborated by Gilbert. The resulting equation is called the Landau-Lifshitz-Gilbert (LLG) equation and conventionally used in theoretical modeling of magnetic dynamics:

$$\frac{\partial \mathbf{M}}{\partial t} = -\gamma \mathbf{M} \times \mathbf{H} + \frac{\alpha}{M} \mathbf{M} \times \frac{\partial \mathbf{M}}{\partial t}$$
(1.24)

Here,  $\alpha$  is the damping parameter, which includes all possible energy dissipation processes and has dimensions inverse to velocity. This equation accurately describes the behaviour of magnets in the macrospin approximation but has its limits.

#### 1.3.2 Antiferromagnets

A simple antiferromagnet can be modelled as two antiferromagnetically coupled ferromagnets with magnetizations  $\mathbf{M}_1$  and  $\mathbf{M}_2$ , respectively. In the non-dissipative approximation, each sublattice obeys the Landau-Lifshitz equation. If one neglects the damping, the equations are [22]:

$$\begin{split} \frac{\partial \mathbf{M}_{1}}{\partial t} &= -\gamma \left[ \mathbf{M}_{1} \times \mathbf{H}_{1}^{\mathrm{eff}} \right] \\ \frac{\partial \mathbf{M}_{2}}{\partial t} &= -\gamma \left[ \mathbf{M}_{2} \times \mathbf{H}_{2}^{\mathrm{eff}} \right] \end{split} \tag{1.25}$$

where  $\gamma$  is the gyromagnetic ration that is assumed to be the same for two sublattices.  $\mathbf{H}_1^{\mathrm{eff}} = -\frac{1}{\mu_0} \frac{\partial \Phi}{\partial \mathbf{M}_1}$  and  $\mathbf{H}_2^{\mathrm{eff}} = -\frac{1}{\mu_0} \frac{\partial \Phi}{\partial \mathbf{M}_2}$  are effective magnetic fields experienced by the first and the second sublattice, respectively.  $\Phi$  is the thermodynamic potential of the antiferromagnet in terms of  $\mathbf{M}_1$  and  $\mathbf{M}_2$ . It can be shown that the main interactions contributing to  $\mathbf{H}_1^{\mathrm{eff}}$  are the effective field of the exchange interaction with the  $\mathbf{M}_2$  sublattice, the effective field of magnetic anisotropy  $\mathbf{H}^{\mathrm{ani}}$  and interaction with an external magnetic field  $\mathbf{H}^{\mathrm{ext}}$ .

Considering the case of a pure antiferromagnet with two sublattices of equal magnetizations  $|\mathbf{M}_1| = |\mathbf{M}_2| = M$ , and according to equations (1.13-1.14), one can rewrite the equations (1.25) in terms of  $\mathbf{L}$  and  $\mathbf{M}$ :

$$\begin{split} \frac{\partial \mathbf{M}}{\partial t} &= -\gamma \left[ \mathbf{M} \times \mathbf{H}_{\mathrm{M}}^{\mathrm{eff}} \right] - \gamma \left[ \mathbf{L} \times \mathbf{H}_{\mathrm{L}}^{\mathrm{eff}} \right] \\ \frac{\partial \mathbf{L}}{\partial t} &= -\gamma \left[ \mathbf{M} \times \mathbf{H}_{\mathrm{L}}^{\mathrm{eff}} \right] - \gamma \left[ \mathbf{L} \times \mathbf{H}_{\mathrm{M}}^{\mathrm{eff}} \right] \end{split} \tag{1.26}$$

where the effective fields are defined differently, i.e. in terms of the thermodynamic potential, which depends on  ${\bf L}$  and  ${\bf M}$ , respectively. In particular,  ${\bf H}_{\rm M}^{\rm eff}=-\frac{1}{\mu_0}\frac{\partial\Phi}{\partial{\bf M}}$  and  ${\bf H}_{\rm L}^{\rm eff}=-\frac{1}{\mu_0}\frac{\partial\Phi}{\partial{\bf L}}.$  The exchange interaction is known to be the strongest interaction in magnets responsible for the very existence of magnetic order. For materials that remain magnetic at room temperature, the effective fields of the exchange interaction are thus of the order of 100-1000 T. Taking the gyromagnetic ratio for a free electron, one finds that the period of the electron precession in such

a magnetic field is of the order of 30-300 fs. We can call this time an effective time of the exchange interaction. Naturally, aiming to reveal the fundamental and practical limits of the speed of magnetic writing, one has to push the spin dynamics to this time scale. Interestingly, if a magnet is excited by an external stimulus which is much shorter than the characteristic time required for a magnet to reach a thermodynamic equilibrium (~100 ps), such a stimulus brings the magnet into a strongly non-equilibrium state. Spin dynamics triggered by ultrafast stimuli is studied in the field of ultrafast magnetism.

## 1.4 Ultrafast magnetism

#### 1.4.1 Femtosecond laser pulse as an ultrafast heater

The development of laser technologies has made it possible to obtain pulses with durations of tens of femtoseconds. Already, the first experiments aiming to reveal spin dynamics triggered by such pulses led to unexpected results. It was found that following the optical excitation, the magnetization of a metallic film of ferromagnetic Ni was reduced by 40% on a time scale of a picosecond (Fig. 1.5(a)) [23]. This timescale appeared to be much shorter than any known interaction of the spins in Ni with the ultimate reservoir of angular momentum - lattice. It was suggested that the results can be explained by a phenomenological threetemperature model (Fig. 1.5(b)), where the femtosecond laser pulse mainly interacts with electrons, deposits heat into the reservoir associated with a free electron gas and subsequently launches heat transfer between the electrons, lattice and spins. The model suggested that ultrafast laser excitation opens up a new channel of ultrafast heat transfer between the spins and the electrons with a subsequent heat exchange between the electrons and the lattice. The origin of the channel has been heavily debated during the last 2 decades [24]. Interestingly, in magnetic dielectrics, this ultrafast channel must be absent as the materials have no free electrons.

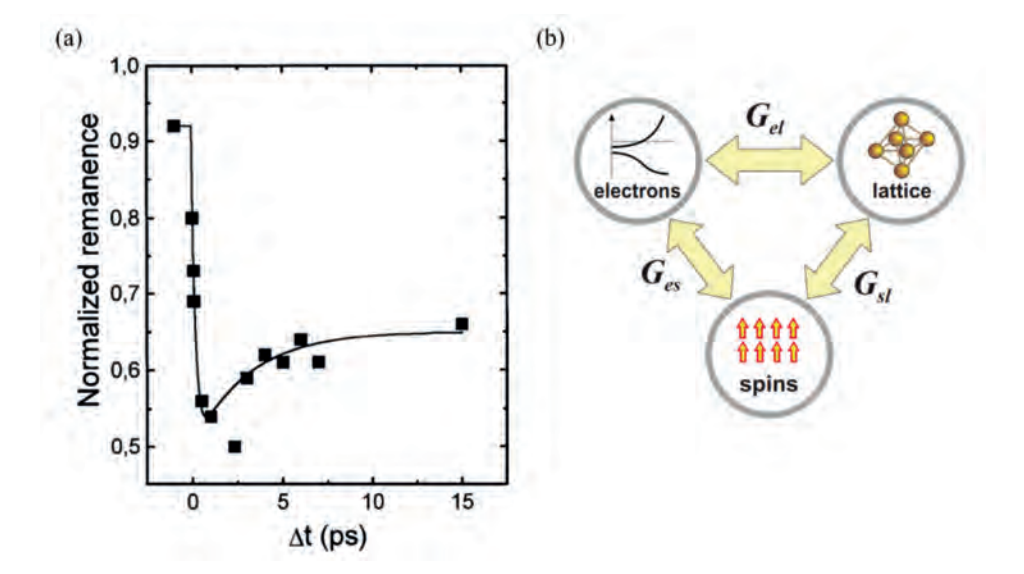


**Fig. 1.5.** (a) Transient remanent longitudinal MOKE signal of Ni/MgF<sub>2</sub> film under laser excitation. The Figure was taken from [23]. (b) Interacting reservoirs (carriers, spins, and lattice) in the three-temperature model. The figure is from [11].

#### 1.4.2 Femtosecond laser pulse as an effective magnetic field

How can light interact with spins without relying on heat? To describe these effects, we begin with the first law of thermodynamics and assume that all processes are reversible and thus, light-matter interaction is not associated with any entropy increase. Generally, in this case, a change of the internal energy during light-matter interaction is given by:

$$d\mathbf{U} = \mathbf{E}^{\omega} d\mathbf{P} + \mu_0 \mathbf{H}^{\omega} d\mathbf{M} \tag{1.27}$$

where  ${\bf E}$  and  ${\bf H}$  are the electric and magnetic fields of the electromagnetic wave with frequency  $\omega$ , and  ${\bf P}$  and  ${\bf M}$  are the electric polarization of the medium and its magnetization, respectively. We consider light-matter interaction under the electric dipole approximation and neglect the magnetic component of light:

$$d\mathbf{U} = \mathbf{E}^{\omega} d\mathbf{P}^{\omega} \tag{1.28}$$

where  $\mathbf{P}^{\omega}$  is the vector of electric polarization induced by the electric field of light. In the linear approximation, the electric polarization is a linear function of the electric field:

$$P_k^{\omega} = \epsilon_0 \widehat{\chi_{\rm kl}} E_l^{\omega} \tag{1.29}$$

Where  $\epsilon_0$  is the vacuum permittivity,  $\widehat{\chi_{kl}}$  is the tensor of optical susceptibility. The integral energy of the medium in this case is equal to:

$$U = \int d\mathbf{U} = U_0 + \frac{1}{2} \epsilon_0 \widehat{\chi_{\mathbf{k}l}} E_k^{\omega *} E_l^{\omega}$$
(1.30)

where  $U_0$  is the part of the internal energy of the medium that is independent of light. It can be shown that if the entropy of the system during light-matter interaction does not increase,  $\widehat{\chi_{kl}}$  is a Hermitian tensor [25]. Hence, the tensor of optical susceptibility can be represented as a sum of symmetric and antisymmetric parts:

$$\widehat{\chi_{\mathrm{kl}}} = \widehat{\chi_{\mathrm{kl}}^s} + \widehat{\chi_{\mathrm{kl}}^a}$$
 (1.31),

where  $\widehat{\chi_{kl}^s} = \widehat{\chi_{lk}^s}$  and  $\widehat{\chi_{kl}^a} = -\widehat{\chi_{lk}^a}$ . Consider the expansion of optical susceptibility dependent on M in a Taylor series. Using the Onsager principle, one can also show that in the series for the symmetric and antisymmetric parts certain terms are excluded by symmetry [25]:

$$\widehat{\chi_{\text{kl}}^{s}(M)} = \widehat{\chi_{\text{kl}}^{s}(0)} + \widehat{\beta_{\text{klmn}}^{'}} M_{m} M_{n} + \widehat{\gamma_{\text{klmn}}^{'}} L_{m} L_{n} + \dots$$

$$\widehat{\chi_{\text{kl}}^{a}(M)} = \widehat{i\alpha_{\text{klm}}^{'}} M_{m} + \widehat{i\alpha_{\text{klmnq}}^{'}} M_{m} M_{n} M_{q} + \dots$$
(1.32)

Where  $\widehat{eta_{klmn}'},\widehat{\gamma_{klmn}'},\widehat{lpha_{klm}'},\widehat{lpha_{klmnq}'}$  are phenomenological tensors. Then the internal energy is represented as:

$$U = U_0 + \frac{1}{2} \epsilon_0 \widehat{\epsilon_{kl}^s(0)} E_k^* E_l + i \frac{1}{2} \epsilon_0 \widehat{\alpha_{klm}^s} E_k^* E_l M_m + \frac{1}{2} \epsilon_0 \widehat{\beta_{klmn}^s} E_k^* E_l M_m M_n + \frac{1}{2} \epsilon_0 \widehat{\gamma_{klmn}^s} E_k^* E_l L_m L_n$$

$$(1.33)$$

Next, by employing equation (1.27), one can express the effective fields generated by light in the medium – fields that act either on the net magnetization  ${f M}$  or on the antiferromagnetic vector L:

$$\mathbf{H}_{\mathrm{M}}^{\mathrm{eff}} = -\frac{1}{\mu_{0}} \frac{\partial \Phi}{\partial \mathbf{M}} = -\frac{1}{\mu_{0}} \frac{\partial \epsilon_{\mathrm{kl}} (\mathbf{H}, \mathbf{M}, \mathbf{L})}{\partial \mathbf{M}} E_{k} (\omega) E_{l}^{*} (\omega)$$

$$\mathbf{H}_{\mathrm{L}}^{\mathrm{eff}} = -\frac{1}{\mu_{0}} \frac{\partial \Phi}{\partial \mathbf{L}} = -\frac{1}{\mu_{0}} \frac{\partial \epsilon_{\mathrm{kl}} (\mathbf{H}, \mathbf{M}, \mathbf{L})}{\partial \mathbf{L}} E_{k} (\omega) E_{l}^{*} (\omega)$$

$$(1.34)$$

Hence, both the total magnetization  $\mathbf{M}$  and the Néel vector  $\mathbf{L}$  can be affected by light and a laser pulse in particular. When the laser pulse is much shorter than the period of spin resonance, its action induces a small deviation of spins from their equilibrium orientation. The effective field  $\mathbf{H}_{\mathrm{M}}^{\mathrm{eff}}$ , generated by a femtosecond laser pulse, by circularly polarized light is called ultrafast inverse Faraday effect (IFE) [26]. Meanwhile, the effective magnetic field  $\mathbf{H}_{\mathrm{L}}^{\mathrm{eff}}$ , generated by linearly polarized femtosecond laser pulses is called inverse Cotton-Mouton effect (ICME) [27].

# 1.5 Magnetization switching in ferrimagnetic dielectrics

### 1.5.1 Heat-assisted magnetic recording in iron garnet

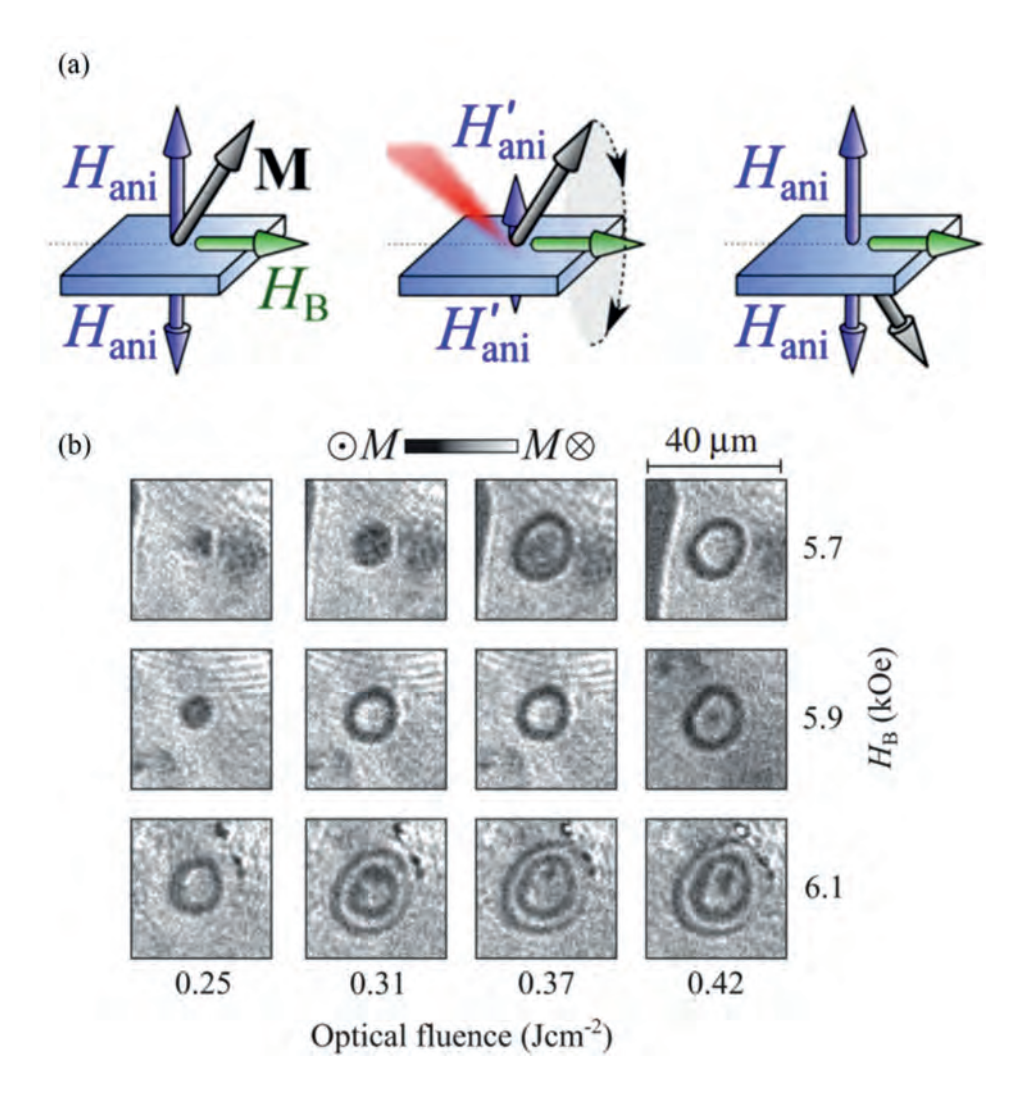
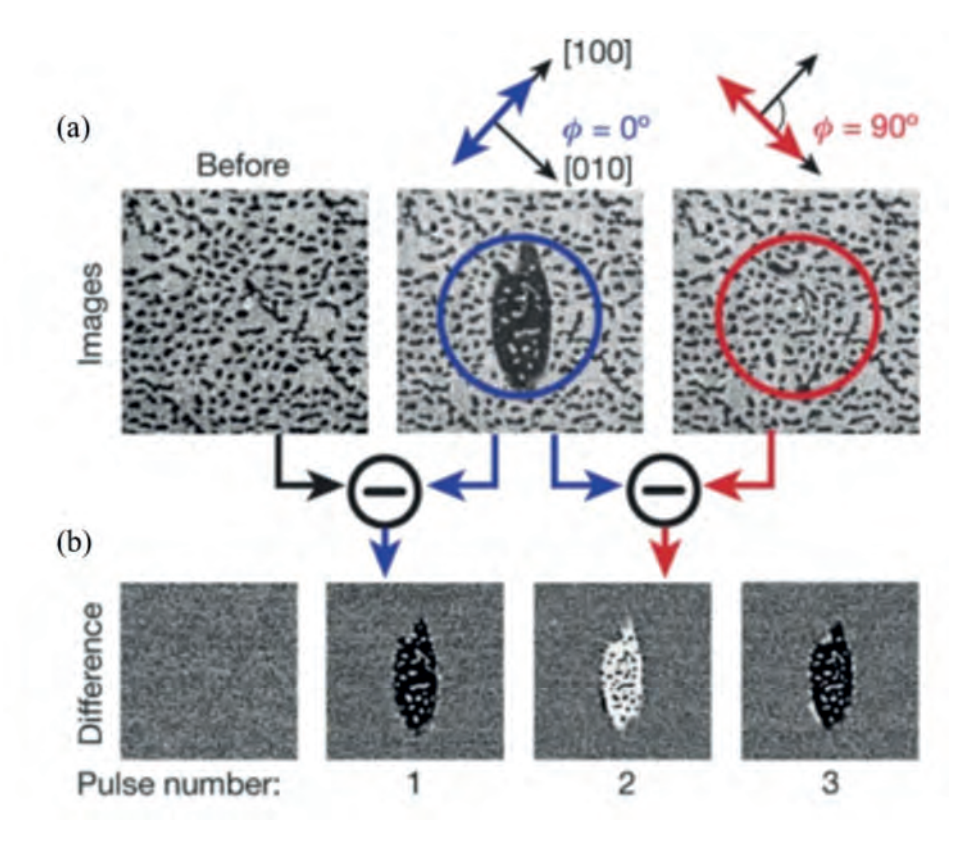


Fig. 1.6. (a) Mechanism of heat-assisted magnetization switching. (b) Snapshots of the out-of-plane component of magnetization, acquired 3.5 ns after exposure to the ultrashort optical pulse. The figure was adopted from [12].

Recently, C. Davies et al. demonstrated a new mechanism of HAMR in ferrimagnetic bismuth-substituted yttrium iron garnet. The mechanism is based on the temperature dependence of the magnitude of the magneto-crystalline anisotropy [12]. To achieve switching in this case, an external magnetic field  $\mathbf{H}_{\mathrm{ext}}$ 

was applied perpendicular to the easy axis of the magnetic crystal required (Fig. 1.6). If the magnitude of this field is comparable to the magnitude of the anisotropy field  $\mathbf{H}_{\rm ani}$ , the magnetization will not align along the easy axis but in the direction of the effective field  $\mathbf{H}_{\rm eff} = \mathbf{H}_{\rm ani} + \mathbf{H}_{\rm ext}$ . An ultrafast laser pulse heats the material, reducing the anisotropy field and thereby altering the orientation of the effective field. From the Landau-Lifshitz-Gilbert equation [28,29], it follows that the magnetization vector will precess around the new orientation



**Fig. 1.7.** Single-pulse non-thermal photo-magnetic recording. (a) From left to right, the domain pattern before the laser excitation, after excitation with a single laser pulse polarized along the [100] axis, and subsequent excitation with a similar laser pulse polarized along the [010] axis. (b) Differential changes after each of the pulse excitations. The Figure is from [30].

of the effective field. If the amplitude of this precession is significant enough, the magnetization overcome the potential barrier separating two stable states. Depending on the relaxation of the anisotropy field, the magnetization vector might either return to its original state or remain fixed in the switched state. The final state of magnetization does not depend on the polarization of optical radiation but

is entirely determined by the balance between magnetization dynamics and anisotropy field relaxation.

## 1.5.2 Non-thermal magnetic recording

Another mechanism of magnetic recording in ferrimagnetic dielectric without relying on heat was demonstrated in cobalt-substituted yttrium iron garnet [30]. Similar to the previous study, the magnetic switching was achieved through magnetization precession. However, this time, the onset of precession was due to photo-induced anisotropy resulting from the optical excitation of Co ions [31]. The efficiency of the excitation appeared to be strongly dependent on the orientation of the polarization of the linearly-polarized pump (Fig. 1.7). The achieved state was fixed due to the relaxation of the photo-excited electrons and recovery of the original magnetic anisotropy. The switching required about 60 ps. Consequently, unlike full optical magnetic switching in metals, switching in a transparent dielectric does not require any melting of magnetic order [32-34]. The authors found that the dissipated heat is much lower than during any known alternative mechanism. When scaled down to a bit size in the state-of-the-art magnetic devices (4000 nm<sup>3</sup>), the heat dissipated during non-thermal magnetic switching was estimated to be of the order of dissipating just 22 aJ, while all-optical switching in metals required 10 fJ [35], in the case of flash memory - 10 nJ [36], and hard drives - 10-100 nJ [37].

# 1.6 Open questions and the scope of the thesis

This thesis aims to further explore the mechanisms of HAMR in dielectrics with antiferromagnetically coupled spins.

The thesis is divided into six chapters. The first chapter is dedicated to the theory of magnetism and magnetic ordering in magnetic materials in general and in dielectrics in particular. This chapter also describes light-matter interaction and optomagnetic effects that enable optical control of magnetism.

The second chapter details the experimental methods used in the experimental work, the measurement of magnetization dynamics in thin films with spatial and temporal resolution. The operation of the camera and pump-probe technique are described. Schematic presentations of the setups for detecting diffraction on domain structures, single-shot imaging, and double pump experiments are provided.

The **third** chapter presents results on studying domain wall motion in lutetium iron-garnet under the influence of polarized femtosecond laser pulses. The use of magneto-optical diffraction as a method significantly improved the precision of measuring the relative size of domains with opposite magnetization directions. Furthermore, combining this method with the pump-probe detection scheme made it possible to conduct measurements with sub-picosecond temporal resolution. Analysis of the data obtained on lutetium iron-garnet showed temporal and spatial resolutions which were comparable with those obtained at the unique X-ray free electron lasers.

The **fourth** chapter focuses on the study of the dynamics of precessional heat-assisted switching of magnetization in lutetium iron-garnet. The influence of the initial temperature and magnitude of the external magnetic field on the outcome of optical switching of magnetization was explored. It was found that the switching occurs only within a narrow range of the explored parameters.

The **fifth** chapter describes the control of the spin-reorientation transition in  $(SmTb)FeO_3$  using two femtosecond pulses of opposite helicities ( $\sigma$ + and  $\sigma$ -). The idea is to use the first pulse to excite the precession of the magnetic moment and to heat the sample closer to the point of the spin-reorientation transition. The second pulse then determines the final state of the system. Depending on the delay time between the pulses, a periodic dependence of the magnetization direction of the final state was expected. However, temperature measurements combined with the time delay between the pulses gave a surprising result. In particular, we found a range of time-delays between the pulses, where the system remains insensitive to the polarization of the second pulse. This chapter also presents theoretical modeling based on the Lagrangian of two antiferromagnetic sublattices, which accounts for an increased magnetic damping near the spin-reorientation transition. It was shown that the latter explains the observed effect.

In the **sixth** chapter, more in-depth results concerning the control of the spin-reorientation transition in (SmTb)FeO<sub>3</sub> are presented. The polarization of the pulses was used to control the spin-reorientation transition. We attempted to separate thermal and polarization-dependent effects by using a linearly polarized pulse and controlling the orientation of its polarization plane. We found that regardless of the pump pulse polarization, the system remains insensitive to the second pulse for a certain period of time. Additionally, we experimentally studied the influence of different elliptical polarizations of the spin-reorientation transition. In particular, we identified the parameters under which a periodic dependence of

the magnetization direction in the final state was observed, as predicted theoretically.

The thesis concludes with a summary of all chapters and an outlook, discussing open opportunities for future experiments.

# Literature

- [1] T. M. Coughlin, Digital Storage for Professional Media and Entertainment, http://www.tomcoughlin.com (2009).
- [2] N. Youngblood, C. A. Ríos Ocampo, W. H. Pernice, and H. Bhaskaran, Integrated optical memristors, *Nature Photonics* 17 **(7)**, 561-572 (2023).
- [3] M. Mohammadi, M. Farahmand, S. Olyaee, and M. Seifouri, An overview of all-optical memories based on periodic structures used in integrated optical circuits, *Silicon* 14 (14), 8661-8680 (2022).
- [4] G. Vats, B. Hodges, A. J. Ferguson, L. M. Wheeler, and J. L. Blackburn, Optical memory, switching, and neuromorphic functionality in metal halide perovskite materials and devices, *Advanced Materials* 35 (37), 2205459 (2023).
- [5] C. Lian, C. Vagionas, T. Alexoudi, N. Pleros, N. Youngblood, and C. Ríos, Photonic (computational) memories: tunable nanophotonics for data storage and computing, Nanophotonics 11 (17), 3823-3854 (2022).
- [6] D. Weller, G. Parker, O. Mosendz, A. Lyberatos, D. Mitin, N. Y. Safonova, and M. Albrecht, FePt heat assisted magnetic recording media, *Journal of Vacuum Science & Technology B* 34 (6) (2016).
- [7] W.-H. Hsu and R. Victora, Heat-assisted magnetic recording—Micromagnetic modeling of recording media and areal density: A review, *Journal of Magnetism and Magnetic Materials* 563, 169973 (2022).
- [8] W. Challener *et al.*, Heat-assisted magnetic recording by a near-field transducer with efficient optical energy transfer, *Nature Photonics* 3 **(4)**, 220-224 (2009).
- [9] M. H. Kryder, E. C. Gage, T. W. McDaniel, W. A. Challener, R. E. Rottmayer, G. Ju, Y.-T. Hsia, and M. F. Erden, Heat assisted magnetic recording, *Proceedings of the IEEE* 96 (11), 1810-1835 (2008).
- [10] A. Kimel, A. Kirilyuk, P. Usachev, R. Pisarev, A. Balbashov, and T. Rasing, Ultrafast non-thermal control of magnetization by instantaneous photomagnetic pulses, *Nature* 435 (7042), 655-657 (2005).
- [11] A. Kirilyuk, A. V. Kimel, and T. Rasing, Ultrafast optical manipulation of magnetic order, *Reviews of Modern Physics* 82 (3), 2731-2784 (2010).
- [12] C. Davies *et al.*, Anomalously damped heat-assisted route for precessional magnetization reversal in an iron garnet, *Physical review letters* 122 **(2)**, 027202 (2019).
- [13] L. Hoddeson, G. Baym, and M. Eckert, The development of the quantum-mechanical electron theory of metals: 1928—1933, *Reviews of Modern Physics* 59 (1), 287 (1987).
- [14] L. Néel, Some new results on antiferromagnetism and ferromagnetism, *Reviews of Modern Physics* 25 **(1)**, 58 (1953).
- [15] C. Kittel, *Introduction to solid state physics Eighth edition*, (2021).
- [16] P. W. Anderson, Local moments and localized states, Science 201 (4353), 307-316 (1978).

- [17] R. Skomski, Simple models of magnetism, (2008).
- [18] H. Horner and C. Varma, Nature of spin-reorientation transitions, Physical review letters 20 (16), 845 (1968).
- [19] R. Szymczak and A. Balbashov, The temperature dependence of domain wall energy in TmFeO3, Physica B+ C 125 (1), 40-44 (1984).
- [20] A. Kimel, A. Kirilyuk, A. Tsvetkov, R. Pisarev, and T. Rasing, Laser-induced ultrafast spin reorientation in the antiferromagnet TmFeO3, Nature 429 (6994), 850-853 (2004).
- [21] S. K. Kim, G. S. Beach, K.-J. Lee, T. Ono, T. Rasing, and H. Yang, Ferrimagnetic spintronics, Nature materials 21 (1), 24-34 (2022).
- [22] A. Kimel, T. Rasing, and B. Ivanov, Optical read-out and control of antiferromagnetic Neel vector in altermagnets and beyond, Journal of Magnetism and Magnetic Materials, 172039 (2024).
- [23] E. Beaurepaire, J.-C. Merle, A. Daunois, and J.-Y. Bigot, Ultrafast spin dynamics in ferromagnetic nickel, Physical review letters 76 (22), 4250 (1996).
- [24] B. Koopmans, G. Malinowski, F. Dalla Longa, D. Steiauf, M. Fähnle, T. Roth, M. Cinchetti, and M. Aeschlimann, Explaining the paradoxical diversity of ultrafast laser-induced demagnetization, Nature materials 9 (3), 259-265 (2010).
- [25] L. D. Landau, J. S. Bell, M. Kearsley, L. Pitaevskii, E. Lifshitz, and J. Sykes, Electrodynamics of continuous media, Vol. 8, (2013).
- [26] T. Satoh et al., Spin oscillations in antiferromagnetic NiO triggered by circularly polarized light, Physical review letters 105 (7), 077402 (2010).
- [27] C. Tzschaschel, K. Otani, R. Iida, T. Shimura, H. Ueda, S. Günther, M. Fiebig, and T. Satoh, Ultrafast optical excitation of coherent magnons in antiferromagnetic NiO, Physical Review B 95 (17), 174407 (2017).
- [28] L. Landau and E. Lifshitz, in Perspectives in Theoretical Physics, pp. 51-65, (1992).
- [29] T. L. Gilbert, A Lagrangian formulation of the gyromagnetic equation of the magnetization field, Phys. Rev. 100, 1243 (1955).
- [30] A. Stupakiewicz, K. Szerenos, D. Afanasiev, A. Kirilyuk, and A. Kimel, Ultrafast nonthermal photo-magnetic recording in a transparent medium, Nature 542 (7639), 71-74 (2017).
- [31] F. Atoneche, A. Kalashnikova, A. Kimel, A. Stupakiewicz, A. Maziewski, A. Kirilyuk, and T. Rasing, Large ultrafast photoinduced magnetic anisotropy in a cobalt-substituted yttrium iron garnet, Physical Review B 81 (21), 214440 (2010).
- [32] C. D. Stanciu, F. Hansteen, A. V. Kimel, A. Kirilyuk, A. Tsukamoto, A. Itoh, and T. Rasing, Alloptical magnetic recording with circularly polarized light, Physical review letters 99 (4), 047601 (2007).
- [33] S. Mangin et al., Engineered materials for all-optical helicity-dependent magnetic switching, Nature materials 13 (3), 286-292 (2014).

- [34] C.-H. Lambert et al., All-optical control of ferromagnetic thin films and nanostructures, Science 345 (6202), 1337-1340 (2014).
- [35] M. Savoini et al., Highly efficient all-optical switching of magnetization in GdFeCo microstructures by interference-enhanced absorption of light, Physical Review B 86 (14), 140404 (2012).
- [36] J. P. Liu, E. Fullerton, O. Gutfleisch, and D. J. Sellmyer, Nanoscale magnetic materials and applications, (2009).
- [37] A. Hylick, R. Sohan, A. Rice, and B. Jones, An analysis of hard drive energy consumption, IEEE International Symposium on Modeling, Analysis and Simulation of Computers and Telecommunication Systems, pp. 1-10, (2008).

# CHAPTER 2

# **Experimental techniques**

This chapter describes the primary physical principles and the experimental techniques employed for research presented in this thesis. The magneto-optical Faraday effect is the central method utilized here for the detection of the magnetic state of the media. It explains how to investigate laser-induced spin dynamics in the time domain, achieved femtosecond temporal resolution, using the principles of the pump-and-probe technique. In this technique, an intense femtosecond laser pulse (pump) is employed to excite a magnet and thus launch spin dynamics. A time delayed and less intense laser pulse (probe) is used to measure the magneto-optical Faraday effect and thus reveal the state of the magnet at a given time delay after the pump. Finally, the chapter describes particular examples of the magneto-optical pump-and-probe techniques employed either for time-resolved magnetic imaging or integral measurements with high sensitivity.

# 2.1 Physical principles of optical probing of magnetism

## 2.1.1 Malus' law. Birefringence and dichroism

Light propagation in vacuum is an electromagnetic field for which the relationships between the electric field  $\mathbf{E}$ , the magnetic field  $\mathbf{H}$  (associated with the propagating light wave), and the wave vector  $\mathbf{k}$  are described by Maxwell's equations. A monochromatic plane wave is a particular solution of the equations, and due to the linearity of Maxwell's equations, a linear superposition of the solutions is also a solution of the equations. Using the Fourier transform, any propagating electromagnetic field can be expressed as a superposition of monochromatic plane waves. Hence, to understand the propagation of the field, it is sufficient to solve Maxwell's equations for a monochromatic plane wave. According to Maxwell's equations for a monochromatic plane wave, one finds:

$$\sqrt{\epsilon_0}\kappa \times \mathbf{E} = \sqrt{\mu_0}\mathbf{H};$$
 (2.1) 
$$\sqrt{\mu_0}\kappa \times \mathbf{H} = \sqrt{\epsilon_0}\mathbf{E};$$

where  $\kappa = \mathbf{k}/|\mathbf{k}|, \epsilon_0$  and  $\mu_0$  are the fundamental constants representing the electric permittivity and the magnetic permeability of vacuum, respectively. From these equations, it follows that all three vectors  $\mathbf{k}$ ,  $\mathbf{E}$ , and  $\mathbf{H}$  are mutually perpendicular. An important parameter of a plane wave is its polarization given by the wave; the fields  $\mathbf{E}$  (and therefore  $\mathbf{H}$ ) change in time. If  $\mathbf{E}$  (and therefore  $\mathbf{H}$ ) oscillates along a given direction and does not change direction, it is said that light is linearly polarized. If the vectors  ${f E}$  (and  ${f H}$ ) continuously rotate around  ${f k}$ , the light is called circularly polarized. An intermediate state is generally referred to as elliptically polarized.

Next, let us consider the interaction of linearly polarized light with an optically anisotropic medium whose dielectric permittivity is  $\epsilon_{kl}$ . Similar to Chapter 1, we treat the problem in the approximation of an electric dipole. Hence, light-matter interaction is fully described by  $\epsilon_{kl}$ . By a proper choice of the coordinate system, the matrix has only diagonal components. If a plane wave propagates in the direction of the z-axis, the electric field is non-zero only in the xy-plane, in that case, the electric displacement can be expressed as:

$$\begin{bmatrix} D_x \\ D_y \end{bmatrix} = \epsilon_0 \begin{bmatrix} \epsilon_{xx} & 0 \\ 0 & \epsilon_{yy} \end{bmatrix} \begin{bmatrix} E_x \\ E_y \end{bmatrix}$$
 (2.2)

In an optically anisotropic crystal,  $\epsilon_{\rm xx} \neq \epsilon_{\rm vv}$ , meaning that two orthogonally polarized components of light propagate differently. The refractive indices for these two waves with mutually orthogonal linear polarizations are  $n_x = \sqrt{\epsilon_{ ext{xx}}}$  and  $n_y = \sqrt{\epsilon_{
m vv}}$ . This difference in refractive indices for linear polarizations is called linear birefringence. According to the Kramers-Kronig relations, a difference in refractive indices implies a difference in the absorption coefficients. When discussing the difference in absorption of two waves with orthogonal linear polarizations, we speak of linear dichroism.

Both effects - linear birefringence and linear dichroism - are employed in building polarizers - optical components that transmit only a selected polarization of the incident wave. In polarizers based on linear dichroism, the orthogonal polarization component is absorbed. In contrast, polarizers employing linear birefringence can cause the orthogonally polarized components to propagate in different directions due to birefringent splitting. However, the spatial separation of polarization components occurs primarily under oblique incidence; at normal incidence, both components follow the same path, albeit with different phase velocities.

In 1810, E. L. Malus showed that when linearly polarized light passes through an ideal polarizer, the light intensity scales with the law known as Malus' law:

$$I = I_0 \cos^2 \theta \tag{2.3}$$

where  $I_0$  is the intensity of the incident light, I is the intensity of the transmitted light,  $\theta$  is the angle between the polarization planes of the incident light and the axis of the polarizer given by the polarization of the transmitted light.

If the dielectric permittivity of the medium acquires an antisymmetric part  $\epsilon^a_{
m kl}=\epsilon^a_{
m lk}$ , the latter should be purely imaginary, because matrix  $\epsilon_{kl}$  is Hermitian (see Chapter 1). We emphasize this fact by defining the antisymmetric components as  $\epsilon_{
m xy}=\epsilon_{
m yx}={
m ig}$ . Hence, the electric displacement is described by

$$\begin{bmatrix} D_x \\ D_y \end{bmatrix} = \epsilon_0 \begin{bmatrix} \epsilon_{\rm xx} & {\rm ig} \\ -{\rm ig} & \epsilon_{\rm yy} \end{bmatrix} \begin{bmatrix} E_x \\ E_y \end{bmatrix}$$
 (2.4)

Diagonalization of the matrix implies finding eigen vectors and eigen values of the matrix. The eigenvectors of the matrix  $\hat{\epsilon}$  correspond to right-handed and lefthanded circularly polarized waves:

$$\sigma^{+} = \begin{bmatrix} 1 \\ -i \end{bmatrix}; \sigma^{-} = \begin{bmatrix} 1 \\ i \end{bmatrix}$$
 (2.5)

Eigenvalues of the matrix are, in fact, the dielectric permittivities and, thus, the refraction coefficients experienced by the waves. If the refraction coefficients experienced by two circularly polarized waves are different, such a phenomenon is called circular birefringence. Consequently, due to the Kramers-Kronig relations, different refraction coefficients for two circularly polarized waves imply different absorption coefficients. The latter phenomenon is called circular dichroism.

It can be easily shown that if linearly polarized light propagates through a medium with a circular birefringence, the linear polarization continuously rotates i.e. linearly polarized light experiences polarization rotation.

## 2.1.2 Magneto-optical Faraday effect

Let us examine using thermodynamics how an external magnetic field influences optical properties of a medium. Using Eq. (1.30) one can define the dielectric permittivity as:

$$\epsilon_{\mathrm{kl}} = 1 + \chi_{\mathrm{kl}} = \frac{2}{\epsilon_0} \frac{\partial^2 U}{\partial E_k^* \partial E_l}$$
 (2.7)

where U is the total internal energy,  $\chi_{kl}$  is the optical susceptibility.

If during light-matter interaction the entropy of the system does not change, one can state that the system is time-invariant. Let us see how this condition affects Eq. (2.7) in the presence of a static external field, taking into account

that  $H^{\mathrm{ext}}(+t) = -H^{\mathrm{ext}}(-t)$  and  $U(+H^{\mathrm{ext}};+t) = U(-H^{\mathrm{ext}};-t)$ . We will consider harmonic changes of the electric field  $E_k\left(t\right)=E_{0,k}\mathrm{exp}\left(\mathrm{i}\omega t\right)$ . Hence,  $E_k(+t) = E_k^*(-t)$ , which brings about the following transformation in Eq. (2.7):

$$\epsilon_{kl} \left( + H^{\text{ext}}; +t \right) = \frac{2}{\epsilon_0} \frac{\partial^2 U \left( + H^{\text{ext}}; +t \right)}{\partial E_k^* \left( +t \right) \partial E_l \left( +t \right)} \\
= \frac{2}{\epsilon_0} \frac{\partial^2 U \left( - H^{\text{ext}}; -t \right)}{\partial E_k \left( -t \right) \partial E_l^* \left( -t \right)} \\
= \epsilon_{lk} \left( - H^{\text{ext}}; -t \right) \tag{2.8}$$

Since the system is time-invariant, we conclude that  $\epsilon_{\rm kl}\,(+H^{\rm ext})=\epsilon_{\rm lk}(-H^{\rm ext})$ . This result, in turn, leads to an important finding about symmetric and antisymmetric parts of the dielectric permittivity, which must be even and odd with respect to an external magnetic field, respectively.

$$\epsilon_{kl}^{s} \left( + H^{\text{ext}} \right) = \epsilon_{lk}^{s} \left( - H^{\text{ext}} \right) = \epsilon_{kl}^{s} \left( - H^{\text{ext}} \right) 
\epsilon_{kl}^{a} \left( + H^{\text{ext}} \right) = \epsilon_{lk}^{a} \left( - H^{\text{ext}} \right) = -\epsilon_{kl}^{a} \left( - H^{\text{ext}} \right)$$
(2.9)

Assuming that the external magnetic field produces only a small perturbation to the dielectric permittivity, the symmetric and antisymmetric components of the dielectric-permittivity tensor can be expanded in a Taylor series:

$$\epsilon_{kl}^{s}(H) = \epsilon_{kl}^{s}(0) + a\ddot{H}^{2} + b\ddot{H}^{4} + c\ddot{H}^{6} + \dots$$

$$\epsilon_{kl}^{a}(H) = a\dot{H} + b\dot{H}^{3} + c\dot{H}^{5} + \dots$$
(2.10)

Hence, the external magnetic field affects the symmetric and antisymmetric parts of the tensor differently. From Equations (2.2) and (2.4), it follows that the linear birefringence and circular birefringence, which are defined by the symmetric and the antisymmetric parts of the dielectric permittivity, must scale quadratically and linearly with the applied magnetic field, respectively.

In 1845, M. Faraday demonstrated for the first time that a magnetic field can induce optical anisotropy in an initially isotropic medium. In his experiment, linearly polarized light passed through a transparent sample (a piece of lead-borosilicate glass), and a magnetic field was applied either along the beam path or opposite to it (Fig. 2.1). With the polarizer and analyzer suitably oriented, in the absence of a magnetic field, the transmitted light intensity fell to zero. When the field was applied, light again began to pass through the polarizer-sample-analyzer setup, proving that the external magnetic field alters the polarization state of the light. Empirically, Faraday found a linear relationship between the angle of polarization rotation  $\theta$  and the external field [1]:

$$\theta = \nu H^{\text{ext}} d \tag{2.11}$$

where d is the sample thickness, and  $\nu$  is the Verdet constant, a material-specific parameter. In general, the Verdet constant  $\nu$  not only depends on the sample material but also on the light wavelength,  $\nu=\nu\left(\lambda\right)$ . Diagonalizing the dielectric permittivity matrix  $\epsilon_{\rm kl}$  from Eq. 2.4 under assumption that  $\epsilon_{xx}=\epsilon_{yy}$  and assuming that  $\epsilon_{\rm kl}^a\left(H^{\rm ext}\right)=a^{'}H^{\rm ext}$ , it can be shown that  $\nu=\frac{2\pi a^{'}}{\sqrt{\epsilon_{xx}\lambda}}$ 

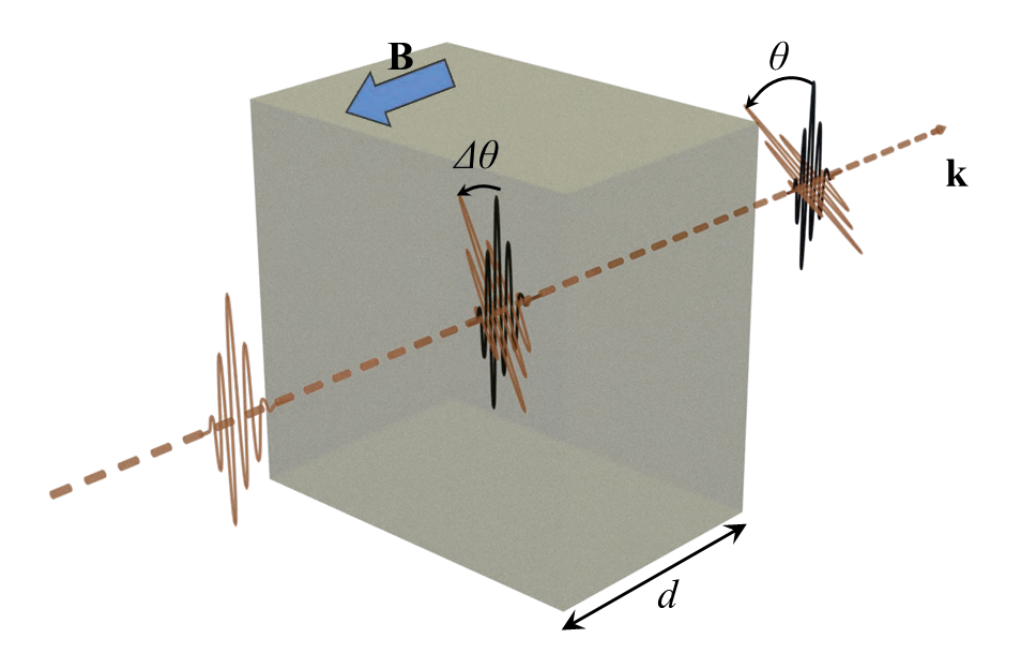


**Fig. 2.1**. Magneto-optical Faraday effect. Linearly polarized light changes its polarization orientation upon propagation **k** through the magnetic medium.

As the magnetic field  $H^{\rm ext}$ , the magnetic induction  ${\bf B}$  and the magnetization  ${\bf M}$  are all axial vectors, they share the same transformation properties under spatial

symmetry operations such as inversion and rotation [2]. As a result, the symmetry consideration outlined in Eqs.2.8-2.10 apply equally to each of these quantities. Hence, one can also write:

$$\theta = \nu \mu_0 (M + H^{\text{ext}}) d \tag{2.13}$$

which makes the Faraday effect a powerful tool for studying the spin structures in magnetic materials, as it reveals how the magnetization  $\mathbf{M}$  depends on the applied magnetic field  $H^{\mathrm{ext}}$ .

## 2.2 Detection methods

### 2.2.1 Magneto-optical imaging

Let us now consider a practical application of the Faraday effect using a simple detection setup. It is important to note that a conventional light detector, such as a photodiode, detects the intensity of the incident light. Although some detectors can do this with a remarkable sensitivity - down to a single photon - information about the polarization state of the light cannot be obtained without additional installations. In accordance with Malus's law (Eq. (2.3)), the polarization rotation angle  $\theta$  can be measured using a source of unpolarized light and two polarizers. The first polarizer, placed before the sample, produces a linearly polarized light, while the second polariser, placed after the sample and often called an analyzer, transforms information about polarization rotation in the sample into an intensity change.

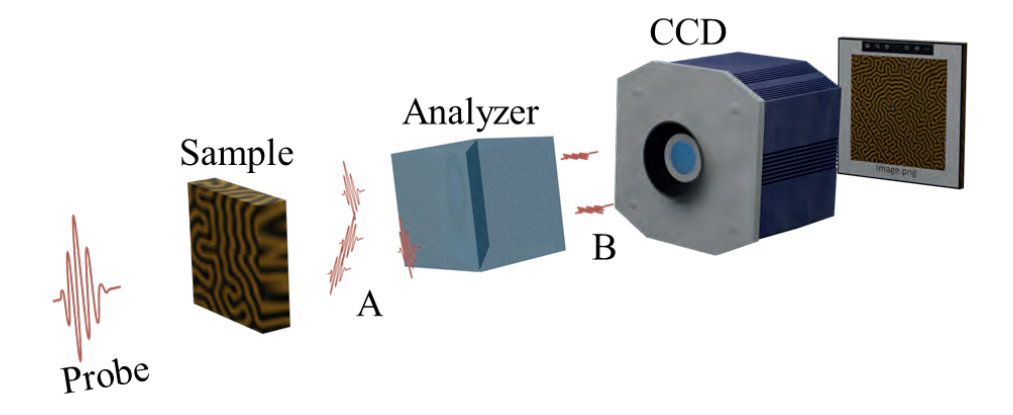


Fig. 2.2 . Spatially-resolved resolved Faraday rotation. A - different polarization rotation for the domains with opposite magnetization (+M and -M). B - CCD camera detects only the light which has a polarization component along the easy axis of the analyzer.

Let us analyze how the detected signal intensity depends on the angle  $\theta$ . Assume that the polarizer is oriented at zero degrees. The analyzer orientation is then set to  $\frac{\pi}{3}$ . When the polarization plane is rotated due to the magneto-optical Faraday effect  $\theta$ , according to Malus's law, the intensity is given by

$$I = lpha I_0 \mathrm{cos}^2 \left(rac{\pi}{2} + heta
ight) = lpha I_0 \mathrm{sin}^2 \left( heta
ight)$$
 (2.14)

where  $\alpha$  accounts for absorption within the medium. For small  $\theta$ , the  $\sin(\theta)$  will be proportional to  $\theta$  itself. In such a case, the relationship between the detected signal and the angle of polarization rotation will be quadratic.

This setup measures the magnetic properties of the sample over the entire illuminated area, without spatial resolution. The measurement accuracy strongly depends on both the beam focusing and its alignment relative to surface defects.

A similar scheme can be employed for the visualization of magnetic domains or spatial distribution of magnetization of another origin [3]. In this case, a CCD camera is employed instead of a photodiode. In particular, each camera pixel acts as an independent photodetector. Consider a multidomain sample (Fig. 2.2). For simplicity, suppose there are only two domain types: one with magnetization  $+\mathbf{M}$ and one with magnetization  $-\mathbf{M}$ , both along or against the light-propagation direction. Unfocused, linearly polarized light passes through several oppositely magnetized domains. Depending on the domain's magnetization, the linear polarization is rotated by  $+\theta$  for  $+\mathbf{M}$  and by  $-\theta$  for  $-\mathbf{M}$ . Setting the polarizer such that light passing through one of the magnetic domain types, say  $+\mathbf{M}$ , is completely blocked, one can get a magneto-optical image of the sample. The light reaching the camera will pass exclusively through  $-\mathbf{M}$  domains. The obtained image will reveal dark and bright areas corresponding to  $+\mathbf{M}$  and  $-\mathbf{M}$ domains, respectively.

Notably, the setup can be easily upgraded and obtain a capability of magnetooptical measurements with a temporal resolution. Using a pulsed light source and delaying the light flash, one can obtain magneto-optical snap shots of the sample at a given time with a time resolution limited by the duration of the light pulse.

## 2.2.2 Balanced photodetector

Improving detector sensitivity remains a continuous challenge in experimental research. The balanced photodetector is considered the most advanced method for sensitive polarization rotation measurements, allowing compensation of lightsource intensity noise [4].

The idea behind balanced detection is to use two photodiodes. In this scheme, an explicit analyzer is not used; instead, a Wollaston prism is pre-installed in the balanced detector. This prism splits the incoming light between two photodiodes, which are rigidly fixed on a rotating platform. The platform can rotate about an axis passing through the center of the Wollaston prism and the geometric midpoint between the two photodetectors. Aligning the balanced detector involves carefully matching its rotational axis to the incoming beam path. Under correct alignment, the total (summed) signal from the two photodiodes corresponds to the intensity of the light entering the Wollaston prism and does not depend on the platform orientation.

Let us consider the intensities measured by the two photodiodes:

$$I_1 = I_0 \left( t \right) \cos^2 (lpha + heta)$$
 
$$I_2 = I_0 \left( t \right) \cos^2 \left( \frac{\pi}{2} + lpha + heta 
ight)$$
 (2.15)

where  $I_0\left(t\right) = I_{\mathrm{DC}} + \Delta I\left(t\right)$  is the intensity of the light source with a noise contribution  $\Delta I(t)$ ,  $\alpha$  is the orientation angle of the Wollaston prism. The sum and the difference signals are then:

$$I_{+}=I_{0}\left( t
ight)$$
 
$$I_{-}=I_{0}\left( t
ight) \cos 2(lpha + heta ) \tag{2.15}$$

It is evident that the sum signal  $I_+$  loses all information about the light's polarization and the Wollaston prism's orientation, retaining only the source intensity. By dividing the difference signal by the sum signal, one can completely intensity fluctuation remove the light-source and retain only the polarization information.

If the probe pulse is linearly polarized, it is possible to reach a position where the two photodetector signals are identical. In this balanced state,  $\alpha=\pi/4$ , the differential signal  $I_{-}$  becomes zero, and the entire dynamic range of the photodetectors can be fully utilized. To maximize the signal-to-noise ratio, it is critical that the two photodetectors (and their optical paths) be perfectly matched. Notably, each detector's shot noise is statistically independent, meaning that there is no noise correlation. Therefore, the shot noise remains the same in the differential current, even when  $I_{-}=0$ . Any perturbation—such as magnetization precession—that rotates the probe polarization plane makes the signals from the two photodiodes deviate from their balanced condition. Consequently, the resulting difference signal is amplified, allowing the detection of very small polarization changes relative to the balanced position. For more details on the balanced photodetector scheme, see [5,6].

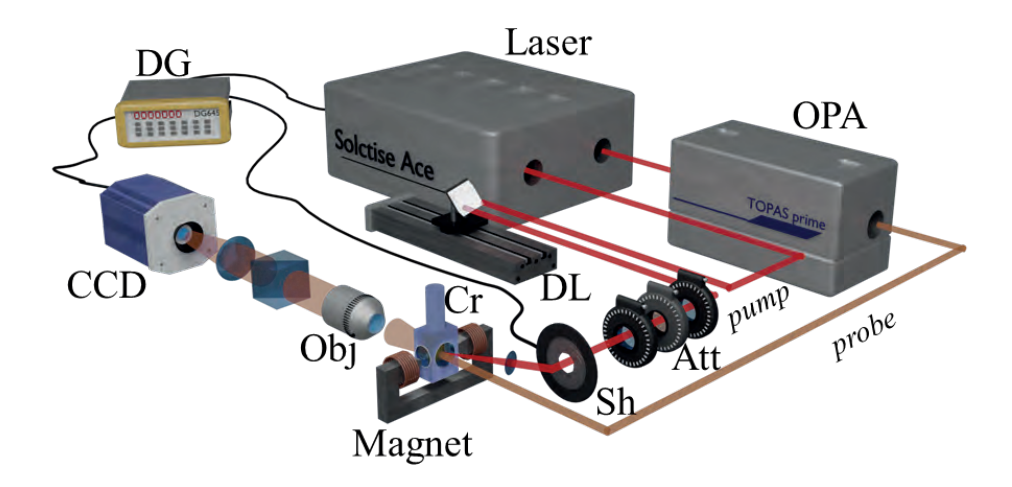


Fig. 2.3 . Schematics of single-shot pump-probe experiment. The pump and probe pulses have different wavelengths. The time delay between the pump and probe pulses is adjusted using a delay line (DL). The power and polarization of the laser pulse are controlled by an attenuator (Att). A shutter (Sh) blocks every second pump pulse to obtain a reference image. The sample is placed in a cryostat (Cr), and a magnet provides a constant magnetic field. The pump pulse is focused onto the sample, while the probe pulse remains unfocused but collimated. Using an objective lens (Obj) and an analyzer, we obtain magneto-optical images on a CCD camera. A delay generator (DG) synchronizes the operation of the laser, shutter, and CCD camera.

# 2.3 Principles of time-resolved measurements

The simplest approach to reveal magnetization dynamics in a sample is to measure the signal's time dependence directly from the detector, for instance, using an oscilloscope. In that case, the sample is continuously illuminated by the light source. After an external stimulus initiates magnetization dynamics, the detector output is displayed on the oscilloscope as a time sweep. This method is intuitive, as it directly reveals how the detector signal changes over time. However, both the photodetector and the oscilloscope must have a sufficiently fast response. Currently, the fastest commercial oscilloscopes operate up to about 2 GHz, corresponding to a time resolution of 0.5 ns. This resolution is inadequate for investigating electronic precession on the order of 30-300 fs (see Chapter 1).

To attain better temporal resolution, pulsed light sources are used. Modern laser systems can reach pulse durations on the order of a few femtoseconds. By controlling the delay between the pump and probe pulses, which triggers magnetization dynamics, and the probe pulse, which monitors it, one achieves a time resolution on the order of the probe-pulse duration. This single probe pulse acts like a flash for the photodetector. In this scenario, neither the detector's response speed nor its readout scheme imposes any fundamental limitation on the temporal resolution of the experimental setup [7,8].

## 2.3.1 Single-shot imaging

If one uses a sufficiently intense pulse, the pump-probe scheme can work in a single-shot mode. For instance, one uses a single pump pulse to launch magnetization dynamics and a single probe pulse to capture the spatial distribution of magnetization with the help of a CCD [9,10]. In our experiments, the pump pulse also came from the same laser system as the probe (Fig. 2.3). This arrangement simplifies synchronizing the time delay between the pump and the probe pulses, naturally avoiding a jitter.

To delay the probe pulses relative to the pump, a delay line is employed. It consists of three orthogonal mirrors (a retroreflector) mounted on a precise micrometer translation stage. By moving the retroreflector with a servo motor, one extends the optical path of one pulse. Knowing the speed of light, one can predict that introducing a spatial delay between the pulses of 1 micrometer yields a temporal delay of about 3 fs. In principle, one can place the delay line in either the probe or the pump beam path. However, in practice, putting the delay line into the pump path offers some advantages. First, the detection scheme becomes less vulnerable to alignment errors in the delay line. Because the delay stage can extend the optical path by 1.2 m or even 2.4 m, the beam spot may shift on the sample. A shift in the probe spot adversely affects how it hits the detector, but a shift in the pump spot is relatively harmless, provided the pump spot is larger than the probe. Another point is defocusing: over a long optical path, any nonzero beam divergence increases spot size and changes the intensity distribution at different delays. If that happens to the probe pulse, the noise at large delays can dominate the useful signal.

The fundamental single-shot-imaging procedure consists of two measurements: one with the pump blocked and one with the pump unblocked. The first measurement provides a reference signal for the sample's initial state; the second measures the pump-induced change. Another key question is how to separate the probe and pump after they pass through the sample. Because we record an image over a large area, simple geometric separation, where the pump beam enters the sample at an angle and refracts away from the probe path, may not suffice. For that reason, we used an OPA (Optical Parametric Amplifier), which generates pulses at different wavelengths via parametric amplification. Hence, using the same laser

system in combination with a Topas Prime OPA, we could shift the probe's wavelength and then filter out the pump with the help of optical filters.

To obtain a spatially resolved image of the sample, we use a 10× macro lens, a polarizer, and a camera. A tabletop cryostat controls the sample's initial temperature. An electromagnet capable of producing fields up to 0.5 T in the cryostat region applies the external magnetic field (not shown in the schematic). Because the cryostat makes it impossible to place a standard macro lens at the focal distance, a long-focus lens with a focal length of 1 cm is used instead.

To extract the pump-induced signal, one subtracts the reference image from the pump image in post-processing. Such recordings enable not only mapping the sample's spatial magnetization distribution but, with additional processing, also evaluating the average intensity (i.e., polarization-plane rotation). The noise levels in these camera-based images depend on the sensor and its cooling but generally exceed those of a balanced photodetector. Therefore, for such measurements, a sample with a strong Faraday magneto-optical effect is preferred.

## 2.3.2 Pump-probe technique

Another way to detect magnetic dynamics with a boosted sensitivity is to employ a stroboscopic pump-probe technique [8]. Here, one uses a sequence of identical pulses spaced at a given repetition rate. If the interval between two pulses is sufficiently long that the system returns to its initial state, each pump pulse in the sequence drives the very same dynamics. The repetition rates of the pump and probe pulses should be in a 1:2 ratio. Because a CCD camera has a long readout time and thus cannot be ready when the next probe pulse arrives, photodetectors and a balanced photodetector, in particular, are employed in our setup (Fig. 2.4).

The logic behind analyzing the balanced-photodetector signals involves separating the probe pulses into two channels, one with the pump blocked and one with the pump unblocked, and then subtracting one from the other. A boxcar integrator, whose operating principle is illustrated in Fig. 2.4(d), is used for this purpose. Synchronized to the laser repetition rate, the boxcar integrator splits even and odd signals into  $I_1$  and  $I_2$ , respectively. Note that the femtosecond pulse duration is many orders of magnitude shorter than the pulse-to-pulse period (tens of microseconds). Hence, the balanced photodetector detects zero signal for most of each cycle, accumulating noise in the process. To reduce the noise, the entire signal from the photodetector is multiplied by a square wave of width  $\omega$  and integrated afterwards. As a result, most of the noise is cancelled out, leaving only the useful part. By digitally subtracting the two channels  $I_1 - I_2$ , one obtains the pump-induced component of the signal. Thanks to multiple repetitions and averaging, the resulting pump-induced signal has much lower random noise without reducing the level of the useful signal.

Because of limited electronics speed, a boxcar integrator does not work well at repetition rates higher than a few kilohertz. In such high-frequency cases, a lock-in amplifier is used, which typically offers greater noise suppression.

A lock-in amplifier multiplies the incoming signal (in our case, from the balanced photodetector) by a reference signal and then applies a low-pass filter. This demodulation isolates the useful component at the desired frequency from all others. The reference signal can come from the lock-in itself or from the laser. Because the laser's repetition rate may not precisely match its nominal value, it is preferable to use a reference derived directly from the laser. Originally, the lock-in amplifier design assumed that both the signal and the reference would be sinusoidal. Internally, the amplifier splits the incoming signal and multiplies it separately by the reference and a 90°-phase-shifted copy of the reference. Each product then passes through a low-pass filter, yielding two outputs, X and Y, known as the in-phase and quadrature components. The amplitude R and phase  $\varphi$ are obtained by converting (X, Y) from Cartesian to polar coordinates:

$$R=\sqrt{X^2+Y^2}$$
 (2.16)  $arphi= an\left( \measuredangle\left( Y,X
ight) 
ight)$ 

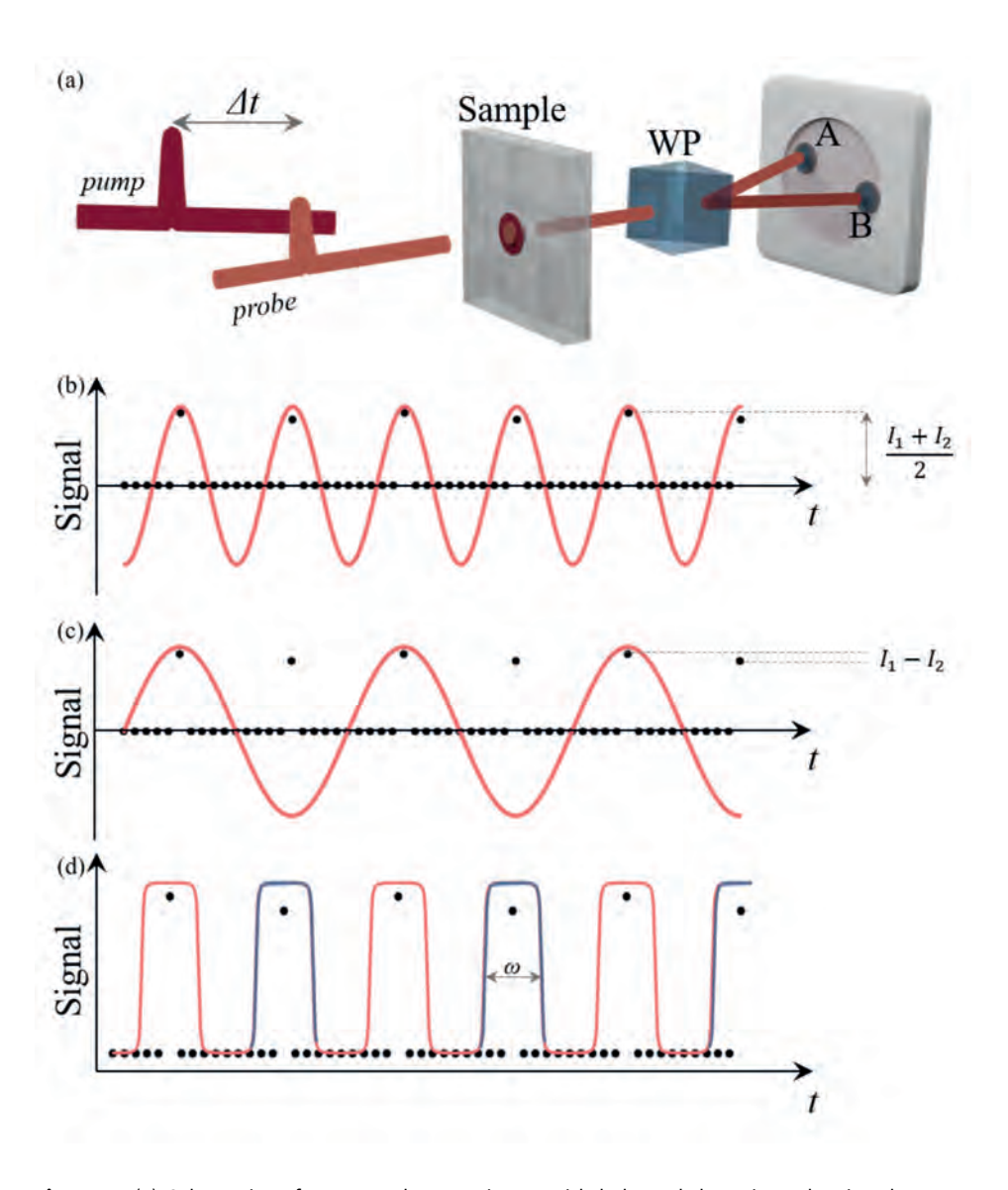


**Fig. 2.4.** (a) Schematics of pump-probe experiment with balanced detection. The time between pump and probe pulses  $\Delta t$  is controlled by the delay line (not shown on the scheme). Wollaston prism separates light into two beams with orthogonal polarizations, which are detected with photodiodes A and B. b-d) dots – A – B pump-probe signal. The pump repetition rate is twice as low as the probe one. Thus, the signal from half of the probe pulses is not affected by the pump ( $I_1$ ), and the other half is pump-affected ( $I_2$ ). Lines are lock-in reference at (b) probe frequency, (c) pump frequency, (d) Boxcar integrator gates.

In practice, however, while the reference signal is sinusoidal, the detected signal from the balanced photodetector often resembles a delta function (owing to a 1 kHz repetition rate and a 40 fs pulse duration; see Fig. 2.4(b)). Let us say  $I_1$  is the

balanced-detector signal when the pump is blocked, and  $I_2$  is the pump-induced signal. By choosing the proper phase between the detector signal and reference, both  $I_1$  and  $I_2$  can be aligned with the positive maxima of the reference sine wave. After low-pass filtering, the resulting DC output is  $(I_1+I_2)/2$ . However, if we set the reference at half the laser's repetition rate (Fig. 2.4(c)), each even-numbered probe pulse  $(I_1)$  lines up with the positive maximum, whereas each odd-numbered probe pulse  $(I_2)$  hits the negative maximum. Thus, the net signal corresponds to  $(I_1-I_2)$ , directly measuring the pump-induced change in the system.

When interpreting results, calibration is needed. For small Faraday rotations  $\theta$ , the relationship between signal intensity and  $\theta$  is linear. In that regime, collecting a few calibration points is sufficient. This is done by rotating the balanced detector base by a few degrees around the beam path and normalizing the observed differential signal using a linear approximation.

To see why the differential signal depends linearly on  $\theta$ , consider linearly polarized light oriented at 45° to the Wollaston prism's optical axis. The intensities at detectors A and B are then

$$E_A^2=E^2\mathrm{sin}^2\left(rac{\pi}{4}
ight)$$
 
$$E_B^2=E^2\mathrm{cos}^2\left(rac{\pi}{4}
ight)$$
 (2.17)

The differential signal, in this case, would be zero. Now, let's introduce a slight deviation in the polarization plane by an angle  $\theta$ :

$$E_A^2=E^2 \sin^2\left(rac{\pi}{4}+ heta
ight)$$
 (2.18) 
$$E_B^2=E^2 \cos^2\left(rac{\pi}{4}+ heta
ight)$$

The measured intensity will then be proportional to their difference:

$$I \propto E_A^2 - E_B^2 = E^2 \left( \sin^2 \left( rac{\pi}{4} + heta 
ight) - \cos^2 \left( rac{\pi}{4} + heta 
ight) 
ight) = E^2 \sin(2 heta)$$
 (2.19)

For small angles,  $\sin 2\theta \approx 2\theta$ , so the signal is proportional to  $\theta$ .

Because a standard lock-in amplifier presupposes harmonic signals, and our pulse train resembles delta functions, the repetition rate of the experiment strongly affects the instrument's sensitivity. To maximize the signal-to-noise ratio, operating at higher repetition rates is generally advantageous.

# 2.4 Double-pump excitation

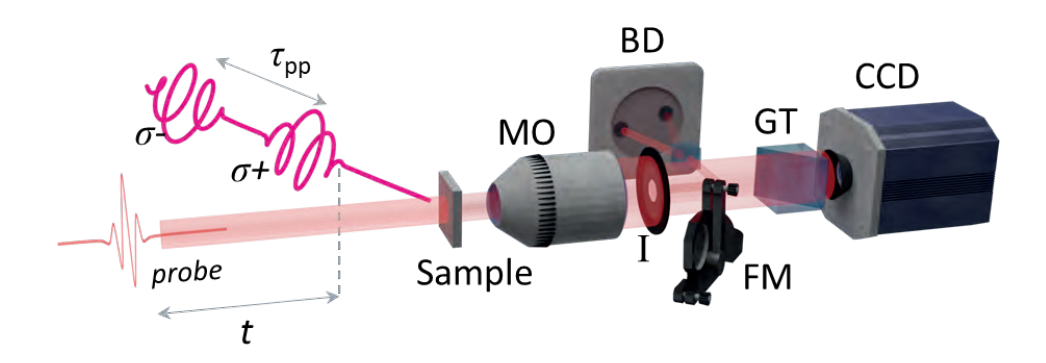


Fig. 2.5 . Schematics of double pump experiment. Probe and the second pump pulse are delayed with two delay lines (t and  $\tau_{pp}$ , respectively). Two pump pulses have circular polarizations with opposite helicities. The polarizations can also be set at an arbitrary, elliptical state. Passing through the micro-objective (MO) probe pulse can be focused onto the balance photodetector (BD) or CCD-camera using a flip-mirror. Iris (I) used to separate the pump-affected area of the sample for the balance detection. GT - Glan-Taylor polarizer.

In Chapters 5 and 6, we present an upgraded experimental setup that uses two pump pulses with independently controlled powers and polarizations (Fig. 2.5). Both pump pulses are derived from a single output of the laser system, with a central wavelength of 800 nm and a pulse duration of 40 fs. The beam is split into two parts using a beam splitter. Each pump arm contains an attenuator for power control and either a half-wave or quarter-wave plate to set the polarization. One of the pump paths includes a mechanical delay line, allowing control of the temporal delay between the pump pulses in the range of -120 to +120 ps. After passing through the respective optical elements, the two pump beams are recombined using a non-polarizing beam splitter. Both pump pulses are incident on the sample at the same angle of 15° relative to the surface normal. A single focusing lens is used to focus both pump beams onto the sample.

The probe pulse is generated from an OPA (Optical Parametric Amplifier) and has a tunable wavelength ranging from 500 to 1300 nm, with a pulse duration of ~50 fs. A delay line is installed in the probe path to control the temporal delay between the (fixed-time) pump and probe pulses, with a maximum delay up to 3 ns. The probe path also includes an attenuator and a replaceable waveplate. For large changes in the probe wavelength, the waveplate must be replaced with one matched to the probe wavelength. The probe beam is collimated (not focused) and incident normally on the sample. The thin-film sample is transparent at the probe wavelength, allowing for magneto-optical imaging of the spatial distribution of magnetization induced by the pump pulses.

The use of different wavelengths for pump and probe enables spectral separation of the probe signal using a narrow-band optical filter. The sample is placed in a cryostat (not shown in the figure) with continuous liquid nitrogen flow. By controlling the built-in heating element, the sample temperature can be set in the range of 77 K to 300 K. In the experiments described in Chapters 5 and 6, no external magnetic field was applied, since at low temperatures the magnetization returned to its initial state between probe pulses.

The setup supports dual detection modes: CCD camera imaging and balanced photodetector-based measurement. An iris (I) and flip mirror (FM) are used to switch between the detection paths. For spatially resolved magneto-optical singleshot imaging, the iris is fully open and the flip mirror is retracted. A Glan-Taylor polarizer and focusing lens are placed in the probe path to project the Faradayrotated probe beam onto the CCD camera sensor. The laser is operated in singleshot mode to capture snapshots of the sample under the influence of both pump pulses and in the unperturbed state (with both pumps blocked).

To measure the integrated magnetization in the pumped region with higher precision, the balanced detection scheme is used. The iris is partially closed to isolate the area of pump excitation (guided by the CCD image), and the flip mirror redirects the probe beam to the balanced photodetector, connected to a lock-in amplifier. The laser operates at a repetition rate of 1 kHz. The pump pulse train is modulated using a mechanical chopper placed in the shared pump path, so that the pump repetition frequency is half that of the probe.

# 2.5 Experiment Automation

All experiments presented in this thesis were automated, eliminating human error inherent to manual experiments. Another major advantage of automation is the

repeatability of measurements. The external conditions of the experiment were maintained and monitored throughout the entire data collection process. The independence of such measurements from human presence allowed continuous acquisition not only during the day but also overnight and across multiple days.

Automation was implemented through two subsystems - hardware and software. The hardware setup included the following devices:

#### 1. **Laser System**

A Ti:Sapphire amplified laser system (Spectra-Physics, Spitfire) was used to produce pulses at a central wavelength of 800 nm (1.55 eV), with a variable repetition rate ranging from 20 Hz to 1 kHz, as well as in singleshot mode. To control the single-shot mode, external square pulses with a voltage of 5 V were applied. The laser system was triggered by a coaxial signal from the DG645 delay generator.

#### 2. **DG645 Digital Delay Generator**

The DG645 (Stanford Research Systems) served as the central timing unit, generating square control pulses for other hardware elements. It allows adjustment of up to four channels with delays down to 5 ps resolution and pulse amplitudes up to 5 V. The DG645 was connected to other equipment via coaxial cables and to the computer via a GPIB interface.

#### 3. **Delay Lines**

Two motorized optical delay lines (Thorlabs and Newport) were used to vary the path length of laser pulses. Each delay line included a motorized translation stage with sub-micron positioning accuracy (0.1 μm), corresponding to sub-femtosecond temporal resolution. The devices were controlled through their native controllers using proprietary wired interfaces.

#### 4. **Motorized Rotation Stages**

Motorized rotation stages (Newport) were used to control the polarization and power of the pump pulses (via waveplates and attenuators). These stages were controlled via the Newport XPS-D4 motion controller. Prior to data acquisition, a calibration table was created to relate the angular positions of the stages to the actual polarization states and power levels of the pump beams.

#### 5. **Newport XPS-D4 Motion Controller**

A universal motion controller capable of operating up to four single-axis Newport servomotors. It was used to control both the optical delay lines and the motorized rotation stages. Communication with the computer was established via Ethernet.

#### 6. Pi Controller (Thorlabs)

A single-axis servo controller used to control one of the delay lines. It was also connected to the computer via Ethernet.

#### 7. Lock-in Amplifier (SRS 830)

Two lock-in amplifiers were used to detect signals from a balanced photodetector, measuring both overall transmittance and polarization rotation. The reference frequency was derived from a chopper placed in the pump beam path. Constant auxiliary outputs (AUX) of the lock-in amplifier were used to control additional equipment, such as the electromagnet. Communication and data logging were performed via a GPIB connection.

#### 8. Electromagnet

An electromagnet with movable pole pieces was used to control the magnetic field applied to the sample. This adjustability of the cavity was essential for measurements at both room temperature and cryogenic conditions. The magnetic field could be switched between opposite directions without reconfiguring the setup. The magnetic field strength was defined by a constant voltage output from the lock-in amplifier.

#### 9. **Mechanical Shutter**

In single-shot experiments, a chopper is not suitable for blocking the pump pulses, so a mechanical shutter was used instead. A constant 5 V signal from the DG645 delay generator triggered the shutter, which had a switching time of ~50 μs. This approach allows for arbitrarily long delays between individual laser shots.

#### 10. CCD Camera (CoolSnapHO)

A high-resolution monochrome CCD camera was used to acquire 2D spatial profiles of the sample's surface. With a resolution of approximately 1400×1200 pixels and a 10× macro lens, spatial resolution of ~7 μm was achieved. A square trigger signal synchronized the shutter for single-shot imaging. The camera communicated with the computer via USB.

#### **Temperature Controller (ITC5035)** 11.

thermocouple and ITC5035 temperature controller Instruments) were used to control the sample temperature inside the cryostat. The controller supports feedback regulation with an accuracy of 0.1 K. It was operated via GPIB directly from the computer.

The software part of the automation system was implemented in LabView, using an object-oriented programming approach. This modular architecture allowed for a unified control structure: when the hardware configuration changed, it was sufficient to implement a new driver (e.g., for delay lines or rotation stages), without rewriting the main program. The control software was based on a feedback loop and enabled long-term measurements (up to several days) under stable and controlled experimental conditions.

The logic of stroboscopic measurement automation followed these steps:

#### 1. Initial calibration

Prior to starting the automated sequence, calibration data were recorded manually. These included the response of the balanced photodetector, attenuator settings, electromagnet output, and the temporal overlap of pump and probe pulses.

#### 2. Temperature stabilization

The desired sample temperature was set from the computer. Since temperature stabilization could take significant time, this step was performed first.

#### 3. Setting external parameters

Once the temperature was stabilized, the following experimental parameters were sequentially set: external magnetic field; polarization of pump pulses; pump pulse power; initial pump-probe time delay.

#### 4. Data acquisition

The mechanical shutter was opened, and a series of measurements was performed while scanning the delay line.

#### 5. Looping

After the measurement series was complete, the shutter was closed, and the next set of external parameters was applied according to the experimental protocol.

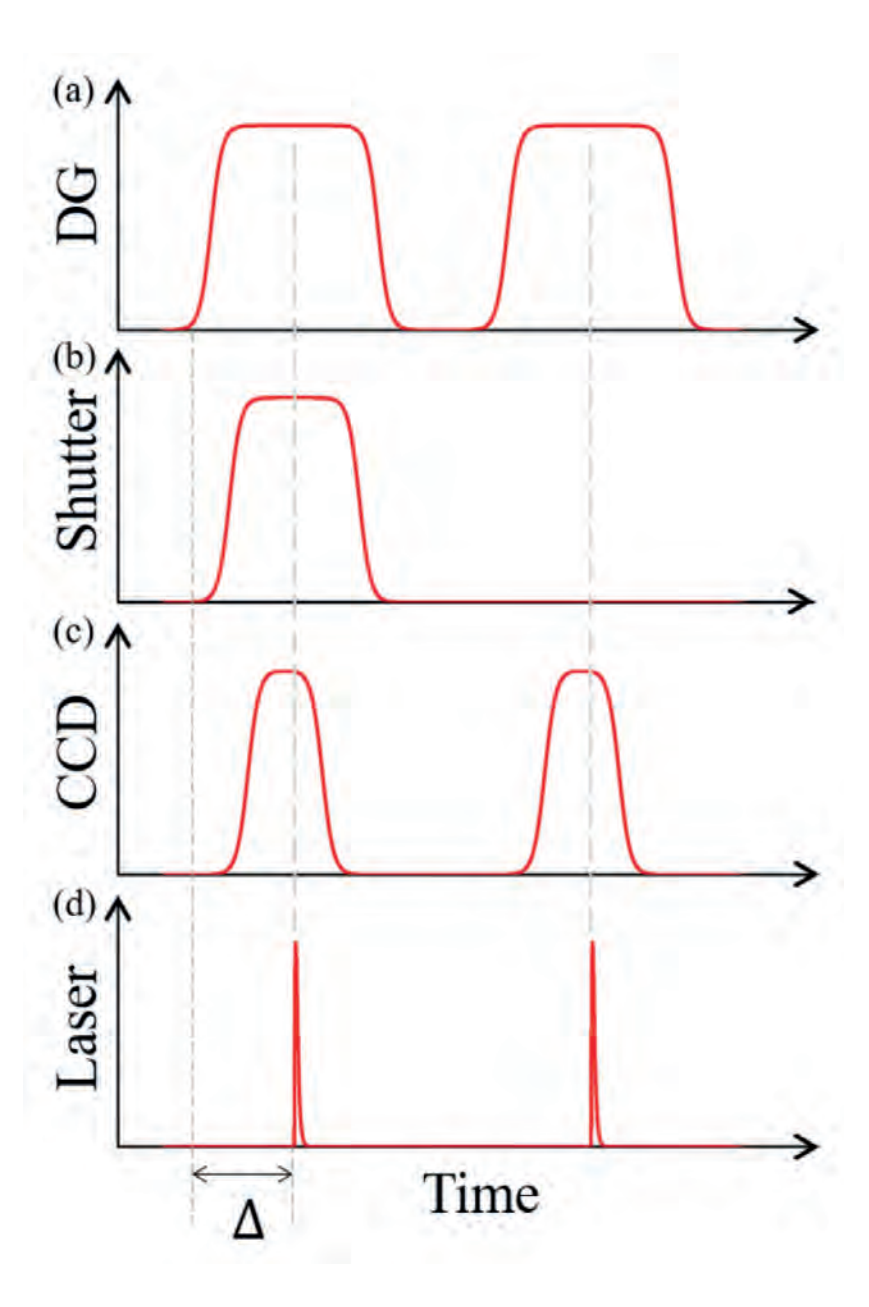


**Fig. 2.6.** Time diagram of the experiment. One cycle consists of two control pulses from the DG645 (a). The first pulse closes the shutter, blocking the pump pulse to create a reference frame (b). During the second pulse, the shutter is open. The CCD camera reads out the signal from the sensor array during the short interval defined by the control signal (c). The DG645 also sends a trigger to the laser system with a time delay  $\Delta$  to compensate for the response times of the shutter and the CCD camera (d).

The automation of single-shot measurements followed a similar structure with kev modifications:

- 1. Parameters initialization
  - External conditions such as temperature, magnetic field, pump polarization and power were set as described above.
- 2. Trigger synchronization
  - The digital delay generator (DG645) was responsible for generating trigger signals for: the mechanical shutter (opened first due to its long response time); the CCD camera; the laser pulse. These signals were nested in time (see Fig. 2.6), ensuring precise synchronization.
- 3. Reference measurements To obtain a reference (unpumped) state, the shutter was kept closed.
- 4. Data acquisition
- 5. Looping

Although photon accumulation in the CCD camera occurs over microseconds, background noise remained minimal, since the dominant source of illumination was the laser pulse itself.

## Literature

- [1] K. Sato and T. Ishibashi, Fundamentals of magneto-optical spectroscopy, *Frontiers in Physics* 10, 946515 (2022).
- [2] L. D. Landau, J. S. Bell, M. Kearsley, L. Pitaevskii, E. Lifshitz, and J. Sykes, *Electrodynamics of continuous media*, Vol. 8, (2013).
- [3] T. H. Johansen and D. V. Shantsev, Magneto-optical imaging, Vol. 142, (2012).
- [4] E. B. Aleksandrov and V. S. Zapasskii, Laser magnetic spectroscopy, Moscow Izdatel Nauka (1986).
- [5] K. Yuksel, M. Wuilpart, V. Moeyaert, and P. Mégret, Optical frequency domain reflectometry: A review, 2009 11th International Conference on Transparent Optical Networks, pp. 1-5, (2009).
- [6] O. Morozov, I. Nureev, A. Sakhabutdinov, A. Kuznetsov, G. Morozov, G. Il'in, S. Papazyan, A. Ivanov, and R. Ponomarev, Ultrahigh-resolution optical vector analyzers, *Photonics*, p. 14, (2020).
- [7] J.-Y. Bigot, M. Vomir, and E. Beaurepaire, Coherent ultrafast magnetism induced by femtosecond laser pulses, *Nature Physics* 5 (7), 515-520 (2009).
- [8] A. Kirilyuk, A. V. Kimel, and T. Rasing, Ultrafast optical manipulation of magnetic order, Reviews of Modern Physics 82 (3), 2731-2784 (2010).
- [9] L. Avilés-Félix *et al.*, Single-shot all-optical switching of magnetization in Tb/Co multilayer-based electrodes, *Scientific reports* 10 **(1)**, 5211 (2020).
- [10] T. Zalewski and A. Stupakiewicz, Single-shot imaging of ultrafast all-optical magnetization dynamics with a spatiotemporal resolution, *Review of Scientific Instruments* 92 **(10)** (2021).

# CHAPTER 3

# Magneto-optical diffraction of visible light as a probe of nanoscale displacement of domain walls at femtosecond timescales

In this Chapter, we used the magneto-optical diffraction of femtosecond laser pulses of visible light by a pattern of magnetic domains in iron garnet as a probe for the domain-wall dynamics. In this method, the femtosecond laser (pump) pulse launches magnetic dynamics. If the sample is initially in a labyrinth multidomain state, another fs linear polarized laser pulse (probe) gets diffracted by the pattern of magnetic domains. Even small changes in the relative sizes of domains with opposite magnetizations result in changes in the diffraction pattern. Measuring the intensity of the third concentric ring of the diffraction pattern, we demonstrated that the signal-to-noise ratio is high enough to detect 6 nm domain wall displacement even with the help of visible light, having 100 times longer wavelength. Using a femtosecond laser pulse as a pump, we showed that it is possible to detect the domain-wall dynamics with 100 fs temporal resolution. We also discuss possible artefacts that can affect the measurements. For instance, one must be aware of the fact that similar changes of the diffracted pattern can also be caused by pump-induced changes of the optical properties in the spectral range of the probe pulse.

Adapted from: A. Dolgikh, T.B. Shapaeva, K.T. Yamada, M.V. Logunov, T.H. Rasing and A.V. Kimel, "Magneto-optical diffraction
of visible light as a probe of nanoscale discplacement of domain walls at femtosecond timescales", Review of Scientific
Instruments 94(10), 2023

#### 3.1 Motivation

Spin textures and dynamics of domain walls in magnetic media have long been one of the hottest topics in magnetism [1-3]. Understanding domain wall dynamics is widely recognized to have a potential to impact future technologies and the development of race track memory, in particular [4-7]. Fundamentally, understanding domain wall dynamics appears to be a cornerstone in many heavily debated topics, including ultrafast phase transitions, ultrafast magnetism, and spintronics [8-12].

Visualization of domain walls and domain wall dynamics is usually realized by employing various conventional optical [13,14], scanning [15-17] or near-field scanning microscopes (SNOM) [18]. Optical observations are based on magnetooptical effects such as the Faraday rotation (in transmission) or the Magneto-optical Kerr effect (MOKE) in reflection. Upon propagation of linearly polarized light through magnetic domains with opposite magnetization, the polarization of light will rotate over the angles  $+\theta$  and  $-\theta$ , respectively. Therefore, by putting the sample between two polarizers and adjusting the axes of the polarizers such that the angle between them is  $\frac{\pi}{2}-\theta$  we can visualize the magnetic domains in the medium. The domains rotating the polarization over the angles  $+\theta$  and  $-\theta$  will be seen under a polarized microscope as dark and bright areas, respectively. In general, spatial resolution in optical imaging is limited by the Abbe diffraction limit, which depends on the wavelength of the light used:

$$D = \frac{\lambda}{2n} \tag{3.1}$$

where  $\lambda$  is the wavelength of the electromagnetic wave in a vacuum, and n is the refractive index of the medium. The linear size D determines the minimum size of an object distinguishable using conventional optics. Certainly, if n=1, the use of visible light (i.e. light with wavelength in the range 380 nm <  $\lambda$  < 780 nm) will not allow the study of objects smaller than 190 nm.

The best temporal resolution in optical imaging is achieved with the help of pulsed light sources and ultimately limited by the duration of the light pulses. Recent developments of femtosecond X-ray laser sources have greatly boosted the interest in experimental studies of magnetic domain walls and domain wall dynamics with nm spatial and sub-ps temporal resolution [2]. However, the presence of (a regular pattern of) domains and domain-wall dynamics can also be studied by optical diffraction: polarization components, which are orthogonal with respect to the

polarization of the incident light, interfere, resulting in a diffraction pattern. Such magneto-optical diffraction has been shown to be an efficient tool to explore domain patterns and their dynamics in magnetic materials [19-21]. For example, using the diffraction of light from a continuous-wave laser at the wavelength of 632.8 nm has allowed us to detect domain wall displacements in an iron garnet with a spatial resolution down to 5 nm [22]. Of course, for such diffraction to occur, the size of the domains should exceed the wavelength of the probe. It is, therefore, of interest that a similar method has recently been realized with fs pulses of X-ray radiation, where the diffraction pattern and its time evolution gave direct information about the relative sizes of domains and the domain-wall dynamics, in particular [23-27].

In this chapter, we conducted a study of the laser-induced dynamics of the domain structure of lutetium garnet using the diffraction method. Similar previous studies on domain wall motion in garnets were limited either to a single degenerate boundary [28] or to weak

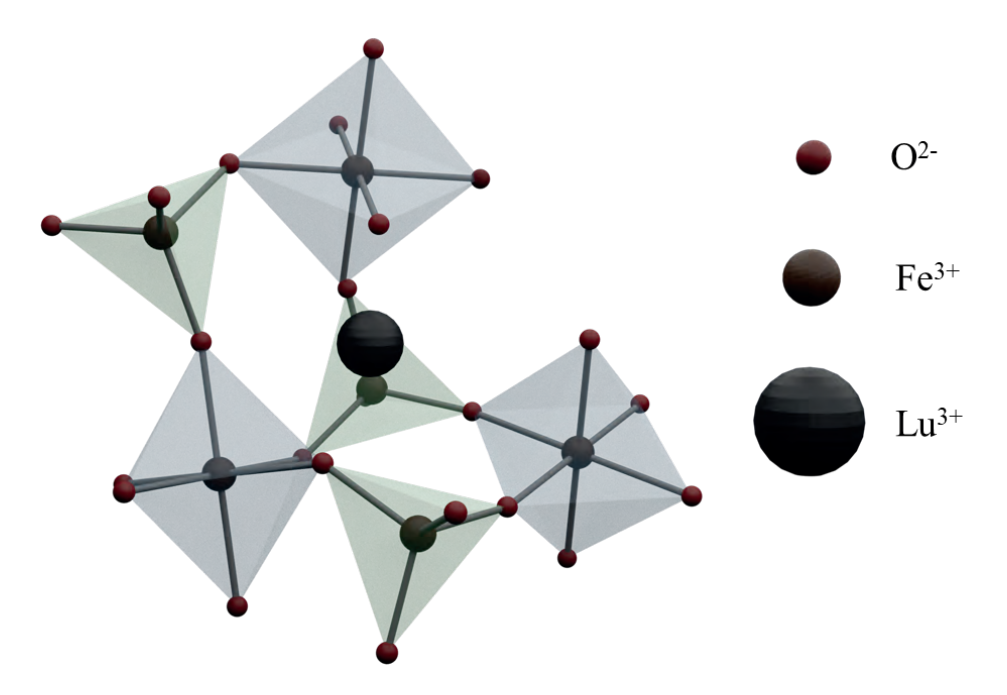


**Fig. 3.1**. Structure of iron-garnet. Iron ions Fe3+ are in tetrahedral and octahedral sublattices, surrounded by O2-. Non-magnetic rare-earth ions of Lu3+ are in dodecahedral positions (not shown).

temporal resolution not exceeding nanoseconds [29]. In the present work, we will experimentally study the average speeds of domain wall motion in the sample with an unperturbed domain structure. The study of multiple domain walls has

significantly improved the spatial accuracy of measurements, surpassing the diffraction limit of measurements, and the use of the pump-probe technique has provided sub-picosecond time resolution.

# 3.2 Sample

The sample studied here was an epitaxial film of iron garnet (Bi,Lu)<sub>3</sub>(Fe,Ga,Al)<sub>5</sub>O<sub>12</sub> with a thickness of  $h = 8.3 \,\mu m$ . The magnetic subsystem is formed by iron ions Fe<sup>3+</sup> in a state with a total spin of S = 5/2. Figure 3.1 shows a simplified crystal structure of iron garnet. The Fe<sup>3+</sup> ions are in two crystallographic positions: octahedral and tetrahedral. Pairs of the nearest neighbors in octahedral and tetrahedral positions are connected through an oxygen cation, leading to strong indirect antiferromagnetic exchange interaction. The total number of iron ions in the two sublattices is not compensated, with a ratio of 3:2 of atoms in the tetrahedral to the atoms in the octahedral position. Thus, such an iron garnet is a ferrimagnet. Bi3+, Lu<sup>3+</sup> ions are located in the dodecahedral position. Selective substitution of iron ions by nonmagnetic ions (Ga<sup>3+</sup> and Al<sup>3+</sup>) allows changing the ratio of the number of iron ions in the two sublattices. Both nonmagnetic atoms can replace iron in both the tetrahedral and octahedral positions [30,31]. By controlling the conditions for the substitution of iron ions, different magnetic properties can be tuned: anisotropy and the Curie temperature [32,33].

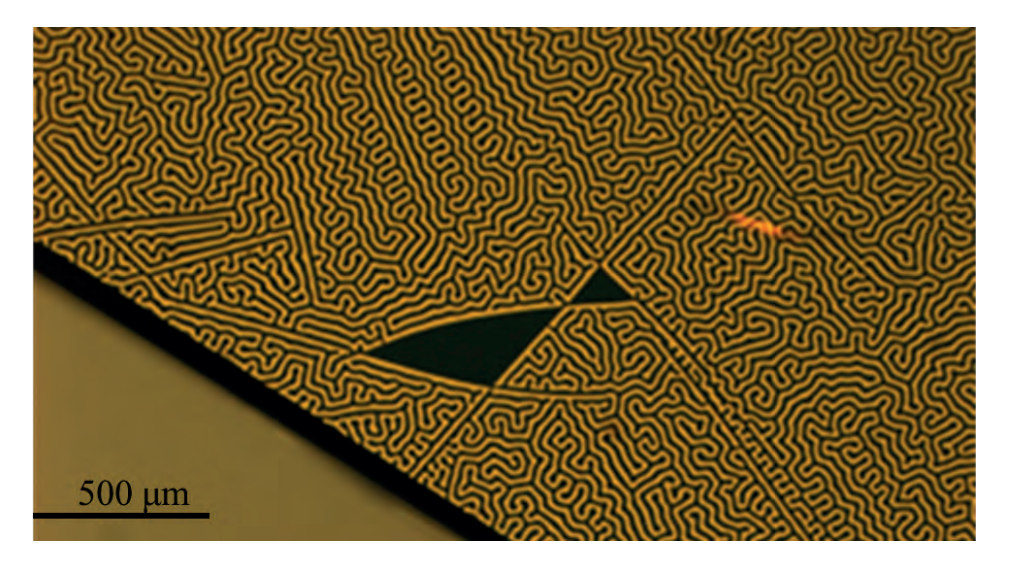


Fig. 3.2. Domain structure of the sample observed with the polarized microscope. Black and yellow colours correspond to the domains with opposite magnetizations. The width of the domains is 16 µm.

The sample has a relatively low saturation magnetization  $4\pi M_s=97{\rm G}$  but has a strong magnetocrystalline anisotropy with the easy magnetization axis along the normal to the sample. The anisotropy field is as large as  $H_a=5.5$  kOe. If the external magnetic field is applied along the anisotropy axis, the sample reveals a very low coercive field of  $H_c<0.7$  Oe [34]. The sample is transparent for the wavelength used in the experiment (632 nm), allowing optical measurements in transmission [35].

The magnetic structure of the sample breaks down into randomly arranged domains with opposite directions of magnetization (Fig. 3.2). A polarizing optical microscope was used to observe the domain pattern. Linearly polarized light illuminated the sample. Depending on the direction of magnetization in the domain, the polarization of the incident light rotates clockwise or counterclockwise. The analyzer of the polarizing microscope was set so that the light passing through the domains of one type was completely blocked. Thus, some domains are colored black and others yellow (this is related to the color of the sample itself). Such a domain structure is called labyrinthine and was also observed in other garnets [36-38]. An important feature of the labyrinthine domain structure for our measurements is the diffraction pattern represented by concentric rings [22,39,40], which is ideal for our experiment. The period of the equilibrium labyrinth domain structure is  $P_0=32\,\mu\mathrm{m}$ . Applying the external magnetic field of  $H_0=32$  Oe turns the labyrinth domain structure into a cylindrical one [29].

# 3.3 Magneto-optical diffraction

The observation of magnetic domains is not solely restricted to direct methods. By employing linearly polarized incident light, it is possible to observe a diffraction pattern. When light passes through magnetic domains, its polarization is rotated by the Faraday effect. This new polarization component, oriented perpendicular to the original one, produces the diffraction pattern. To detect this pattern, a polarizer must be placed after the sample, oriented orthogonally to the initial polarization direction of the incident light. In this section of the chapter, we describe how this diffraction appears. We first discuss a single period composed of two domains with opposite magnetization directions and then extend the discussion to a two-dimensional domain structure.

## 3.3.1 Diffraction on a single domain pair

We first consider a thin, non-transparent, two-dimensional film with a hole in the middle. Two magnetic domains with opposite out-of-plane magnetizations fill this hole, and their sizes are the same (see Fig. 3.3 (b)). Coherent linearly polarized light

falls on this system at normal incidence. We consider light propagating along the z-axis and its electric field along the y-axis. We assume that the domain wall between these domains is infinitely narrow, which is quite close to reality since, in our sample, the size of the domains is around 16000 nm, while the domain walls are only 50 nm [3]. Upon propagation of light through the magnetic structure, the polarization of the light  $\mathbf{E}_0(0,1,0)$  continuously rotates due to the Faraday effect (Eq. 2.11).

One domain rotates the polarization over angle  $+\theta \mathbf{E}_1 (\sin\theta, \cos\theta, 0)$ , while another over angle  $-\theta \mathbf{E_2} \left(-\sin\theta,\cos\theta,0\right)$  -9  $\mathbf{E_2}$  (Fig. 3.3(a)). In this way, the y-components of the electric field of light after interaction with the domains are the same and do not participate in the diffraction. On the contrary, the x-components of the electric field have different signs and can be described as:

$$E_x = \left\{ egin{array}{ll} 0, & ext{if } x \leq -s \, ext{or} \, x > +s, \ +E_0 \cdot \sqrt{\exp\left(- ext{ah}
ight)} \cdot \sin\left( heta
ight), & ext{if } -s < x \leq 0 \ -E_0 \cdot \sqrt{\exp\left(- ext{ah}
ight)} \cdot \sin\left( heta
ight), & ext{if } 0 < x \leq +s. \end{array} 
ight.$$

Where  $\exp(-ah)$  defines the absorption of the material, a - absorption coefficient. We assume that the absorption in the domains with opposite magnetization is the same. After the normalization of equations (3.3), we get a normalized Faraday rotation function:

$$g(x) = \begin{cases} 0, & \text{if } x \le -s \text{ or } x > +s, \\ +1, & \text{if } -s < x \le 0, \\ -1, & \text{if } 0 < x \le +s. \end{cases}$$
(3.3)

The resulting normalized Faraday rotation function is shown in Fig. 3.3(b). Its values correspond to the rotation of the plane of polarization of incident light counterclockwise and clockwise, respectively.

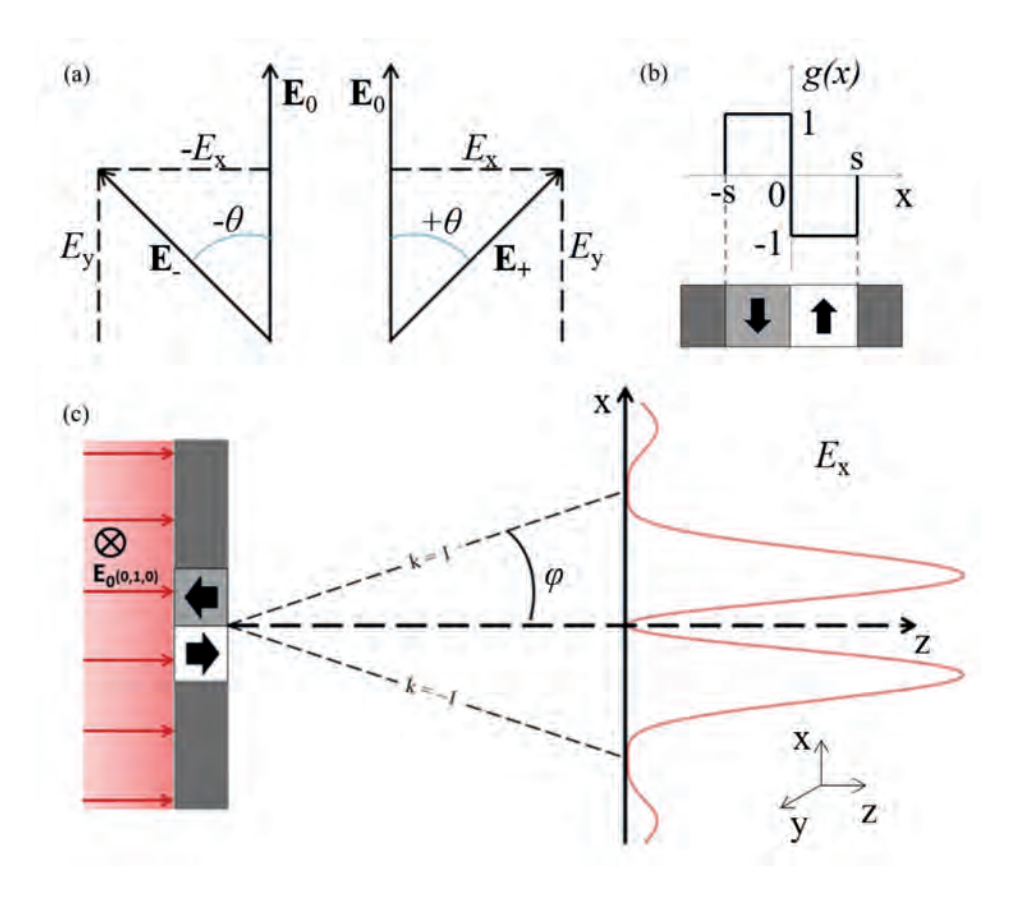


**Fig. 3.3**. (a) Faraday rotation by the domains with opposite magnetizations. Incoming light is linearly polarized along the y-axis. (b) The hole in a non-transparent material filled in with two domains with opposite magnetizations and the corresponding Faraday function. 1 and -1 mean clockwise and counterclockwise rotation of the polarization on the same angle. (c) A diffraction pattern is observed on such a hole with two domains in the polarization component, which is orthogonal to the polarization of the incoming light.

If we consider only the component of the transmitted light, the polarization of which is orthogonal to the polarization of incident radiation, then at an arbitrary angle  $\varphi$ , we can get the following relationship determining the diffraction angles of light on two domains:

$$P_0 \sin \varphi = \mathbf{u}\lambda \tag{3.4}$$

where  $u=0,\pm 1,\pm 2,\ldots$  is the diffraction order, and  $\lambda$  is the wavelength of light.  $P_0=2s$  is the period of the domain pattern. For a symmetric phase diffraction

grating, as depicted in Fig. 3.3(c), even diffraction orders are absent, i.e., the diffraction intensity is zero at  $u=0,\pm 2,\pm 4,\ldots$ 

Performing the Fourier transform of the transmission function, we obtain the intensity profile of light with the electric field along the x -axis:

$$I_{x}\left(u\right) = I_{0} \cdot \exp\left(-\operatorname{ah}\right) \cdot \sin^{2}\left(\theta\right) \cdot \frac{2s^{2}}{\pi} \cdot \left(\frac{\cos\left(2\operatorname{us}\right) - 1}{2\operatorname{us}}\right)^{2} \tag{3.5}$$

In essence, formula (3.4) serves as an envelope for the diffraction pattern that arises when considering multiple periods of the domain structure. It's important to note that, in our case, as with most, the Faraday rotation is less than 90°. As a result, at the output of the crystal, the light wave has two components,  $E_y$  and  $E_x$ .

All the y-components share the same phase, which means this component of the light wave propagates along the z-axis after leaving the crystal and does not convey any information about the domain structure. In other words, the intensity of radiation polarized along the y-axis simply represents background illumination. Thus, in the zeroth order of diffraction, the light will be polarized solely along the y-axis. The intensity of radiation in the zeroth order of diffraction is determined as follows:

$$I_{y,0} = I_0 \exp\left(-\text{ah}\right) \bullet \cos^2\left(\theta\right) \tag{3.6}$$

#### 3.3.2 Periodic one-dimensional domain pattern as a phase grating

Now, let's move to the stripe domain structure shown in Fig. 3.4. The incident light is also linearly polarized along the y-axis and propagates along the z-axis. But now, instead of two domains with opposite magnetizations, we consider a periodic structure.

The amplitudes of the waves reaching an arbitrary point on the screen from each period are equal, but the phase difference between the waves coming from neighboring periods equals  $\frac{2\pi P}{\lambda} \sin \varphi$ . To obtain the disturbance sent by the entire domain system, it is necessary to sum over all periods. In this case, the intensity of the u-th order diffraction is determined as follows:

$$I_{x}\left(u\right) = I_{0} \cdot \exp\left(-\operatorname{ah}\right) \cdot \sin^{2}\left(\theta\right) \cdot \frac{2s^{2}}{\pi} \cdot \left(\frac{\cos\left(2\mathrm{u}s\right) - 1}{2\mathrm{u}s}\right)^{2} \cdot \left(\frac{\sin\left(2\mathrm{Nu}s\right)}{\sin\left(2\mathrm{u}s\right)}\right)^{2} \tag{3.7}$$

where N is the number of domains. The position of the diffraction orders is determined by  $2\mathbf{u}s=\pi\mathbf{n},\mathbf{n}\in Z$ . It should be noted that for unbalanced values of  $s_1$  and  $s_2$ , the formula will undergo some changes:

$$I_{x}\left(u\right) = I_{0} \cdot \exp\left(-\text{ah}\right) \cdot \sin^{2}\left(\theta\right) \cdot \frac{2s^{2}}{\pi} \cdot \left(\frac{\cos\left(2us_{1}\right) - 1}{\text{uP}}\right)^{2} \cdot \left(\frac{\sin(2\text{Nu}s_{1})}{\sin\left(\text{uP}\right)}\right)^{2} \quad (3.8)$$

Fig. 3.4 shows the *y*-component of the transmitted light calculated using Equation (3.3), and the *x*-component calculated using Equation (3.9), assuming domains of equal size. At the same time, the single-period envelope has a minimum when  $2\mathbf{u}s=2\pi\mathbf{k},\mathbf{k}\in Z$ . Thus, when  $\mathbf{u}=0,\pm2,\pm4,\ldots$  diffraction orders are suppressed, and the total intensity is equal to zero. Upon a transition to a two-dimensional case with a labyrinth domain structure, the derivations are very similar, but instead of a stripe diffraction pattern, we would expect to observe a concentric ring.

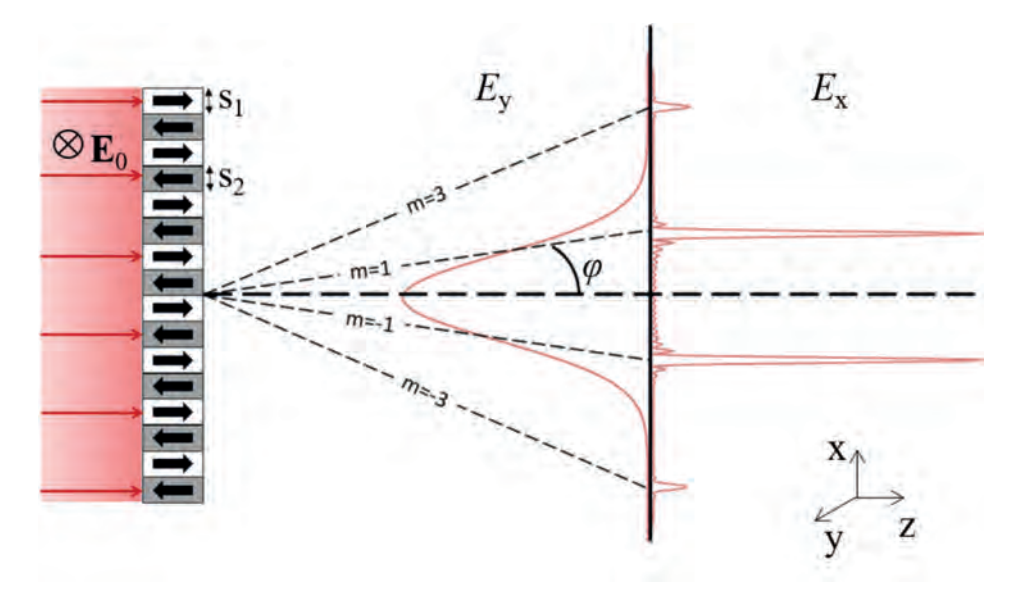


**Fig. 3.4.** Magneto-optical diffraction on the array of alternating domains. Incoming light is linearly polarized along the y-axis.

If we consider a two-dimensional labyrinth domain structure, this will not affect the formulas derived earlier. The diffracted light simply forms concentric circles instead of a linear diffraction pattern. The radiation intensity in the first order equals  $I_1+I_{-1}$ , and that in the second order equals  $I_2+I_{-2}$ , etc. Also, in the two-dimensional distribution of magnetic domains, due to multiple variations in the orientation of these domains, the diffraction maxima broadens, which affects the sensitivity of the method. In Fig. 3.5, you may see the diffraction pattern observed on our sample without an external magnetic field. One can clearly distinguish the symmetry of the pattern. The y-component of the polarization was suppressed with a polarizer. In our image, we can observe an uneven distribution of intensity in the third diffraction order. This indicates a deviation from an isotropic distribution of domains in the sample. We believe this is related to the presence of defects (such as scratches) in the ferrite-garnet film, causing a small portion of domains in certain areas of the sample to align along one direction. Utilizing a defect-free film will enable increased measurement accuracy.

If we consider measurements of the integral intensity of one of the diffraction maxima, then we need to use a spatial filter to block all other maxima. If the spatial filter separates the third diffraction order within the borders of  $\varphi=\varphi_A$  and  $\varphi=\varphi_B$  as shown in Fig. 3.5, the integral intensity can be calculated as follows:

$$f(s) = \int_{\varphi_A}^{\varphi_B} \left( \frac{\cos\left(\frac{2\pi s \sin(\varphi)}{\lambda}\right) - 1}{\frac{2\pi s \sin(\varphi)}{\lambda}} \right)^2 \left( \frac{\sin\left(\frac{2N\pi s \sin(\varphi)}{\lambda}\right)}{\sin\left(\frac{2\pi s \sin(\varphi)}{\lambda}\right)} \right)^2 d\varphi$$
(3.9)

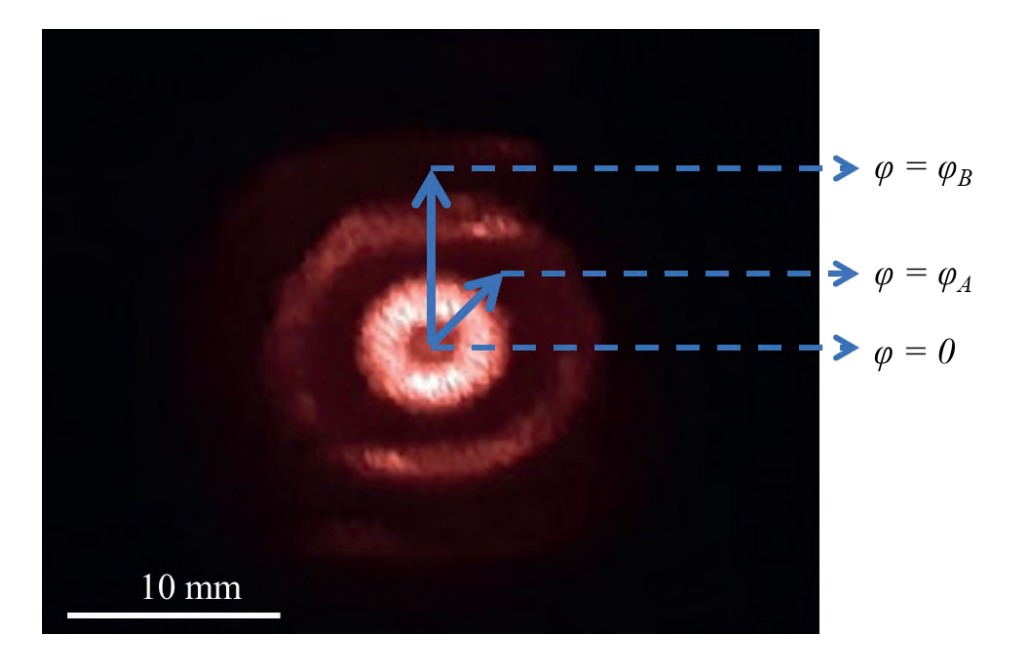


**Fig. 3.5.** The diffraction pattern for coherent light at a wavelength of 632 nm is formed by a labyrinth domain structure. The spatial filter separates the 3<sup>rd</sup> diffraction order within the borders  $\varphi_A < \varphi < \varphi_B$ .

## 3.4 Experimental details

To study the ultrafast dynamics of magnetic domains via magneto-optical diffraction, we employed the principles of a pump-probe technique. In particular, we used amplified light pulses from a Ti:sapphire laser with a duration of 40 fs and a central wavelength of  $\lambda$  = 800 nm (photon energy 1.55 eV). Each pulse was split into two parts. One part was sent through an optical parametric amplifier (OPA), which shifted the central wavelength of the pulse to  $\lambda$  = 600 nm (photon energy 2.07 eV). This beam, which was used as a probe, was focused on a spot on the sample with a diameter of 120 µm. This spot covers more than seven domains of the sample studied, which is enough to produce a clear diffraction pattern. Another part of the laser beam was used as a pump. Its wavelength remained at  $\lambda$  = 800 nm, and the beam was focused onto the sample in a slightly larger spot with a diameter of 130 µm. In this way, the probe interacts only with sample areas exposed to the pump, which will boost the signal-to-noise ratio. The difference between the pump and the probe wavelengths allows to completely blocking of the pump light after the sample using a cut-off filter. The probe beam reached the sample at normal incidence, while the incidence angle for the pump light was set to 15 deg with respect to the sample normal. Due to the parallax effect between

the pump and the probe, we experience a loss of time resolution compared to the pulse duration (40 fs). The scattering angles for the observed diffraction orders: 1st,  $3^{rd}$  and  $5^{th}$  are equal to 26, 70 and 110 mrad, respectively. A lens with a focal distance of 100 mm placed after the sample collected the diffracted light and collimated it in a beam with a diameter smaller than 2.5 cm, setting an upper limit for the diameters of the optical components of the experimental setup. This choice was determined by the dimensions of the Thorlabs optical components used in this work. Behind the lens, we placed an analyzer and a CCD camera.

When domain boundaries shift, the relationship between the sizes of domains with opposing magnetization directions changes. It has been previously shown that with minor alterations of an external magnetic field, the period of the domain structure remains unaltered [29]. If the period of the domain structure remains constant, the positions of the main maxima in the diffraction pattern don't change either. However, in accordance with equation (3.8), the intensity of the diffraction maxima does change. Thus, by measuring the integral intensity of the maximum/maxima, one can indirectly calculate a change in the relative size of the domains due to a shift of the domain boundaries.

As explained above and similarly to [22], to trace the dynamics of the magnetic domains, we measured the relative changes in the intensity  $\Delta I_{
m m}/I_{
m m}$  of the third diffraction order, where m=3. This method enables us to conduct measurements using a single photodetector and a box-car integrator synchronized with the laser pulses. To improve the signal-to-noise ratio, the detection system operates at the pump frequency and measures the pump-induced signal as the difference of the signals from a pump-perturbed and an unperturbed sample, respectively. In principle, incorporating a synchronized camera with a high dynamic range can enable simultaneous measurement of all diffraction maxima, strongly reducing the time required to perform the experiments and corresponding calibrations. If initially the average width of domains with the magnetization pointing "up" is equal to s, its relative change  $\Delta s/s$  would result in an intensity change  $\Delta I_3/I_3$ and the sensitivity of the method will be defined by the ratio  $(\Delta I_3/I_3)/(\Delta s/s)$ . For instance, using light of a continuous-wave laser at the wavelength of 632.8 nm it was shown that increasing the width of one type of domain  $\Delta s/s$  by 2% leads to a change in the light intensity in the third diffraction order  $\Delta I_3/I_3$  by 4%.

To separate the third-order diffraction maximum, we used a spatial filter (Fig. 3.6(a)) consisting of a ring-shaped hole in a plastic plate. The spatial filter was fabricated with the help of 3D printer, and for every sample, a unique filter must be custom-made. The internal and external radii of the ring were 6 mm and 10 mm, respectively. Thus, the first and the fifth diffraction orders were blocked. To

minimize the possible influence of scattered light, we cut the hole corners from the side facing the incident light. In this way, we blocked much of the pattern but detected the integral intensity of the 3<sup>rd</sup> diffraction order.

The resulting diffraction ring was focused on a single-element photodetector. This technique allows measurements using a single photodetector and a box-car integrator. The detection system functions at the pump frequency and measures the relative change in the pump-induced signal relative to the signal from the undisturbed state, yielding a high signal-to-noise ratio.

In a classic pump-probe experiment, it's necessary to restore the sample to its initial state between each pump pulse. However, when studying the overall change in the domain pattern in a sample, such as the ratio of the sizes of one domain to another, we don't need precise control over the initial state. To reproduce the same diffraction pattern, it's sufficient for us to maintain the domain sizes and ensure the pattern maintains labyrinth structure. The structure may recover over time on its own, which is suitable for single-shot experiments [41,42], or an alternating external magnetic field can be applied [43]. We used a pair of Helmholtz coils (Fig. 3.6(b) A) to implement an alternating magnetic field. The coils were about five times bigger than the sample. The sample was placed in the middle, between the coils where the generated magnetic field is the most homogeneous.

Applying exponentially damped sinusoidal magnetic fields with an initial amplitude higher than the field required to saturate the magnetization, we managed to restore the initial diffraction pattern within 20 ms and thus facilitated stroboscopic measurements at a repetition rate of 40 Hz. External Helmholtz coils (Fig. 3.6(b) B) were used to create a static magnetic field maintaining the desired ration of domain width magnetized parallel and antiparallel to the field.

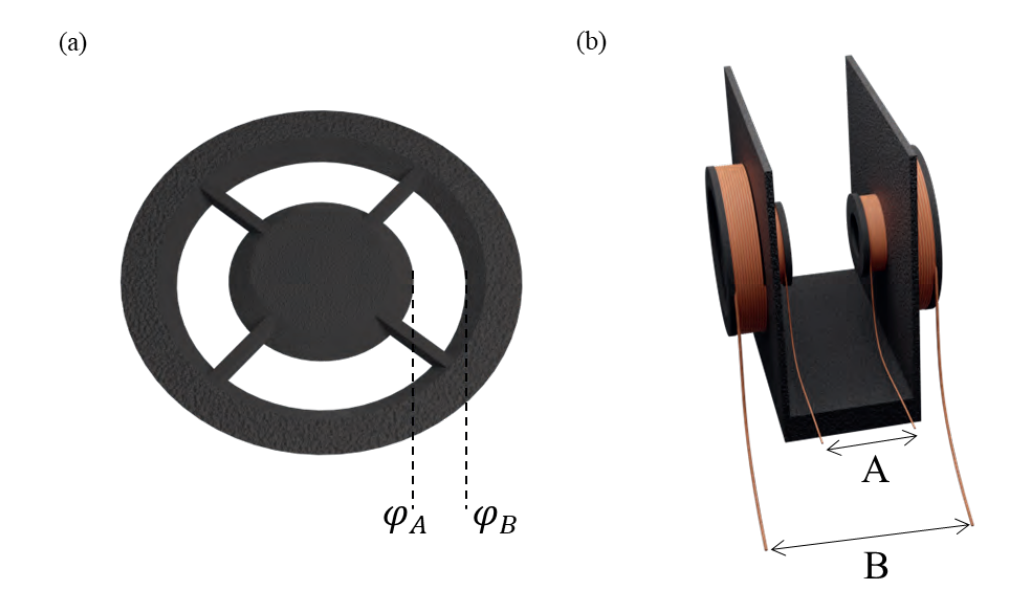


**Fig. 3.6.** (a) Spatial filter for separation of the third diffraction maximum. (b) Helmholtz coils for the generation of a magnetic field along the light propagation direction. The coils in each pair (A or B) are connected in series.

The selection of the third diffraction maximum was not arbitrary. With each succeeding diffraction order, the integral intensity decreases, while the sensitivity to relative domain size changes increases. The intensity of the fifth diffraction maximum was insufficient for stable measurements, while the sensitivity of the first diffraction maximum was significantly lower than that of the third. However, the sensitivity can also be enhanced when measuring a single diffraction maximum. The sensitivity of measurements increases if we change the initial ratio of domain sizes. Figure 3.7(a) shows the dependency of the integral intensity of the first and third diffraction orders on the domain size ratio. Moving away from the initial position, where domain sizes coincide, results in noticeably higher changes in the observed intensity. This graph also shows that even with an imbalance in the sizes of opposing domains, the third diffraction order will be more sensitive than the first one.

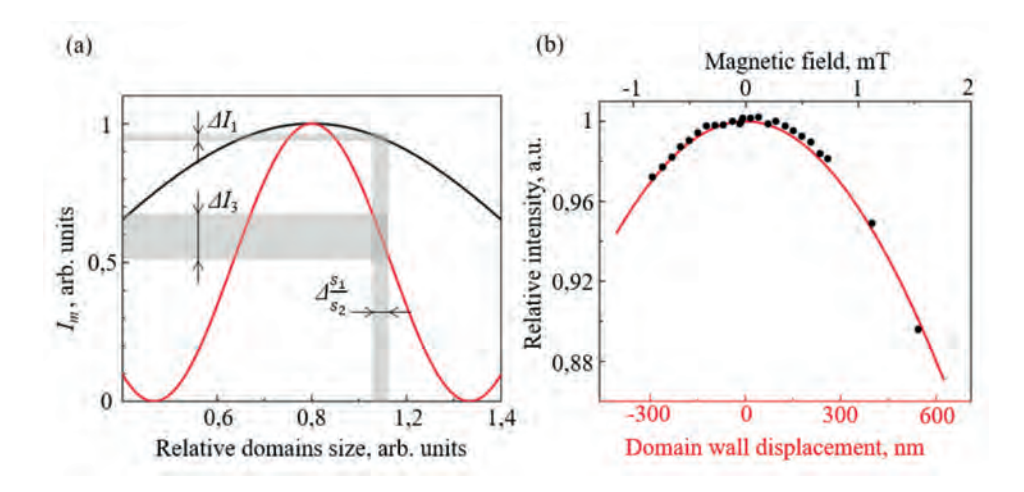


**Fig. 3.7.** (a) Calculated dependences of the normalized intensity of the first and the third diffraction order on the relative domain size. (b) Normalized intensity of the 3<sup>rd</sup> diffraction order. Applying voltage to the Helmholtz coils, we controlled the bias magnetic field and thus changed the relative domain size. The red curve is the theoretical calculation using Eq. 3.8.

To create an unbalanced ratio of opposing domain sizes, we employed an additional pair of Helmholtz coils (Fig. 3.6(b)). These coils were five times larger than the sample's linear dimensions, providing us with a uniform magnetic field in the observed area. Applying a current through the coils, we generated a magnetic field along their axis, thereby increasing the size of domains whose magnetization is aligned along the magnetic field. Figure 3.7(b) shows how a voltage applied to the coils and the corresponding average changes in the domain width  $\Delta h$  results in a change in the intensity of the 3<sup>rd</sup> diffraction order. Note that while the domains with magnetization aligned with the magnetic field are expanding on  $\Delta h$ , the ones with magnetization in the opposite direction are narrowing similarly. The black dots show the experimental data, while the red curve is calculated using Eq. 3.8. For magnetic fields significantly smaller than the saturation field ( $H_{
m ext} \ll H_{
m s}$ ), the period  $P_0$  remains constant [22], and the outcome of Eq. 3.8 is affected only by a change in parameter s<sub>1</sub>, while the other parameters remain unchanged. A drawback of applying a bias voltage to achieve better sensitivity is a nonlinearity of the detection scheme. In particular, a displacement of domain walls over a certain distance in one direction would in principle, result in a stronger signal than the same displacement in the opposite direction.

## 3.5 Results and discussion

Before we performed time-resolved measurements, we estimated the sensitivity of our detection scheme to potential displacements of the domain walls. Using the

data sets obtained at negative time delays, i.e. when the probe arrives before the pump, we estimated the standard deviation of the noise to be  $\sigma=0.3\%$  of the integral intensity in the unperturbed state. Requiring a reliable detection, a signal that is at least three times larger than the noise and assuming a Gaussian noise distribution,  $3\sigma$  will correspond to an error bar with a confidence limit of 99.7%. From Eq. 3.8, we calculated that the minimum domain wall displacement that leads to a  $3\sigma$  change in the intensity of the 3<sup>rd</sup> diffraction order is about 6 nm.

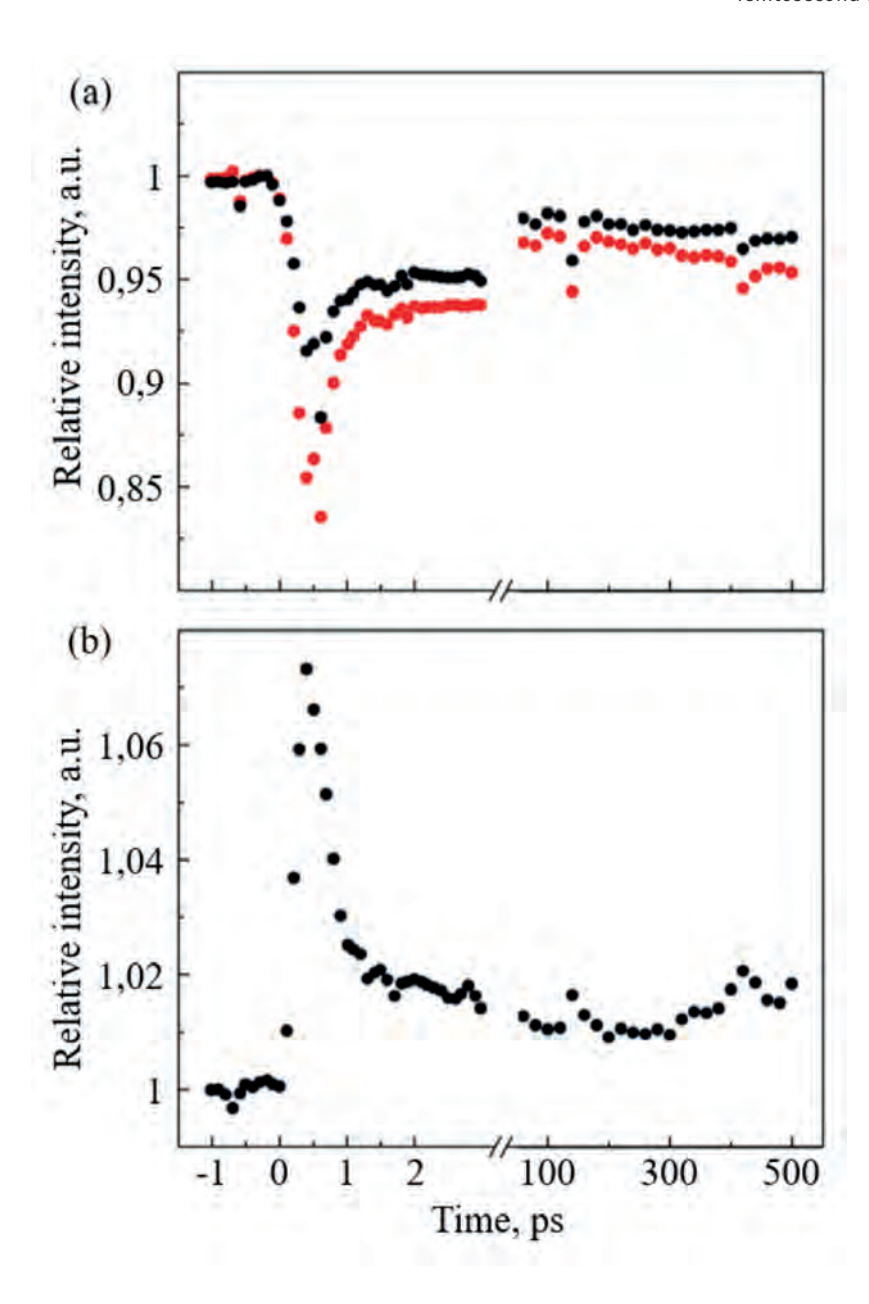


**Fig. 3.8.** (a) Temporal evolution of the integral intensity of the 3rd diffraction order (black dots) and the total intensity of the transmitted light (red dots) after excitation by right-handed circularly polarized pump. (b) Temporal evolution of the integral intensity of the 3rd diffraction order normalized for the intensity of the transmitted light after excitation with right-handed circularly polarized pump excitation. The pump pulse fluence was  $F=0.32J/cm^2$ .

Measuring the integral intensity of the  $3^{rd}$  diffraction order as a function of pump-probe time-delay t, one can trace how the domain pattern evolves as a result of

femtosecond laser excitation. The intensities of the  $3^{rd}$  diffraction order measured at various time delays are normalized to the intensity before the pump arrives at the sample (t < 0 ps), and the results of this are shown in Fig. 3.8(a). This experiment confirms that the described setup can reveal subpicosecond dynamics of the intensity of the  $3^{rd}$  diffraction order. The demonstrated spatial and temporal resolution are very close to those reported in Ref. [27], obtained by diffraction of fs X-ray pulses. The latter claimed the sensitivity to picosecond domain wall displacements as small as 0.7 nm.

From the changes in the intensity of the 3<sup>rd</sup> diffraction order as a function of time delay, we can estimate the domain wall velocity. From Fig. 3.8(a), it is seen that after 1.5 ps, the intensity of the third diffraction order (black dots) changes by 5%. This would correspond to a domain wall velocity of 300 km/s. While nanosecond magnetic pulses were able to launch magnetic-moment-flip waves with speeds up to 55 km/s in iron garnets [44], a domain wall motion with the speed of 300 km/s seems to be somewhat unrealistic. It is, therefore, important to realize that not only the domain wall displacement can affect the intensity of the diffraction pattern. Due to an intense pump pulse, the optical properties and the Verdet constant of a medium can change, resulting in a change in the intensities of the diffraction maxima (see Eq. 3.8) [45], even when the magnetic domain pattern would remain unaffected. To compensate for at least one of the possible artifacts, we measured the dynamics of the total transmission of the probe light through the sample (the results of this are also shown in Fig. 3.8(a)). The dynamics of the total intensity of the probe light (red dots) after the pump excitation gives us a measure of the transient absorption in the medium. From Fig. 3.8(a), it can be seen that the intensity of the light transmitted through the sample changes considerably. We, therefore, normalized the intensity of the 3<sup>rd</sup> diffraction order with respect to the total intensity. The results of this normalization are shown in Fig. 3.8(b)). This procedure does not take into account the potential pump-induced changes in the Verdet constant. The normalized changes in the intensity of the 3<sup>rd</sup> diffraction order by 2.5% after 1 ps correspond to domain wall displacements over 100 nm and thus imply a domain wall velocity of 100 km/s.

It should be noted that for more than two decades, the controversy in the interpretation of experiment results in ultrafast magnetism has been caused by pump-induced changes in the magneto-optical constant [46-48]. In order to disentangle the dynamics of ultrafast magnetization and the magneto-optical constants, we would need to perform experiments in a broad spectral range of probe pulse [49], for instance. Another way to resolve this controversy is to use pump pulses that do not affect the magneto-optical constant, such as ultrashort pulses of magnetic field [50], electric current [51], or even spin current [52].

#### 3.6 Conclusions

In this study, we demonstrated a proof of concept of a table-top setup for time-resolved measurements of domain walls displacement with subpicosecond temporal and nanometer spatial resolutions. The technique employs visible light, the principles of magneto-optical diffraction and pump-probe measurements. Though the present experiments involved labyrinth domains in transparent garnets, a similar approach can be used for the study of domain dynamics in opaque metallic films, using the magneto-optical Kerr effect in reflection. We show that if the domain wall dynamics is triggered by a near-infrared femtosecond laser pulse, the technique can be affected by artifacts due to pump-induced changes in optical absorption and the magneto-optical Verdet constant. It is expected that for the case when the pump is in the form of an ultrashort pulse of magnetic field, electric current or spin current, the application of the method should be free of these artifacts and thus more reliable.

#### Literature

- [1] A. P. Malozemoff and J. C. Slonczewski, Magnetic domain walls in bubble materials: advances in materials and device research, Vol. 1, (2013).
- [2] J. Stöhr and H. C. Siegmann, Magnetism, Vol. 5, (2006).
- [3] A. Hubert and R. Schäfer, Magnetic domains: the analysis of magnetic microstructures, (2008).
- [4] S. S. Parkin, M. Hayashi, and L. Thomas, Magnetic domain-wall racetrack memory, science 320 (5873), 190-194 (2008).
- [5] J. Vandermeulen, B. Van de Wiele, L. Dupré, and B. Van Waeyenberge, Logic and memory concepts for all-magnetic computing based on transverse domain walls, *Journal of Physics D: Applied Physics* 48 (27), 275003 (2015).
- [6] R. Tomasello, V. Puliafito, E. Martinez, A. Manchon, M. Ricci, M. Carpentieri, and G. Finocchio, Performance of synthetic antiferromagnetic racetrack memory: domain wall versus skyrmion, *Journal of Physics D: Applied Physics* 50 (32), 325302 (2017).
- [7] D. Kumar, T. Jin, S. Al Risi, R. Sbiaa, W. S. Lew, and S. Piramanayagam, Domain wall motion control for racetrack memory applications, *IEEE Transactions on Magnetics* 55 (3), 1-8 (2018).
- [8] A. Fernández-Pacheco, R. Streubel, O. Fruchart, R. Hertel, P. Fischer, and R. P. Cowburn, Three-dimensional nanomagnetism, *Nature communications* 8 (1), 1-14 (2017).
- [9] P. Němec, M. Fiebig, T. Kampfrath, and A. V. Kimel, Antiferromagnetic opto-spintronics, *Nature Physics* 14 (3), 229-241 (2018).
- [10] A. V. Kimel and M. Li, Writing magnetic memory with ultrashort light pulses, *Nature Reviews Materials* 4 (3), 189-200 (2019).
- [11] S.-H. Yang, Spintronics on chiral objects, Applied Physics Letters 116 (12) (2020).
- [12] S. A. Nikitov et al., Dielectric magnonics: from gigahertz to terahertz, *Physics-Uspekhi* 63 **(10)**, 945 (2020).
- [13] I. M. Miron et al., Fast current-induced domain-wall motion controlled by the Rashba effect, *Nature materials* 10 **(6)**, 419-423 (2011).
- [14] R. Badea and J. Berezovsky, Mapping the landscape of domain-wall pinning in ferromagnetic films using differential magneto-optical microscopy, *Physical Review Applied* 5 **(6)**, 064003 (2016).
- [15] J. Fritzsche, V. Moshchalkov, H. Eitel, D. Koelle, R. Kleiner, and R. Szymczak, Local Observation of Reverse-Domain Superconductivity in a Superconductor-Ferromagnet Hybrid, *Physical review letters* 96 (24), 247003 (2006).
- [16] M. Bode, E. Vedmedenko, K. Von Bergmann, A. Kubetzka, P. Ferriani, S. Heinze, and R. Wiesendanger, Atomic spin structure of antiferromagnetic domain walls, *Nature materials* 5 (6), 477-481 (2006).

- [17] A. Bisig et al., Correlation between spin structure oscillations and domain wall velocities, *Nature communications* 4 (1), 2328 (2013).
- [18] T. Yang, V. Gopalan, P. Swart, and U. Mohideen, Direct observation of pinning and bowing of a single ferroelectric domain wall, *Physical review letters* 82 (20), 4106 (1999).
- [19] J. Dillon and J. Remeika, Diffraction of light by domain structure in ferromagnetic CrBr3, Journal of Applied Physics 34 (3), 637-640 (1963).
- [20] M. Chetkin and Y. S. Didosyan, Stripe-structure and magneto-optical diffraction in orthoferrites, Fizika Tverdogo Tela 15 (4), 1247-1249 (1973).
- [21] J. Suits, Optical diffraction by magnetic domains in europium chalcogenides, *Journal of Applied Physics* 38 **(3)**, 1498-1499 (1967).
- [22] M. Gerasimov, S. Ilin, M. Logunov, S. Nikitov, A. Spirin, and A. Chaldyshkin, A magneto-optical setup for studying the time evolution of nanoscale domain-wall displacements under pulsed magnetization, *Instruments and Experimental Techniques* 60, 716-721 (2017).
- [23] C. Gutt et al., Single-pulse resonant magnetic scattering using a soft x-ray free-electron laser, *Physical Review B* 81 **(10)**, 100401 (2010).
- [24] A. V. Kimel, Ultrafast probes for ultrasmall magnets, *Physics* 3, 20 (2010).
- [25] B. Pfau et al., Ultrafast optical demagnetization manipulates nanoscale spin structure in domain walls, *Nature communications* 3 (1), 1100 (2012).
- [26] D. Weder et al., Transient magnetic gratings on the nanometer scale, Structural Dynamics 7 (5) (2020).
- [27] D. Zusin et al., Ultrafast perturbation of magnetic domains by optical pumping in a ferromagnetic multilayer, *Physical Review B* 106 **(14)**, 144422 (2022).
- [28] K. Prabhakara, T. Shapaeva, M. Davydova, K. Zvezdin, A. Zvezdin, C. Davies, A. Kirilyuk, T. Rasing, and A. Kimel, Domain Wall Deceleration in a Ferrite–Garnet Film by Femtosecond Laser Pulses, Moscow University Physics Bulletin 76 (6), 447-454 (2021).
- [29] M. Gerasimov, M. Logunov, A. Spirin, Y. N. Nozdrin, and I. Tokman, Time evolution of domain-wall motion induced by nanosecond laser pulses, *Physical Review B* 94 **(1)**, 014434 (2016).
- [30] P. Röschmann and P. Hansen, Molecular field coefficients and cation distribution of substituted yttrium iron garnets, *Journal of Applied Physics* 52 **(10)**, 6257-6269 (1981).
- [31] L. Helseth, R. Hansen, E. Il'yashenko, M. Baziljevich, and T. Johansen, Faraday rotation spectra of bismuth-substituted ferrite garnet films with in-plane magnetization, *Physical Review B* 64 (17), 174406 (2001).
- [32] R. Pearson, Magnetocrystalline Anisotropy of Rare-Earth Iron Garnets, *Journal of Applied Physics* 33 **(3)**, 1236-1242 (1962).
- [33] A. Andreenko, K. P. Belov, S. A. Nikitin, and A. M. Tishin, Magnetocaloric effects in rare-earth magnetic materials, *Soviet Physics Uspekhi* 32 **(8)**, 649 (1989).

- [34] M. Logunov, S. Nikitov, A. Stognii, S. Safonov, and A. Temiryazev, Evolution of the Hysteresis Loops of Iron Garnet Films upon Deep Layered Etching, Bulletin of the Russian Academy of Sciences: Physics 83, 866-868 (2019).
- [35] Y. B. Kudasov et al., Magnetooptic properties of bismuth-substituted ferrite-garnet films in strong pulsed magnetic fields, Physics of the Solid State 60, 2207-2210 (2018).
- [36] C. Mee, Recent measurements of the magneto-optical properties of some garnets, Contemporary Physics 8 (4), 385-400 (1967).
- [37] G. S. Kandaurova, New phenomena in the low-frequency dynamics of magnetic domain ensembles, Physics-Uspekhi 45 (10), 1051 (2002).
- [38] A. Kotsyubynsky, Crystalline, magnetic and domain structure of epitaxial ferritegarnet films, Physics and Chemistry of Solid State 18 (3), 275-281 (2017).
- [39] J. Dillon Jr, H. Kamimura, and J. Remeika, Magneto-Optical Studies of Chromium Tribromide, Journal of Applied Physics 34 (4), 1240-1245 (1963).
- [40] O. Kfir et al., Nanoscale magnetic imaging using circularly polarized high-harmonic radiation, Science advances 3 (12), eaao4641 (2017).
- [41] N. Bergeard et al., Irreversible transformation of ferromagnetic ordered stripe domains in single-shot infrared-pump/resonant-x-ray-scattering-probe experiments, Physical Review B 91 **(5)**, 054416 (2015).
- [42] F. Büttner et al., Observation of fluctuation-mediated picosecond nucleation of a topological phase, Nature materials 20 (1), 30-37 (2021).
- [43] C. Graves et al., Nanoscale spin reversal by non-local angular momentum transfer following ultrafast laser excitation in ferrimagnetic GdFeCo, Nature materials 12 (4), 293-298 (2013).
- [44] A. Logginov and G. Nepokoĭchitskiĭ, Ultrafast magnetic-moment-flip waves in iron garnet films, Soviet Journal of Experimental and Theoretical Physics Letters 35, 27 (1982).
- [45] F. Hansteen, A. Kimel, A. Kirilyuk, and T. Rasing, Nonthermal ultrafast optical control of the magnetization in garnet films, Physical Review B 73 (1), 014421 (2006).
- [46] B. Koopmans, M. Van Kampen, J. Kohlhepp, and W. De Jonge, Ultrafast magneto-optics in nickel: magnetism or optics?, Physical review letters 85 (4), 844 (2000).
- [47] G. Zhang, W. Hübner, G. Lefkidis, Y. Bai, and T. F. George, Paradigm of the time-resolved magneto-optical Kerr effect for femtosecond magnetism, Nature Physics 5 (7), 499-502 (2009).
- [48] K. Carva, M. Battiato, and P. M. Oppeneer, Is the controversy over femtosecond magneto-optics really solved?, Nature Physics 7 (9), 665-665 (2011).
- [49] J.-Y. Bigot, L. Guidoni, E. Beaurepaire, and P. N. Saeta, Femtosecond spectrotemporal magnetooptics, Physical review letters 93 (7), 077401 (2004).

- [50] T. Gerrits, H. Van Den Berg, J. Hohlfeld, L. Bär, and T. Rasing, Ultrafast precessional magnetization reversal by picosecond magnetic field pulse shaping, *Nature* 418 **(6897)**, 509-512 (2002).
- [51] R. B. Wilson, Y. Yang, J. Gorchon, C.-H. Lambert, S. Salahuddin, and J. Bokor, Electric current induced ultrafast demagnetization, *Physical Review B* 96 **(4)**, 045105 (2017).
- [52] A. Melnikov, I. Razdolski, T. O. Wehling, E. T. Papaioannou, V. Roddatis, P. Fumagalli, O. Aktsipetrov, A. I. Lichtenstein, and U. Bovensiepen, Ultrafast transport of laser-excited spin-polarized carriers in Au/Fe/MgO (001), *Physical review letters* 107 (7), 076601 (2011).

# CHAPTER 4

# Ultrafast heat-assisted magnetization dynamics in ferrimagnetic insulator<sup>2</sup>

Ultrafast laser-induced heating of ferrimagnetic iron garnet in an external magnetic field triggers magnetization precessional dynamics with a large amplitude. The dynamics is studied as a function of magnetic field, laser fluence, and sample temperature. Exploring the three-dimensional space of these parameters experimentally and computationally, we identify the conditions for which the amplitude of the precession is the largest and even achieve values sufficient for magnetic recording. We found that the range of external magnetic fields and temperatures, which corresponds to the magnetic recording, is rather narrow. Modelling the dynamics, using magnetization as a macroscopic parameter, reveals that this range of parameters is defined by the optimal height of the potential barrier separating two stable states. The barrier needs to be low enough to allow the switching, but not so low that the stability of the states is lost.

Adapted from: A. Dolgikh, D. Afanasiev, V.V. Yurlov, M.V. Logunov, A.K. Zvezdin and A.V. Kimel, "Ultrafast heat-assisted magnetization dynamics in a ferrimagnetic insulator", Phys. Rev. B 107(9), 094424, 2023

#### 4.1 Motivation

Ultrafast magnetism is a rapidly developing research field that explores spin dynamics in ferro-, ferri- and antiferromagnetic media excited by sub-100 ps stimuli [1-6]. If such stimuli excite magnets on a timescale faster than the characteristic times of elementary spin-lattice or electron-lattice interactions, they bring the media into a strongly non-equilibrium state, where the conventional description of magnetic phenomena in terms of equilibrium thermodynamics is no longer valid, conventional approximations fail and the triggered magnetization dynamics can become counter-intuitive [4]. Apart from purely fundamental interest, ultrafast magnetism challenges the fundamental and practical limits on the speed and energy dissipations of writing of a single magnetic bit [7-10]. Hence the field has a potential to impact future data storage technologies.

Among all magnetic materials studied in ultrafast magnetism, ferrimagnets represent a rich and probably the most appealing playground to explore large amplitude magnetization dynamics and magnetic writing induced by ultrashort stimuli. For instance, in contradiction with Curie's symmetry principle, it was discovered that solely ultrafast heating either with the help of femto- and picosecond laser pulses [11-15] or picosecond electrical pulses [16] is able to reverse the magnetization of ferrimagnetic metals. Although it has been believed that heat-assisted magnetization dynamics and recording in insulators are slow [3], ferrimagnetic iron garnets facilitate an unconventional, precessional route of heatassisted magnetic recording [17]. In this mechanism, laser-induced heating destroys magnetic anisotropy, launches anomalously damped magnetization precession in an external magnetic field, and eventually results in capturing of the magnetization by another stable bit-state [17]. In ferrimagnets, where both the net magnetization and magnetic anisotropy are strongly temperature dependent, the efficiency of the heat-assisted precessional magnetic recording must be a function not only of magnetic field but also of temperature. The goal of this work is to reveal the mutual interplay of temperature and magnetic field which eventually leads to laserinduced switching.

In this work, we study large amplitude heat-assisted magnetization dynamics in ferrimagnetic iron garnet by performing time-resolved single-shot imaging of magnetization dynamics as a function of external magnetic field, laser fluence, and sample temperature. Exploring the three-dimensional space of these parameters experimentally and computationally, we identify and explain the conditions for which the amplitude of the precession is the largest and even achieves values sufficient for magnetic recording.

## 4.2 Sample

The sample studied in this chapter is the same as in the previous one - lutetium iron garnet. We will not reiterate all the properties of this sample that have already been described in Chapter 3. We will only highlight the most important properties relevant to the study of heat-assisted magnetization switching. In this compound the spins of Fe<sup>3+</sup> ions in the octahedral and the tetrahedral sites form two nonequivalent magnetic sublattices with oppositely oriented magnetizations  $\mathbf{M}_1$  and  $\mathbf{M}_2$ , respectively. The difference in the volume fraction of the octahedral and the tetrahedral sites leads to a nonzero net magnetization  $\mathbf{M} = \mathbf{M}_1 + \mathbf{M}_2$  below the Curie temperature  $T_{\rm C} \approx 600$  K [18]. In the parent compound Lu<sub>3</sub>Fe<sub>5</sub>O<sub>12</sub>, the net magnetization is dominated by the tetrahedral sublattice. Substituting Fe<sup>3+</sup> ions in the tetrahedral positions with Ga<sup>3+</sup> and Al<sup>3+</sup> levels off the magnetizations of the sublattices, such that at the magnetization compensation point  $T_M=\,$  50 K the magnetizations of the sublattices cancel each other, such that  $\mathbf{M}_{1}\left(T_{\mathrm{M}}
ight)=$  $-\mathbf{M}_{2}\left(T_{\mathrm{M}}\right)$  and the net magnetization vanishes  $\mathbf{M}=0$ . We note that neither Lu<sup>3+</sup> nor Bi<sup>3+</sup> have a magnetic moment and thus have no impact on the net magnetization M. However, the magneto-optical Faraday effect depends not only on the magnetization but also on the Verdet constant. Adding Bi<sup>3+</sup> ions increases the Verdet constant [19-22], but is known to change  $T_{\rm C}$  as a side effect [23].

The epitaxial film of iron garnet with a thickness of 8 µm was grown on a (111) Gd<sub>3</sub>Ga<sub>5</sub>O<sub>12</sub> substrate using liquid-phase epitaxy. Although crystals of iron garnet have a cubic magnetic anisotropy, thin films normally acquire a uniaxial anisotropy during growth, with the easy axis along the sample normal. At room temperature, the magnetization can be saturated by applying a magnetic field of about  $H_{
m s}$  = 50 Oe along the easy axis [24]. The film of iron garnet is characterized by a strong magneto-optical Faraday effect reaching 6° for light at a wavelength of 800 nm ( $h\nu$ = 1.55 eV). The magneto-optical effect at this wavelength is dominated by the magnetization of the Fe<sup>3+</sup> ions of the octahedral sublattice [22].

## 4.3 Experimental details

To study laser-induced magnetization dynamics in the iron garnet, we employed single-shot magneto-optical imaging. In order to trigger magnetization dynamics, we employed a femtosecond laser pulse having a 100 fs duration at the central wavelength of 625 nm ( $h\nu$  = 1.98 eV). We experimentally estimated the absorption coefficient at this wavelength to be around 300 cm<sup>-1</sup>. Hence the light penetration depth (40 µm) is still substantially larger than the sample thickness. This condition ensures a nearly homogeneous pump-induced heating across the whole sample thickness.

The linearly polarized pump beam was at the angle of incidence of 20° and was focused into a spot with the width at half maximum equal to 100  $\mu m$ . Magneto-optical images of the sample were obtained using linearly polarized probe pulses with a duration of about 100 fs at the central wavelength of 800 nm. The unfocused probe beam at normal incidence was used to visualize spatial dynamics induced by the pump pulse. Due to the magneto-optical Faraday effect, the component of the magnetization normal to the sample plane  $M_{\rm z}$  resulted in a polarization rotation of the probe pulses  $\theta \sim M_{\rm z}$ . Using an optical analyzer, we transformed the polarization rotation into intensity changes, which were subsequently detected by a CCD camera (Fig. 1(a)). This experimental scheme enables visualization of the spatial distribution of the sample magnetization and is characterised by a particular sensitivity to the out-of-plane magnetization component. With varying time delay between the pump and probe pulses, one can obtain time-resolved magneto-optical snapshots of the pump-induced magnetization dynamics with a temporal resolution down to 100 fs.

The measurements were performed for a wide range of magnetic fields  $H^{\rm ext}$ , such that  $0 < H^{\rm ext} < 3.5$  kOe. The field was applied in the sample plane, leading to a tilt of the magnetization from the sample normal (Fig. 4.1(b)). For the field applied exactly in the sample plane, the magnetization has two equivalent energy minima of thermodynamic potential corresponding to magnetizations oriented at angles + $\varphi$  and –  $\varphi$  with respect to the sample plane, see Fig. 4.1(b). Here  $\varphi$  = 0 corresponds to the peak of the potential barrier separating the minima. It means that if the magnetization has deviated from one minimum over an angle larger than  $\varphi$ , there is a chance that upon relaxation the magnetization will relax to another minimum. In this case, the whole procedure will resemble the recording of a single magnetic bit as explained in Ref. [17]. A slight tilt of the magnetic field out of the sample plane breaks the equivalence between the potential minima, such that at  $H_{\rm z}^{\rm ext} > H_{\rm s}$  one of the minima eventually

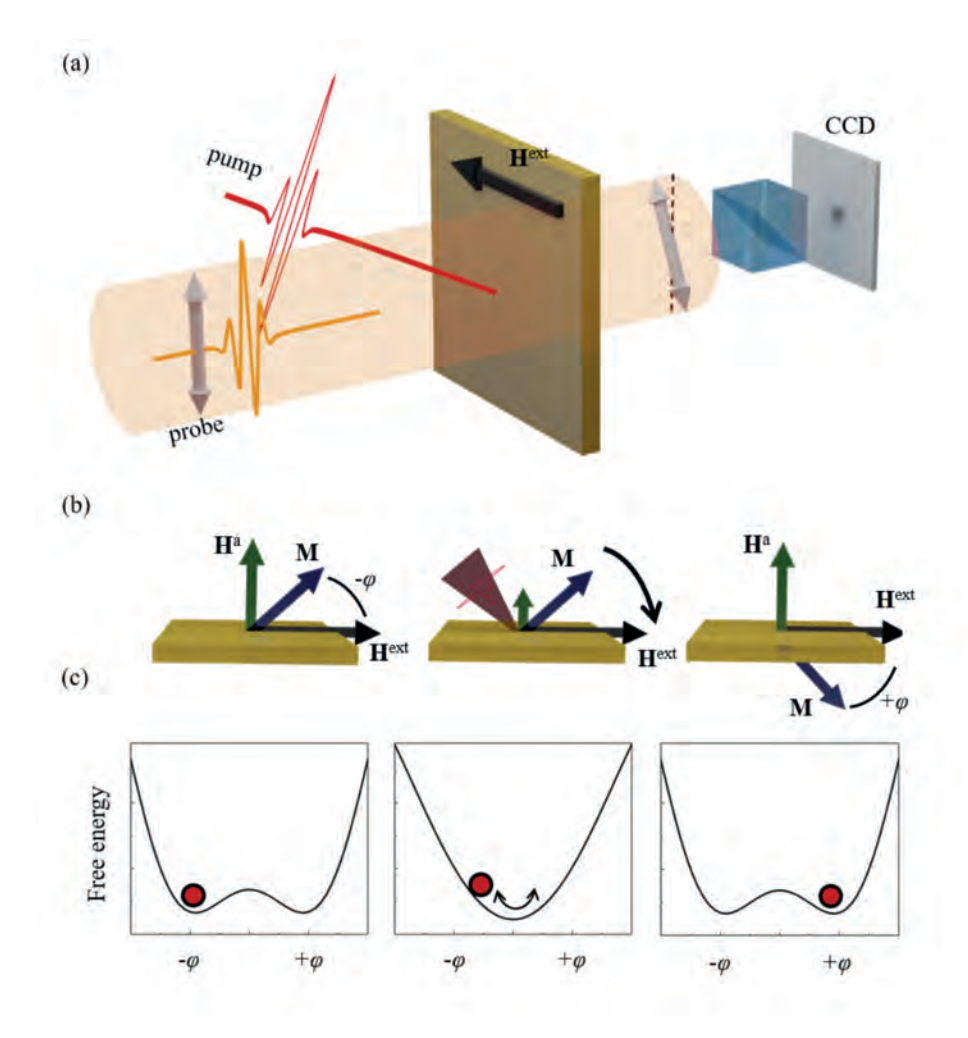
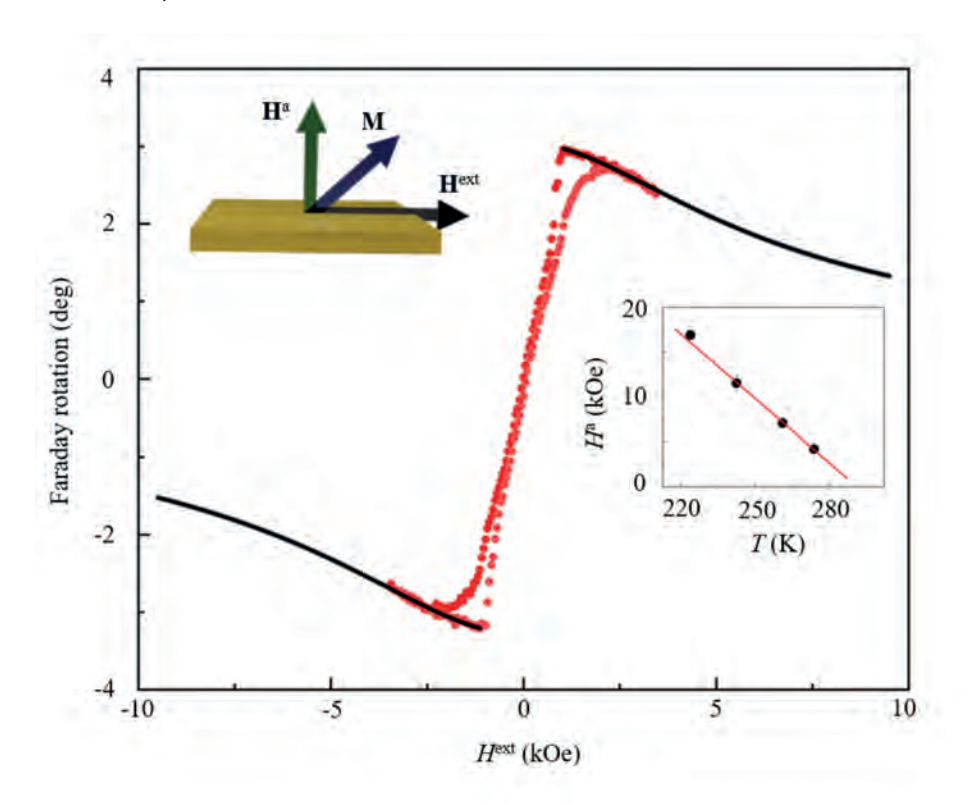


Fig. 4.1. (a) A schematics of the experiment: unfocused probe illuminates the sample; rotation of the probe polarization plane heta is detected by the CCD camera. (b) Evolution of the sample magnetic state. From left to right: unperturbed state; pump pulse heats the sample, reduces the field of magnetic anisotropy  $\mathbf{H}^{\mathrm{a}}$  and thus launches magnetization precession; after relaxation,  $\mathbf{H}^{\mathrm{a}}$  is restored, and the magnetization  ${\bf M}$  is fixed in the switched direction. (c) The free energy profile corresponds to the cartoons on panel (b).

disappears and the magnetization saturates. In this work, we intentionally tilted the external magnetic field over an angle of about 0.5° from the sample plane. The tilted field did not destroy the second minimum but ensured that if the magnetization is switched under an action of a single pump pulse, it relaxes back to the initial state before the next pump pulse arrives.

Figure 4.2 shows the magneto-optic Faraday effect  $\theta$  as a function of the applied magnetic field in the geometry of the experiment. Due to the small out-of-plane z - component of the magnetic field, the magnetization is saturated along the easy axis. Hence, the maximum



**Fig. 4.2.** The probe polarization rotation vs the external magnetic field at T = 275 K. Experimental data is represented by red circles, black lines extrapolate the dependence to high magnetic fields. For the extrapolation, we fit the experimented data points for  $H^{\rm ext}>H_{\rm s}$  with function  $\alpha_F=A\cdot\cos\varphi$ , where A is a fit parameter and  $\varphi=\arctan\frac{H^a}{H^{\rm ext}}$  is obtained as explained in the text. The inset shows the estimated  ${\bf H}^a$  as a function of temperature as explained in the text.

value of the Faraday effect  $\theta^0$  (Fig. 4.2) corresponds to the case when the magnetization is aligned along the normal to the sample. A stronger external field pulls the magnetization towards the sample plane, which is seen as a negative slope for the fields  $H^{\rm ext}>1$  kOe when  $H^{\rm ext}_{\rm z}>H_{\rm s}$ . Using the slope, we estimated the effective field of magnetic anisotropy  $H^{\rm a}$ . Assuming that the equilibrium orientation of the magnetization is defined by an interplay between the mutually perpendicular external magnetic field and the effective field of magnetic anisotropy, the slope from Fig. 4.2 was fitted using:

$$heta = heta^0 \cdot \cos \left( \arctan \left( rac{H^{
m ext}}{H^{
m a}} 
ight) 
ight)$$
 (4.1)

where  $heta^0$  is the Faraday rotation of the saturated sample i.e., the maximum rotation. The anisotropy field  $\mathbf{H}^{\mathrm{a}}$  was estimated from the measured hysteresis loops as a function of temperature and the results are summarized in the inset of Fig. 4.2. Applying a linear fit to the

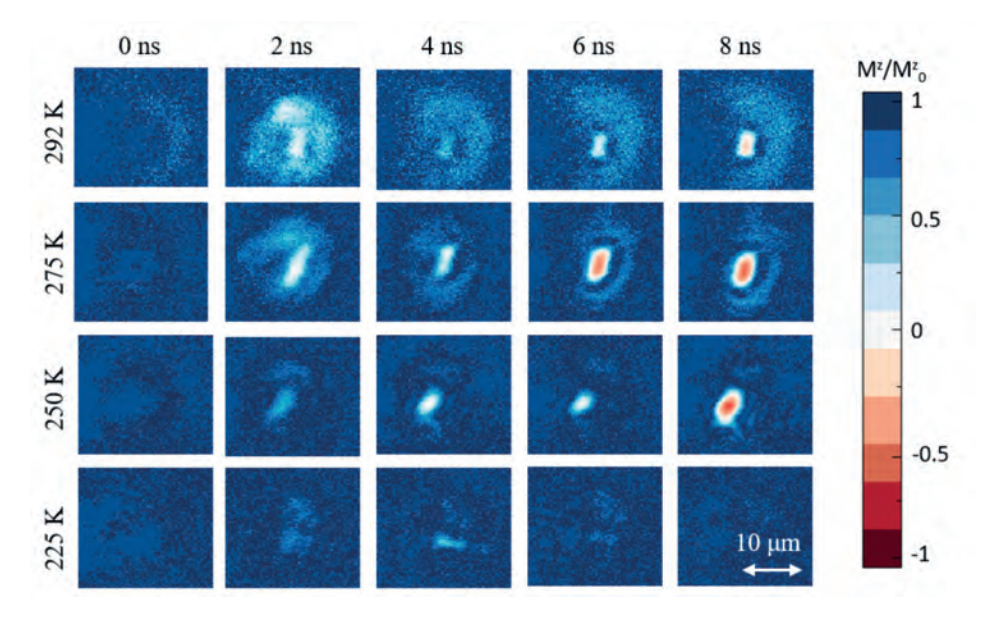


Fig. 4.3 . Temporally- and spatially-resolved laser-induced magnetization dynamics. The pump fluence is 80 mJ/cm $^2$ . Magnetic field  $H^{
m ext}=3$  kOe is applied in the sample plane. The color code represents the orientation of the magnetization, such that magnetization pointing "up" corresponds to blue (1), while magnetization pointing "down" corresponds to red (-1).

data and extrapolating the fitted function to higher temperatures suggests that the anisotropy field can even reach zero far below  $T_{\rm C}$ . Such behaviour appears to be typical for this type of ferrimagnetic iron garnet [23].

# 4.4 Experimental results

Figure 4.3 shows time-resolved magneto-optical images of the magnetization dynamics excited by an intense femtosecond pump with a fluence of 80 mJ/cm<sup>2</sup>. The measurements were performed in a magnetic field  $H^{
m ext}=3$  kOe at several temperatures above  $T_{
m M}.$  It is seen that during the first few nanoseconds (ns), the laser-induced dynamics evolves in a large area. Starting from 4 ns, one observes an onset of an intense signal in an area roughly 7  $\mu$ m in diameter just in the centre of the spot. This area is surrounded by a ring with a weaker signal resembling a bull eye pattern much similar to those reported in [7,17,25]. To process the magneto-optical data, we calculated the z – component of the magnetization after the pump excitation  $M^z$  normalized on  $M_0^z$ . The changes of  $M^z/M_0^z$  by more than 100% imply that the amplitude of the magnetization dynamics is sufficiently large to overcome the potential barrier separating two energy minima, see Fig. 4.1(c).

Digitizing the images allows us to acquire quantitative data on the magnetization dynamics. We selected a vertical line running through the spot center to showcase the strobe-like variation of the switching area depending on the time delay between the probe and the pump (Fig. 4.4). The initial magnetization state in the sample corresponds  $M^{\rm z}/M_0^{\rm z}=1$  or the gray color of the palette.

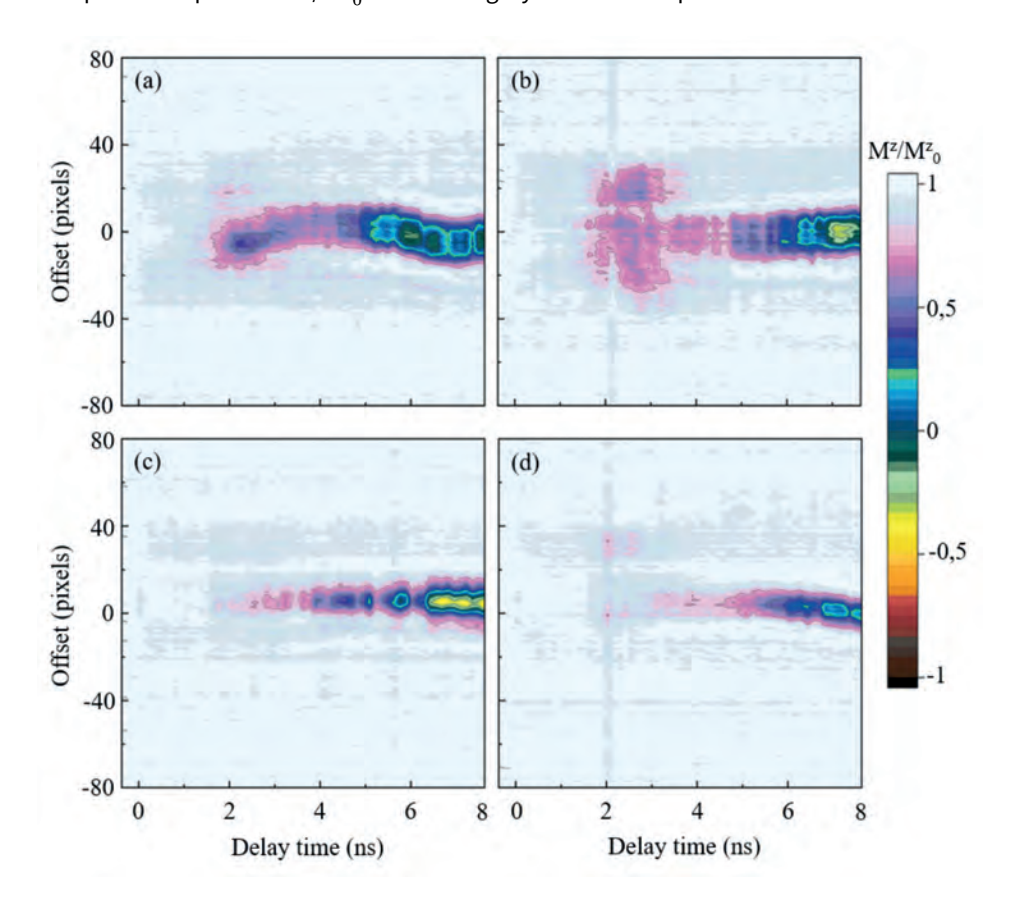


**Fig. 4.4**. Traces of pump-induced magnetization dynamics for varied pump fluences and temperatures: (a) 275 K, 80 mJ/cm², (b) 275 K, 100 mJ/cm², (c) 250 K, 80 mJ/cm², (d) 250 K, 100 mJ/cm², Magnetic field  $H^{\rm ext}=3$  kOe. The dynamics were derived from stroboscopic images like those in Fig. 3 along a vertical line passing through the spot center.

The figures illustrate that dynamics with an amplitude that we can detect using the CCD commence not at the moment of the pump pulse arrival but with a delay about  $\Delta t = 2$  ns. Notably, at lower temperatures, this delay is more pronounced. Also, the size of the switchable spot grows with increasing temperature, while the fluence influence on the final spot size is less noticeable. With higher fluence, the change in magnetization in the 2 ns <  $\Delta t$  < 3 ns interval takes place not only in the central area but also at the spot edges, eventually forming an additional ring, also described in [17].

By integrating the signal in the central area of 5 pixels and in the spot's counterside area, also of 5 pixels, we plotted the relative magnetization as a function of time (see Fig. 4.5). We followed the routine described in [26] to account for the nonlinear relationship between the camera-detected intensity and the Faraday rotation, which provides information about  $M_z$ . The central area dynamics reveals such a fingerprint of precessional magnetic switching as

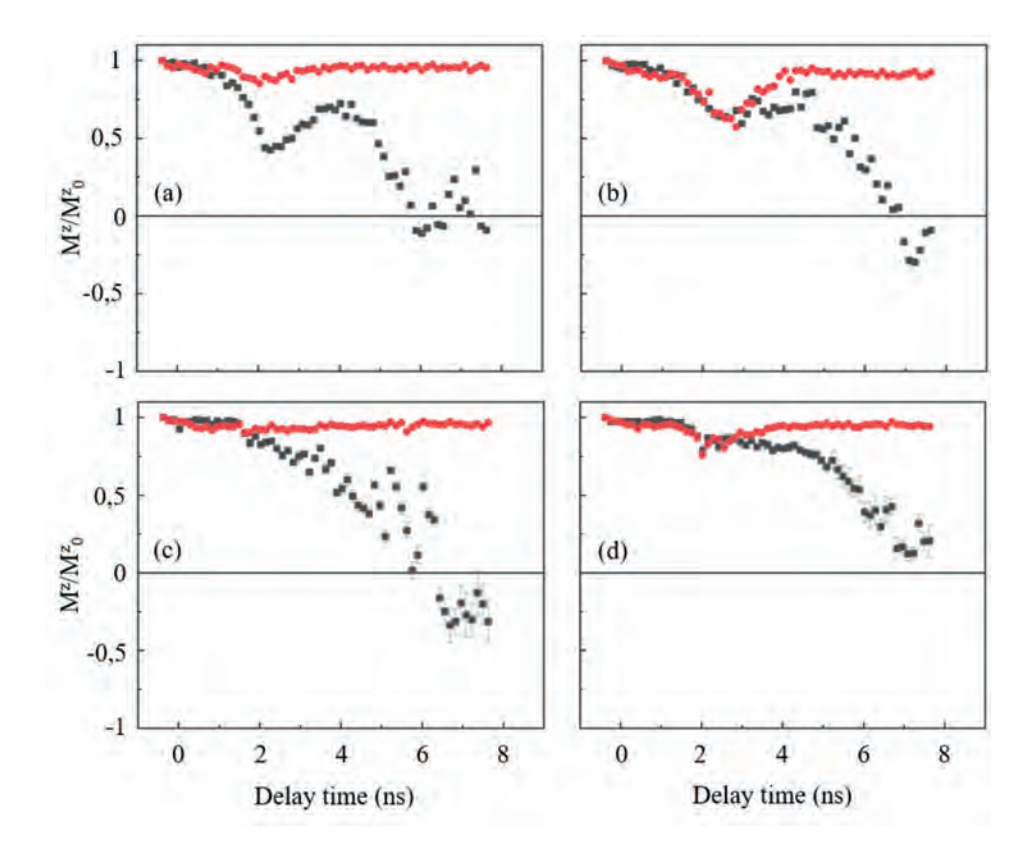


**Fig. 4.5**. Pump-induced magnetization dynamics for central part (black squares) and side part (red circulars) of the beam spot. Magnetic field  $H^{\rm ext}=3$  kOe, temperature and fluence correspond to (a) 275 K, 80 mJ/cm², (b) 275 K, 100 mJ/cm², (c) 250 K, 80 mJ/cm², (d) 250 K, 100 mJ/cm². The values were obtained by integrating the areas of five pixels from the corresponding traces from Fig. 4.4.

oscillations of the magnetization with large amplitude. The signal at the spot's center corresponds to the magnetization rotation over a large angle, which can even exceed  $\varphi$  (see Fig. 4.1(b)). According to [17], such a large amplitude of the magnetization precession can be sufficient for switching. It is worth noting that an increase in fluence does not always have a positive impact on precession amplitude (Fig. 4.5(c) and (d)). At low temperatures, the precession amplitude, on the contrary, fell and did not exceed the angle between the magnetization and the sample plane,  $\varphi$ .

It is observed that, with high fluence values, more energy is transferred to the spot edges, and during the first 3-4 ns, the dynamics at the spot edges mirror the central dynamics. Later, the edge precession decays more quickly, forming a ring with magnetization lying in the same semiplane as the initial magnetization but differs

in  $M_{\rm z}$  magnitude. With low fluence, the edge dynamics decay much more rapidly, and the discrepancy with the central area starts as early as  $\Delta t$  = 2 ns.

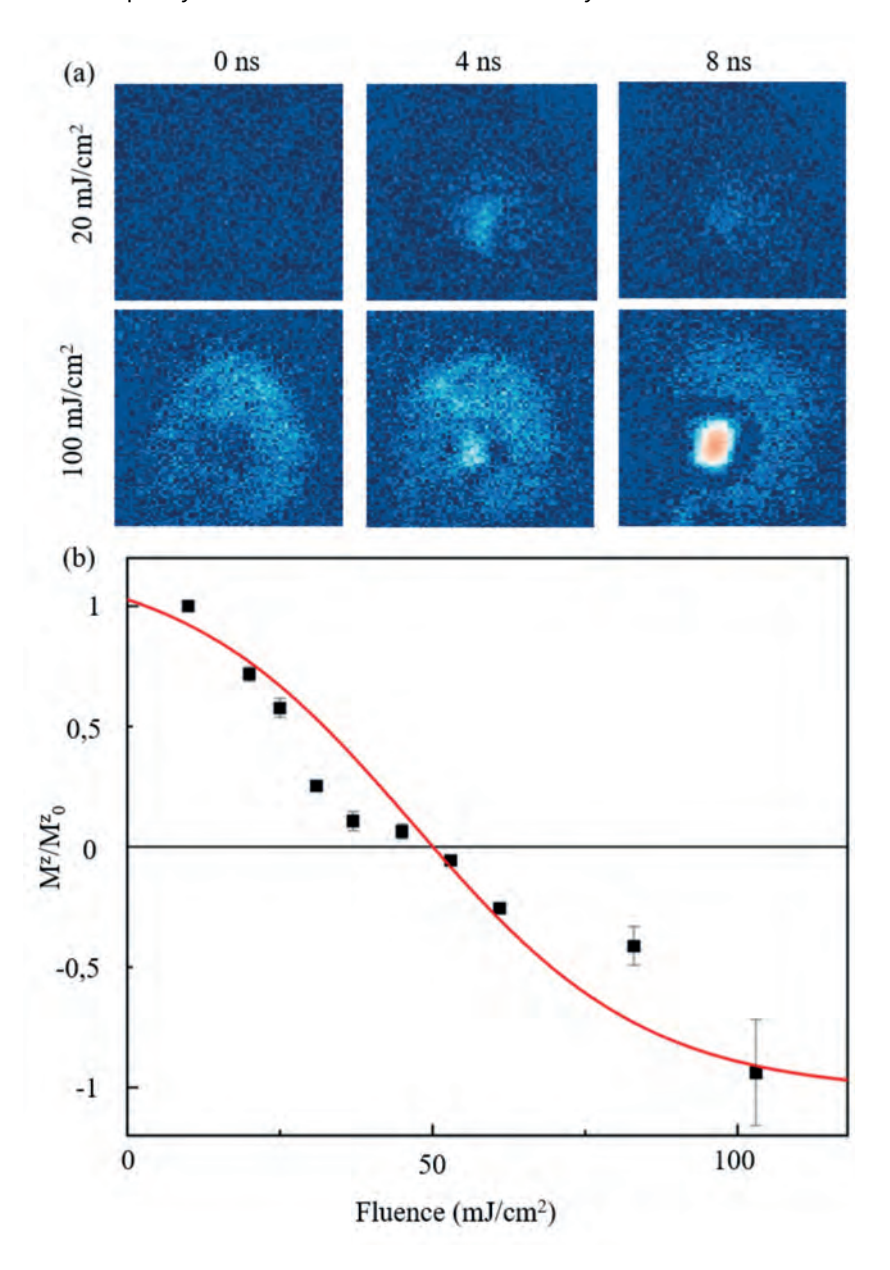


**Fig. 4.6.** (a) Temporarily- and spatially resolved magnetization dynamics for low  $F=20\,$  mJ/cm2 (upper panel) and high  $F=100\,$  mJ/cm2 pump fluence (lower panel), respectively. (b) Out-of-plane component of the magnetization at 8 ns after pump pulse.  $M^z/M_0^z=1$  corresponds to the magnetization in the initial state (up).  $M^z/M_0^z=-1$  corresponds to the reversed state (down). The red line is a guide to the eye shown to highlight the nonlinear character of the dependence.

The time-dependent magnetization was measured for fluences in the range of  $20 {\rm mJ/cm^2} \le F \le 100 {\rm mJ/cm^2}$  (Fig. 4.6). In the shown measurements, the initial sample temperature was T=292 K, the external magnetic field  $H^{\rm ext}=3$  kOe. At a low fluence of F=20 mJ/cm², changes in magnetization occur over an average time interval, which can be seen in the images (fig. 4.6(a)). This dynamics subsequently fades, and the magnetization returns to its original state. At a high fluence value of F=100 mJ/cm², the dynamics occur over a larger area of the sample and also begin at  $\Delta t << 1$  ns. Subsequently, this dynamics leads to the formation of a domain with an opposite magnetization value compared to the original one. Fig. 4.6(b) summarizes the amplitudes of the precessional dynamics as a function of fluence at the time point  $\Delta t=8$  ns. The red line serves to highlight the nonlinearity in the dependence.

Next, to summarize the conditions necessary for the switching, we built up a phase diagram showing snapshots of the photo-induced magnetic changes at long time delays after the pumping. Figure 4.7(b) summarizes the snapshots obtained at the pump-probe delay  $\Delta t=8$  ns for various temperatures and external magnetic fields. Note that while for some combinations of  $H^{\rm ext}$  and T the changes of  $M^z/M_0^z$  exceed 100% ( $M^z/M_0^z < 0$ ), there are also regions, where the magnetization was impacted only slightly. Moreover, it is seen that the largest changes in the magnetization are achieved along one diagonal of the square formed by the horizontal (T) and the vertical ( $H^{\rm ext}$ ) axes.

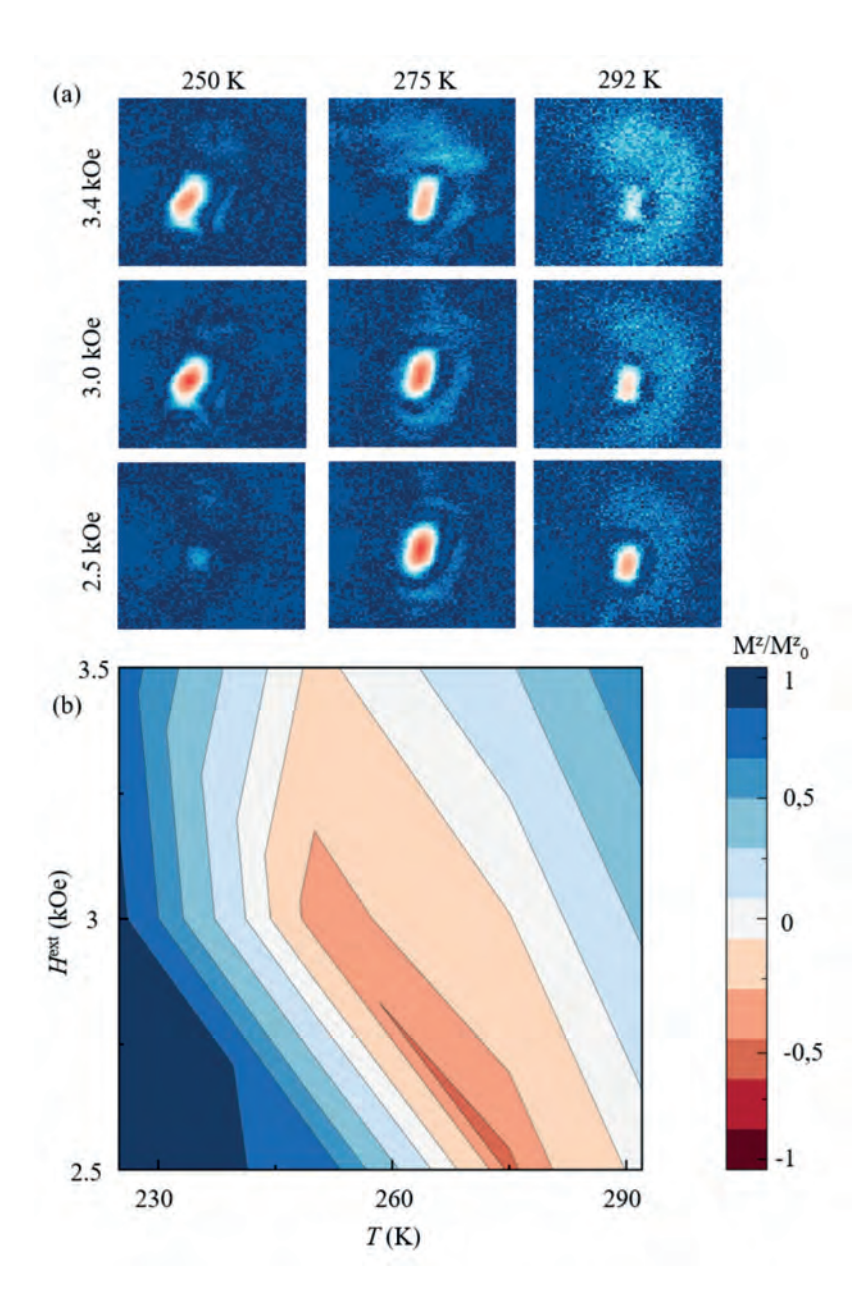


**Fig. 4.7**. (a) The magneto-optical images obtained 8 ns after the pump for various temperatures (horizontal) and magnetic fields (vertical). The pump fluence is 80 mJ/cm<sup>2</sup>. (b) Phase diagram of the pump-induced magnetization state as obtained after digitizing the images shown in panel (a).

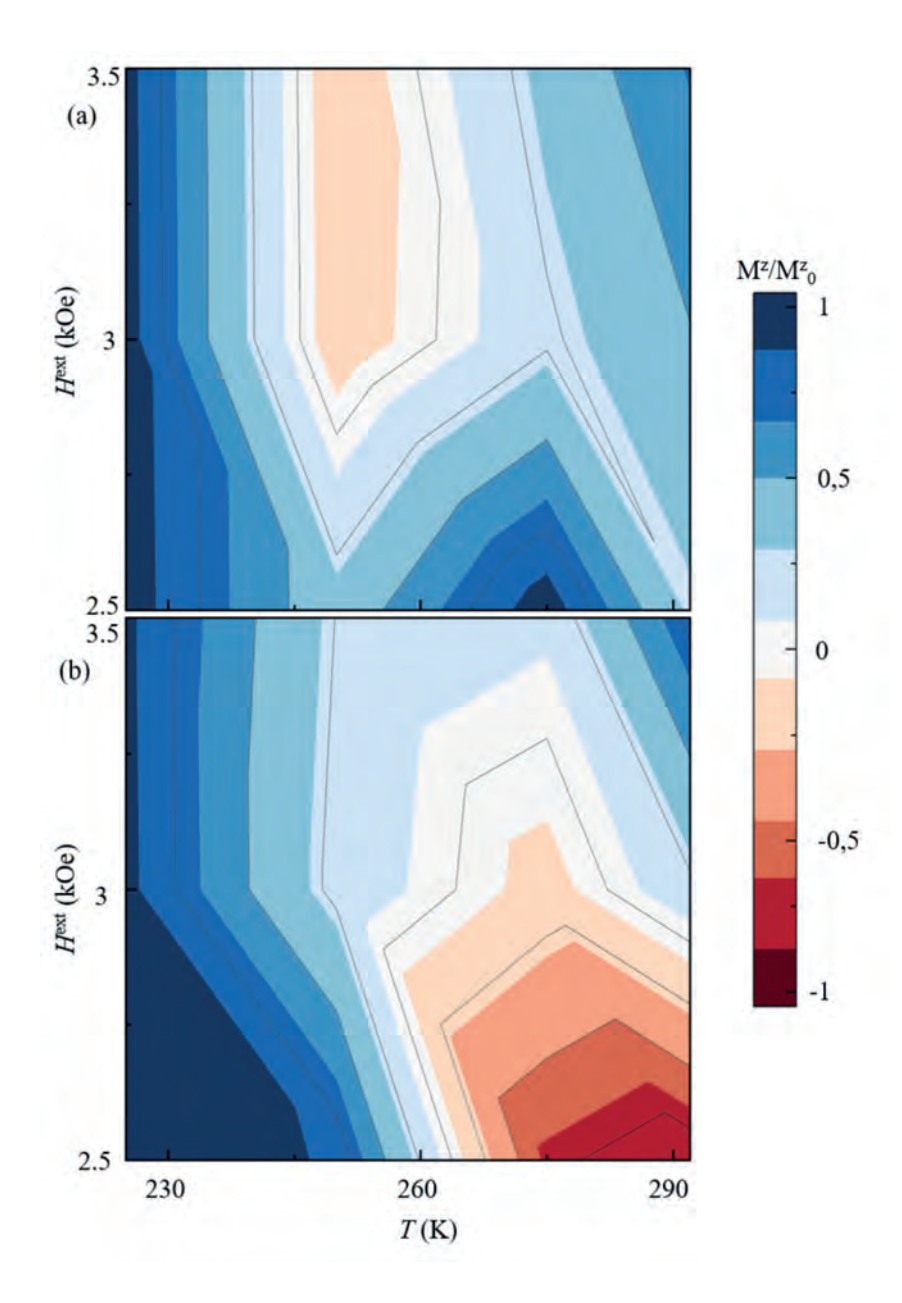


Fig. 4.8 . HT- phase diagram of the pump-induced magnetization state for different fluences: (a)  $60 \text{ mJ/cm}^2$ , (b)  $100 \text{ mJ/cm}^2$ .

At other fluence values, the diagonal character of the maximum magnetization amplitude at the HT-phase diagram is preserved (Fig. 4.8). However, the absolute maximum itself shifts to the area of higher temperatures and smaller fields at

higher fluence and to the area of lower temperatures and larger fields at lower fluence.

#### 4.5 Discussion

Our results show that large amplitude magnetization dynamics and switching in the studied iron garnet are strongly dependent on temperature and magnetic field. Although the geometry of the experiment and the mechanism of the switching are similar to those described in [17], in this work we reveal that the magnetization dynamics depends not only on the external magnetic field and laser fluence but also on temperature. To understand the origin of this dependence, we carried out a set of numerical simulations.

In the mechanism described in [17], ultrafast laser-induced heating destroys the magnetic anisotropy thus changing the equilibrium orientation of the magnetization. To reach the new equilibrium, the magnetization starts a largeamplitude precession around the external magnetic field. Due to damping, the magnetization can be caught by the second stable state. We estimated the temperature increase produced by the laser pulse using the heat balance equation:

$$\Delta T = \frac{\alpha \mathbf{F} \cdot S}{\mathbf{cm}} \tag{4.2}$$

where S and m are the surface area and the mass of the irradiated sample, c is the specific heat and lpha is the absorption coefficient. The specific heat c and the mass density of the garnet were taken from Refs. [27-31].  $\alpha$  was estimated experimentally with the help of the Beer-Lambert law. Considering a Gaussian profile of the pump intensity, the pump fluence of 80 mJ/cm2 must be enough to increase the sample temperature for about 20 K. According to the data shown in the inset of Fig. 4.2, such heating is indeed large enough to weaken and nearly destroy the magnetic anisotropy in the sample.

We assume that the dynamics could be described using magnetization as the only macroscopic order parameter. While such an approximation overlooks the multisublattice nature of the iron garnet, it can be used far from the compensation temperature  $T_{\rm M}$  [32]. The dynamics is further described using the Lagrange formalism and the Rayleigh dissipation function [33-35]:

$$\mathcal{L} = M(1 - \cos\theta) \frac{\dot{\varphi}}{\gamma} - U(\theta, \varphi) \,,$$
 
$$U(\theta, \varphi) = -\frac{1}{2} M H^{\mathrm{A}}(T) \sin^2 \theta \sin^2 \varphi - M H_{\parallel}^{\mathrm{ext}} \cos \theta - M H_{\perp}^{\mathrm{ext}} \sin \theta \sin \varphi, \qquad (4.3)$$
 
$$R = \frac{a_{\mathrm{d}} \left( \dot{\theta} + \sin^2 \theta \dot{\varphi}^2 \right)}{\gamma} \,,$$

where  $U(\theta,\varphi)$  is potential energy, M is the total magnetization of the magnetic film,  $\gamma$  is the gyromagnetic ratio,  $\phi$  and  $\theta$  are azimuthal and polar angles of the magnetization vector respectively,  $a_{
m d}$  is the Gilbert damping parameter,  $H_{\parallel}^{
m ext}$  and  $H_\perp^{
m ext}$  are in-plane and out-of-plane components of the applied magnetic field, respectively. The first term in the potential energy represents the anisotropy energy, the second and the third - the Zeeman energy. From the potential energy one finds two ground states of the system corresponding to the angles:

and  $arphi^{(2)}=rac{3\pi}{2}, heta^{(2)}pprox rccos\left(rac{H^{
m ext}}{H^{
m a}(T)}
ight)$ ,  $arphi^{(1)} = rac{\pi}{2}, heta^{(1)} pprox rccos\left(rac{H^{
m ext}}{H^{
m a}(T)}
ight)$ respectively. Using Eq. (4.1), the Euler-Lagrange equations can be written as follows:

$$\begin{cases} \dot{\theta} + \alpha \sin\theta \dot{\varphi} = \frac{\omega_{\rm a}(T) \sin\theta \sin^2\varphi}{2} + \omega_{\rm H}^{\perp} \cos\varphi \\ \sin\theta \dot{\varphi} - \alpha \dot{\theta} = -\frac{\omega_{\rm a}(T) \sin^2\varphi \sin^2\theta}{2} + \omega_{\rm H}^{\parallel} \sin\theta - \omega_{\rm H}^{\perp} \cos\theta \sin\varphi \end{cases}$$
(4.4)

where  $\omega_{\mathrm{a}}\left(T\right)=\gamma H^{\mathrm{a}}\left(T\right), \omega_{\mathrm{H}}^{\parallel}=\gamma H_{\parallel}^{\mathrm{ext}}, \omega_{\mathrm{H}}^{\perp}=\gamma H_{\perp}^{\mathrm{ext}}$  . The temperature of the magnetic film changes in time T = T(t) due to laser pulse heating. To model the time dependence, we solve the power balance equation:

$$\chi F = C_{\rm V} V \frac{\mathrm{dT}}{\mathrm{dt}} + c \left( T - T_0 \right), \tag{4.5}$$

where F is the laser fluence,  $C_{\rm V}$  is the isochoric specific heat, V is the volume of the heated area,  $T_0$  is the bias temperature of the substrate,  $\chi$  and c are material parameters whose ratio can be defined by fitting experimental data assuming that  $\Delta T pprox \lambda F$  where  $\lambda = 0.25 {
m K}\cdot {
m cm}^2/{
m mJ}$  was calculated from equation (2),  $\Delta T =$  $T\left( au
ight) -T_{0},\, au$  is the pulse duration. This model implicitly assumes instantaneous heat transfer from light to the lattice. Indeed, it is known in optically excited magnetic dielectrics, such as iron garnets [3,36,37], the energy from optically excited electrons to the lattice is transferred at the subpicosecond timescale. Afterwards, the equilibrium lattice temperature is established at the time-scale of thermalization of phonons, which is given by the characteristic time of phononphonon interaction (~100 ps). As this timescale is much shorter than the characteristic timescales of the spin precession presented in this work, the assumption of instantaneous heating holds true for the modelling of magnetization dynamics.

We performed the modelling by taking the states with  $\varphi = \varphi^{(1)} = \frac{\pi}{2}, \theta = \vartheta^{(1)}$  as the initial state. The second metastable state is thus  $\varphi=\varphi^{(2)}=\frac{3\pi}{2}, \theta=\vartheta^{(2)}$ . In the modeling, we also set that  $\alpha_{
m d}$  = 0.05,  $\frac{H_{\perp}}{H_{\parallel}}$  = 0.01, V = 6.3  $\cdot$  10<sup>4</sup>  $\mu$ m $^2$ ,

 $C_{\rm V}$  = 4.1 J/Kcm<sup>3</sup>, F = 80 mJ/cm<sup>2</sup>. The temperature dependence of the anisotropy field  $H^{a}(T)$  is taken from the experiment (see Fig. 4.2).

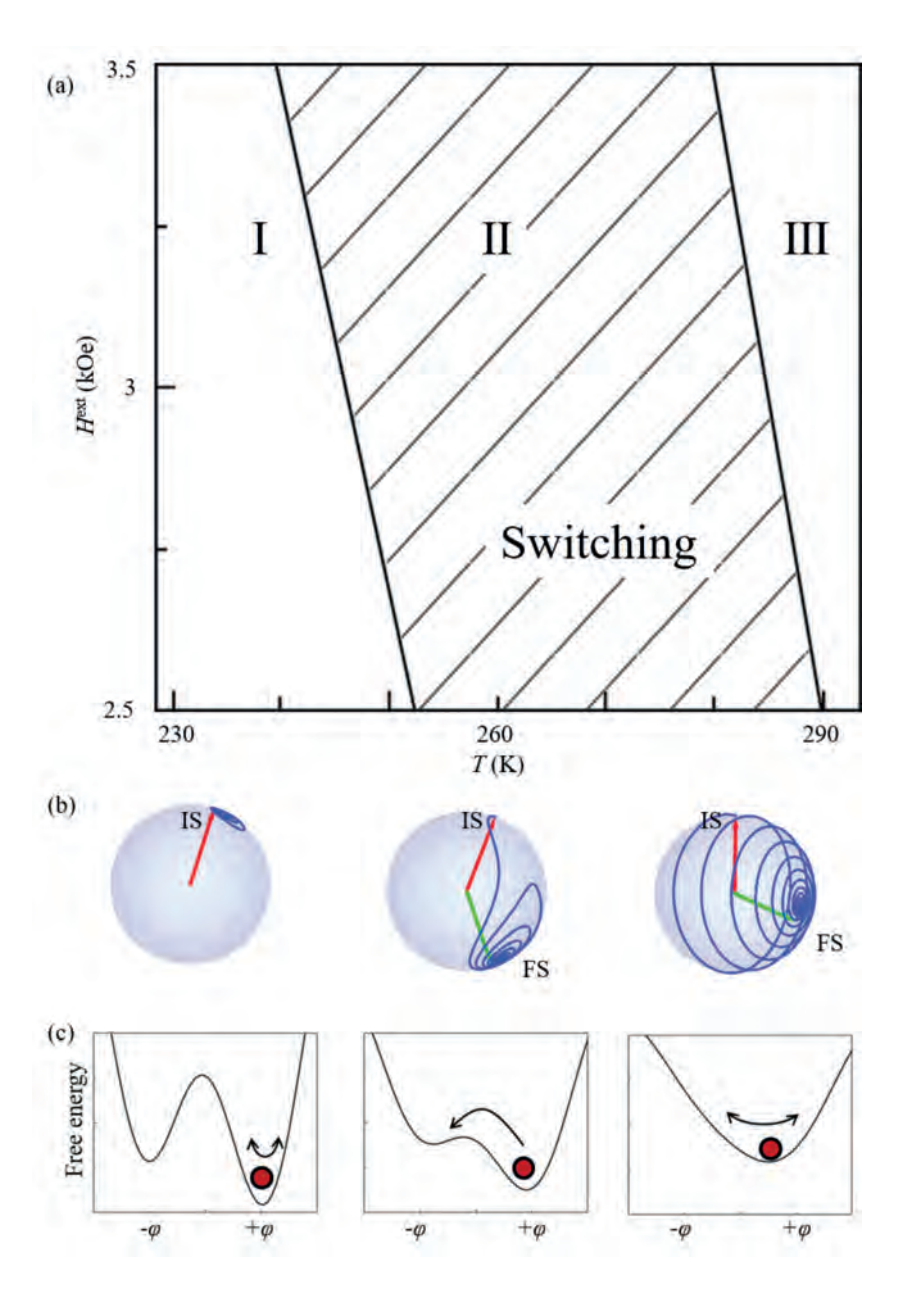


Fig. 4.9 . (a) Calculated HT-phase diagram of the final magnetization state. Hatched area corresponds to the reversed magnetization. Three types of dynamics (I-III) are described using 3D trajectories (b) and free energy profiles (c). The symbols IS and FS on the trajectories stand for the initial and final states, respectively.

Fig. 4.9(a) summarizes combinations of the applied magnetic fields and the bias temperatures for which the laser-induced magnetization dynamics eventually results in the switching of the magnetization between two stable states. It is seen

that at a fixed magnetic field, the switching is possible only in a relatively narrow range of temperatures. This range shifts to lower temperatures upon an increase in the strength of the applied magnetic field. Indeed, a temperature increase results in a decrease in the anisotropy field  $\mathbf{H}^{\mathrm{a}}$ . To preserve the conditions leading to the switching, upon an increase of the bias temperature, the applied magnetic field must be decreased. Upon even further increase of the bias temperature, the magnetic anisotropy does not result in a potential barrier between the initial and the final states any longer and the concept of switching loses its sense. Fig. 4.9(b) shows the route of the precessional dynamics on the unit sphere for three different areas of the diagram from Fig. 4.9(a). The corresponding profiles of the free energy and the trajectories of the magnetization are presented in Fig. 4.9(c), respectively. The results of the modelling are in good qualitative agreement with the experimental data shown in Fig. 4.7. However, the experimentally observed range of temperatures at which the switching is possible is much narrower than the one in theory. This discrepancy can be explained by the fact that our simple model does not account for stochastic magnetic fields randomly affecting spins in a magnet at nonzero temperatures. An inhomogeneous heating across the sample thickness also can be a reason for the observed differences between the experiment and modelling.

### 4.6 Conclusions

Using femtosecond laser pulses and laser-induced heating, we have experimentally explored heat-assisted magnetization dynamics in external magnetic fields and variable temperatures. More particularly, we reveal how the magnetization dynamics depends on magnetic field, laser fluence and sample temperature. Our investigations demonstrated that heat-assisted magnetic recording can, in principle, be accomplished only within a relatively confined range of parameters.

In our modelling, we treated magnetization as a macroscopic order parameter. This approach allowed us to define the range of parameters governed by the optimal height of the potential barrier that separates two bit-states. This barrier should be low enough to allow the switching but not so low as to undermine the stability of the bit states. In other words, if the barrier height is reduced excessively, the stability of the bit states is lost and the two minima can no longer be distinguished from each other. However, while our model provided valuable insights and was in good qualitative agreement with experimental data, it also highlighted the need for further refinement. Notably, the experimentally observed range of temperatures where switching is possible was found to be much narrower than in theory.

This finding is of significant importance in the quest to optimize magnetic recording technologies. It implies that we must carefully select and control the operational parameters to facilitate deterministic switching, an essential factor for the reliable operation of data storage devices.

### Literature

- E. Beaurepaire, J.-C. Merle, A. Daunois, and J.-Y. Bigot, Ultrafast spin dynamics in ferromagnetic nickel, Physical review letters 76 (22), 4250 (1996).
- [2] C. D. Stanciu, F. Hansteen, A. V. Kimel, A. Kirilyuk, A. Tsukamoto, A. Itoh, and T. Rasing, Alloptical magnetic recording with circularly polarized light, Physical review letters 99 (4), 047601 (2007).
- [3] A. Kimel, R. Pisarev, J. Hohlfeld, and T. Rasing, Ultrafast quenching of the antiferromagnetic order in F e B o 3: Direct optical probing of the phonon-magnon coupling, Physical review letters 89 (28), 287401 (2002).
- [4] A. Kirilyuk, A. V. Kimel, and T. Rasing, Ultrafast optical manipulation of magnetic order, Reviews of Modern Physics 82 (3), 2731-2784 (2010).
- J. Stöhr and H. C. Siegmann, Magnetism, Vol. 5, (2006).
- [6] A. Kimel, A. Kalashnikova, A. Pogrebna, and A. Zvezdin, Fundamentals and perspectives of ultrafast photoferroic recording, Physics Reports 852, 1-46 (2020).
- [7] I. Tudosa, C. Stamm, A. Kashuba, F. King, H. Siegmann, J. Stöhr, G. Ju, B. Lu, and D. Weller, The ultimate speed of magnetic switching in granular recording media, Nature 428 (6985), 831-833 (2004).
- K. Hono, Y. Takahashi, G. Ju, J.-U. Thiele, A. Ajan, X. Yang, R. Ruiz, and L. Wan, Heat-assisted magnetic recording media materials, MRS Bulletin 43 (2), 93-99 (2018).
- M. Kief and R. Victora, Materials for heat-assisted magnetic recording, MRS Bulletin 43 (2), 87-92 (2018).
- [10] M. H. Kryder, E. C. Gage, T. W. McDaniel, W. A. Challener, R. E. Rottmayer, G. Ju, Y.-T. Hsia, and M. F. Erden, Heat assisted magnetic recording, Proceedings of the IEEE 96 (11), 1810-1835 (2008).
- [11] A. V. Kimel and M. Li, Writing magnetic memory with ultrashort light pulses, Nature Reviews Materials 4 (3), 189-200 (2019).
- [12] C. Davies, T. Janssen, J. Mentink, A. Tsukamoto, A. Kimel, A. Van Der Meer, A. Stupakiewicz, and A. Kirilyuk, Pathways for single-shot all-optical switching of magnetization in ferrimagnets, Physical Review Applied 13 (2), 024064 (2020).
- [13] C. Banerjee, N. Teichert, K. Siewierska, Z. Gercsi, G. Atcheson, P. Stamenov, K. Rode, J. Coey, and J. Besbas, Single pulse all-optical toggle switching of magnetization without gadolinium in the ferrimagnet Mn2RuxGa, Nature communications 11 (1), 4444 (2020).
- [14] T. Ostler et al., Ultrafast heating as a sufficient stimulus for magnetization reversal in a ferrimagnet, Nature communications 3 (1), 666 (2012).
- [15] J. H. Mentink, J. Hellsvik, D. Afanasiev, B. Ivanov, A. Kirilyuk, A. Kimel, O. Eriksson, M. Katsnelson, and T. Rasing, Ultrafast spin dynamics in multisublattice magnets, Physical review letters 108 (5), 057202 (2012).

- [16] Y. Yang, R. B. Wilson, J. Gorchon, C.-H. Lambert, S. Salahuddin, and J. Bokor, Ultrafast magnetization reversal by picosecond electrical pulses, Science advances 3 (11), e1603117 (2017).
- [17] C. Davies et al., Anomalously damped heat-assisted route for precessional magnetization reversal in an iron garnet, Physical review letters 122 (2), 027202 (2019).
- [18] V. Fratello, S. Slusky, C. Brandle, and M. Norelli, Growth-induced anisotropy in bismuth: Rareearth iron garnets, Journal of applied physics 60 (7), 2488-2497 (1986).
- [19] G. Scott and D. Lacklison, Magnetooptic properties and applications of bismuth substituted iron garnets, IEEE Transactions on Magnetics 12 (4), 292-311 (1976).
- [20] V. Doormann, J. P. Krumme, and H. Lenz, Optical and magneto-optical tensor spectra of bismuth-substituted yttrium-iron-garnet films, Journal of applied physics 68 (7), 3544-3553 (1990).
- [21] I. Dolgikh, F. Formisano, K. Prabhakara, M. Logunov, A. Zvezdin, P. Christianen, and A. Kimel, Spin dynamics driven by ultrafast laser-induced heating of iron garnet in high magnetic fields, Applied Physics Letters 120 (1) (2022).
- [22] W. Crossley, R. Cooper, J. Page, and R. Van Stapele, Faraday rotation in rare-earth iron garnets, Physical Review 181 (2), 896 (1969).
- [23] P. Hansen, C.-P. Klages, J. Schuldt, and K. Witter, Magnetic and magneto-optical properties of bismuth-substituted lutetium iron garnet films, Physical Review B 31 (9), 5858 (1985).
- [24] M. Gerasimov, M. Logunov, A. Spirin, Y. N. Nozdrin, and I. Tokman, Time evolution of domainwall motion induced by nanosecond laser pulses, Physical Review B 94 (1), 014434 (2016).
- [25] C. Back, D. Weller, J. Heidmann, D. Mauri, D. Guarisco, E. Garwin, and H. Siegmann, Magnetization reversal in ultrashort magnetic field pulses, Physical review letters 81 (15), 3251 (1998).
- [26] Y. Hashimoto et al., Ultrafast time-resolved magneto-optical imaging of all-optical switching in GdFeCo with femtosecond time-resolution and a µm spatial-resolution, Review of Scientific Instruments 85 (6) (2014).
- [27] A. B. Harris and H. Meyer, Calorimetric determination of energy levels in rare-earth and yttriumiron garnets, Physical Review 127 (1), 101 (1962).
- [28] M. Khoshakhlagh, J. Islamian, S. Abedi, and B. Mahmoudian, Development of scintillators in nuclear medicine, World journal of nuclear medicine 14 (03), 156-159 (2015).
- [29] M. Guillot, F. Tchéou, A. Marchand, P. Feldmann, and R. Lagnier, Specific heat in Erbium and Yttrium Iron garnet crystals, Zeitschrift für Physik B Condensed Matter 44, 53-57 (1981).
- [30] T. Mirianashvili, V. Varazashvili, M. Tsarakhov, and T. Pavlenishvili, Heat capacity and ferromagnetic transformation of lutetium iron garnet, Zhurnal Neorganicheskoj Khimii 42 (6), 1026-1028 (1997).

- [31] S. Parida, S. Rakshit, and Z. Singh, Heat capacities, order-disorder transitions, and thermodynamic properties of rare-earth orthoferrites and rare-earth iron garnets, Journal of Solid State Chemistry 181 (1), 101-121 (2008).
- [32] A. Zvezdin, Field induced phase transitions in ferrimagnets, Handbook of Magnetic Materials 9, 405-543 (1995).
- [33] V. Yurlov et al., Magnetization switching by nanosecond pulse of electric current in thin ferrimagnetic film near compensation temperature, Applied Physics Letters 116 (22) (2020).
- [34] H. Leutwyler, Nonrelativistic effective lagrangians, Physical Review D 49 (6), 3033 (1994).
- [35] C. P. Hofmann, Ferromagnets and antiferromagnets in the effective Lagrangian perspective, AIP Conference Proceedings, pp. 305-308, (2002).
- [36] F. Hansteen, A. Kimel, A. Kirilyuk, and T. Rasing, Femtosecond photomagnetic switching of spins in ferrimagnetic garnet films, Physical review letters 95 (4), 047402 (2005).
- [37] F. Hansteen, A. Kimel, A. Kirilyuk, and T. Rasing, Nonthermal ultrafast optical control of the magnetization in garnet films, Physical Review B 73 (1), 014421 (2006).

# CHAPTER 5

# Double pulse all-optical coherent control of spins in antiferromagnetic rare-earth orthoferrite<sup>3</sup>

Control of magnetic order with femtosecond optical pulses offers an important route towards future magneto-photonic hybrid devices for data processing and storage. However, the operation rates of such devices are fundamentally limited by the minimum time interval between two subsequent write/erase events. In this chapter, we investigate this limit by studying coherent spin-reorientation transitions in the antiferromagnetic rare-earth orthoferrite (Sm,Tb)FeO<sub>3</sub> under double-pump optical excitation.

Rare-earth orthoferrites are insulating oxides where magnetic Fe<sup>3+</sup> ions are coupled antiferromagnetically, resulting in a canted spin structure with weak ferromagnetism. Despite their antiferromagnetic coupling, the nonequilibrium spin dynamics in such materials share several features with ferrimagnetic dielectrics due to the presence of multiple magnetic sublattices and complex anisotropies.

We reveal that during a 5–20 ps time window following the first pump pulse, the system becomes insensitive to a second optical excitation. This insensitiveness, whose duration depends on the initial sample temperature, is attributed to a peak in damping of nonlinear antiferromagnetic dynamics near the spin-reorientation phase transition. Our findings not only expose fundamental characteristics of ultrafast spin dynamics in antiferromagnetic media but also contribute to the design of magneto-photonic hybrid devices capable of operation at terahertz (THz) frequencies.

Adapted from: N.E. Khokhlov, A.E. Dolgikh, B.A. Ivanov and A.V. Kimel "Double pulse all-optical coherent control of ultrafast spin-reorientation in antiferromagnetic rare-earth orthoferrite" APL Materials 12(5), 2024. Contribution: conducting an experiment, data analysis, theoretical modelling and writing the article.

#### 5.1 Motivation

Antiferromagnets are the largest, but probably the least explored, class of magnetically ordered materials discovered only in the 20<sup>th</sup> century [1,2]. The magnetic order in antiferromagnets is characterized by mutually antiparallel alignment of neighboring spins, such that their net magnetic moment is either zero or vanishingly small. In the simplest case of a two-sublattice antiferromagnet, the order can be modelled as two ferromagnets with mutually antiparallel magnetizations of the sub-lattices –  $\mathbf{M}_1$  and  $\mathbf{M}_2$  – so that the whole material is described by the antiferromagnetic Néel vector  $L = \mathbf{M}_1 + \mathbf{M}_2$ .

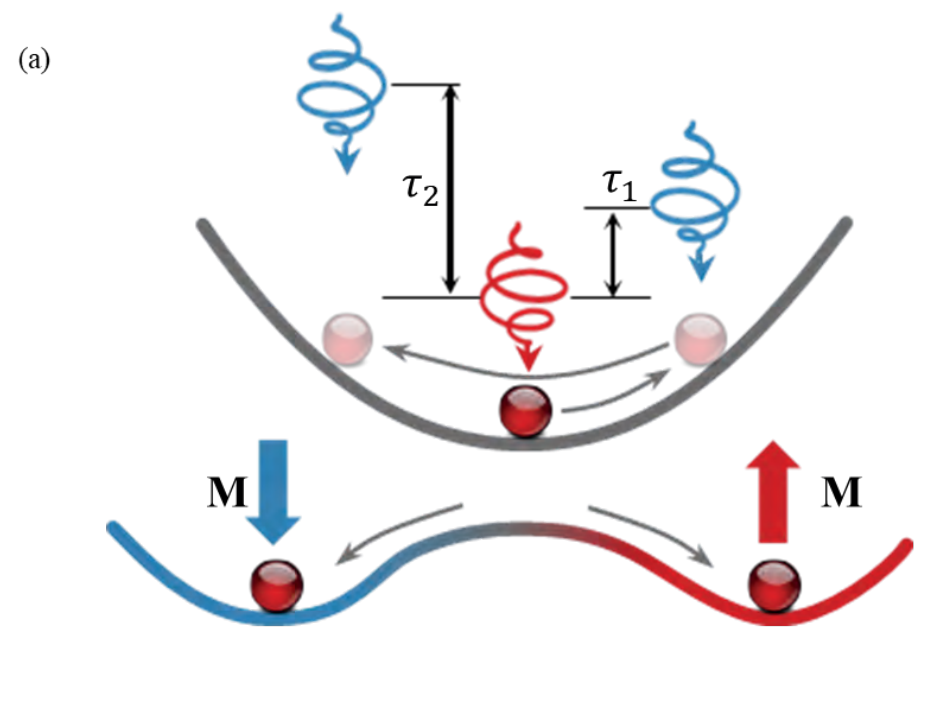
Due to high frequencies of intrinsic spin resonances, often reaching the landmark of 1 THz, the antiferromagnets are seen as the materials that must hit the fastest and the least-dissipative mechanisms for writing magnetic bits in future data storage [3]. Understanding how to control spins in antiferromagnets and revealing the characteristic time-scales, which define the fundamental limits on the speed of such a control, are thus among the most heavily debated questions in contemporary magnetism [4].

Rare-earth (RE) orthoferrites have long been offered a very fruitful playground for this research. First, due to the very strong temperature dependence of magnetic anisotropy, these materials possess a heat-induced Spin-Reorientation phase Transition (SRT) [5]. Using a femtosecond laser pulse as an ultrafast heater, it was possible to launch spin dynamics and to study spin-reorientation in antiferromagnets at the unprecedentedly fast timescale [6]. Second, due to strong opto-magnetic effects, circularly polarized femtosecond laser pulses can act on spins in these materials as equally short pulses of effective magnetic field with a polarity defined by the helicity of light [7].

A combination of these two mechanisms of launching spin dynamics led, in principle, to the discovery of the inertia of spins in antiferromagnets [8] and to the routes of coherent control of SRT [9]. Although, intuitively, heat-induced SRT can proceed along two energetically equivalent routes with the material eventually ending up in a multidomain state, ultrashort pulses of opto-magnetic fields were suggested to dynamically break the degeneracy and steer the medium to a state defined by the helicity of the light pulse [9]. Later, the same principle of dynamical degeneracy breaking was employed to demonstrate coherent control of SRT in orthoferrites with the help of a pair of pulses - a properly timed femtosecond laserheat pulse and a nearly single cycle pulse of THz magnetic field [10].

Here, we further explore the coherent control of SRT with a pair of laser pump pulses. Employing two circularly polarized pulses acting as both ultrafast heater and opto-magnetic field, the time delay au of the second-arrived pump should define the final magnetization orientation in a controllable manner (Fig. 5.1(a)). In experiments, we reveal a strong and previously ignored effect of heavily increased damping of spin precession near the phase transition. The damping significantly affects the result of the action of the pair of pulses. We showed that if the first pulse heats the orthoferrite to a temperature near the SRT, the material becomes practically insensitive to the second pulse in the subsequent time window of 5-20 ps. According to the simulations based on the models employed before, such an insensitivity can indeed be observed, but in this case, it must be observed periodically at later time delays as well. We propose an upgrade for the existing model that accounts for the increased damping and enables a match of the modeling with the experimental results.

The idea of our experiment is to control the route with a pair of laser pulses and reveal how the final state depends on the time delay between the pulses in a pair. An expected scenario that we aim to verify is shown in Fig. 5.1(a). The first pulse acts as an ultrafast heater and a pulse of opto-magnetic field. Hence, it launches a low-amplitude spin precession and simultaneously causes transient changes of thermodynamic equilibrium.



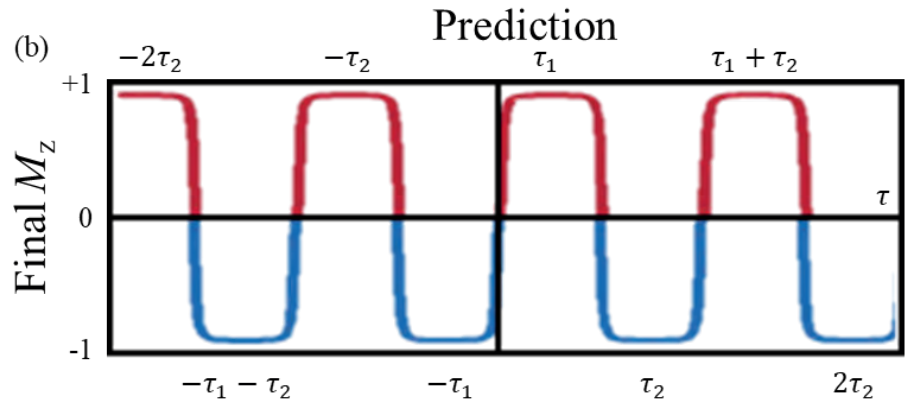


Fig. 5.1. (a) Schematic illustration of the coherent optical control of final magnetization at spinreorientation phase transition. (b) Prediction of the final magnetization orientation depending on the time delay between two pump pulses, assuming negligible energy loss within the spin system.

Using a properly timed second pulse, which also acts as an ultrafast heater and an ultrashort pulse of the opto-magnetic field, one can push the spin system either to the state with the magnetization "up" or to the state with the magnetization "down". In this case, the first pump pulse excites the spin precession of a certain frequency in the system. Depending on the phase of this precession at the moment the second pulse is applied, the system can relax to one of two equivalent states: "up" or "down". Thus, we expected to see a periodic pattern corresponding to the period of oscillation of the spin system (Fig. 5.1(b)).

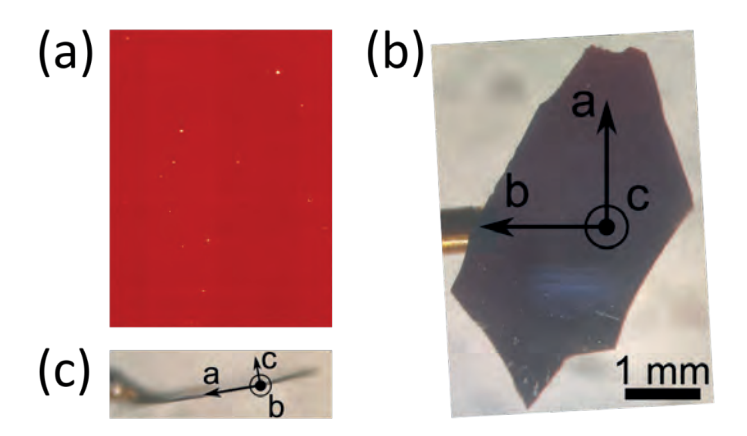


Fig. 5.2. Photo of the sample with indicated crystallographic axes (a,b,c-axes).

## 5.2 Sample

sample studied was the single-crystalline rare-earth orthoferrite (Sm<sub>0.55</sub>Tb<sub>0.45</sub>)FeO<sub>3</sub>. The crystal was grown by prof. A.M. Balbashov at Moscow Power Engineering Institute using the floating-zone method [11]. Owing to the balance between Sm and Tb contents, this orthoferrite possesses a low linear crystallographic birefringence, which results in a huge effective Faraday rotation. In almost all the pure RE orthoferrites, the SRT regions lie at low temperatures. The dependence of the magnetic anisotropy energy on temperature is strongly influenced by details in the electronic structure of the RE ions. By mixing two different RE ion types in one orthoferrite, we could achieve SRT at higher temperatures that are usual for other rare-earth orthoferrites. The SRT temperature range lies somewhere between the anisotropy energies of each of the corresponding pure orthoferrites. Due to the mixture of Sm $^{3+}$  and Tb $^{3+}$  ions the  $\Gamma_2$ to  $\Gamma_4$  SRT in (Sm<sub>0.55</sub>Tb<sub>0.45</sub>)FeO<sub>3</sub> should be positioned near room temperature. For the study the bulk crystal was cut in the form of a 158  $\mu m$  thin plane-parallel plate with its normal along the c-axis (Fig. 5.2). Single-crystal X-ray diffraction (XRD) confirms that the sample under the study is a c-cut single crystal with an orthorhombic P structure. The crystal lattice parameters are a = 5.38 Å, b = 5.58 Å, c = 7.60 Å.

The magnetic structure of the crystal can be modelled as a two-sublattice antiferromagnet with magnetizations  $M_1$  and  $M_2$ , respectively. The exchange interaction favours their mutually antiparallel orientations, but due to the Dzyaloshinskii-Moriya interaction  $\mathbf{M}_1$  and  $\mathbf{M}_2$  are slightly canted by about 1°, resulting in a non-zero net magnetization  $\mathbf{M} = \mathbf{M}_1 + \mathbf{M}_2 \neq 0$ . The magnetization  ${f M}$  and the antiferromagnetic Néel vector  ${f L}={f S}_1-{f S}_2$  are orthogonal to each other (Fig. 5.3(a)). At temperatures  $T < 215 {
m K}$ , the spins and  ${f L}$  are aligned along the c crystallographic axis, while M is along the a-axis ( $\Gamma_2$  phase). Due to the strong temperature dependence of the magneto-crystalline anisotropy, in the range  $215 {
m K} < T < 250 {
m K}$  the spins continuously rotate in the ac plane ( $\Gamma_{24}$  phase). At  $T>250\mathrm{K}$ , the spins are along the a-axis, while  $\mathbf{M}$  is along the c-axis ( $\Gamma_4$  phase). We can experimentally confirm the presence of SRT in the sample, measuring the Faraday effect for light propagation along the c-axis and, therefore, sensitive to the out-of-plane magnetization component (Fig. 5.3(b) and (c)). It is seen from the magneto-optical images that a temperature increase promotes spin reorientation from phase  $\Gamma_2$  with in-plane  ${f M}$  orientation and indistinguishable domain structure

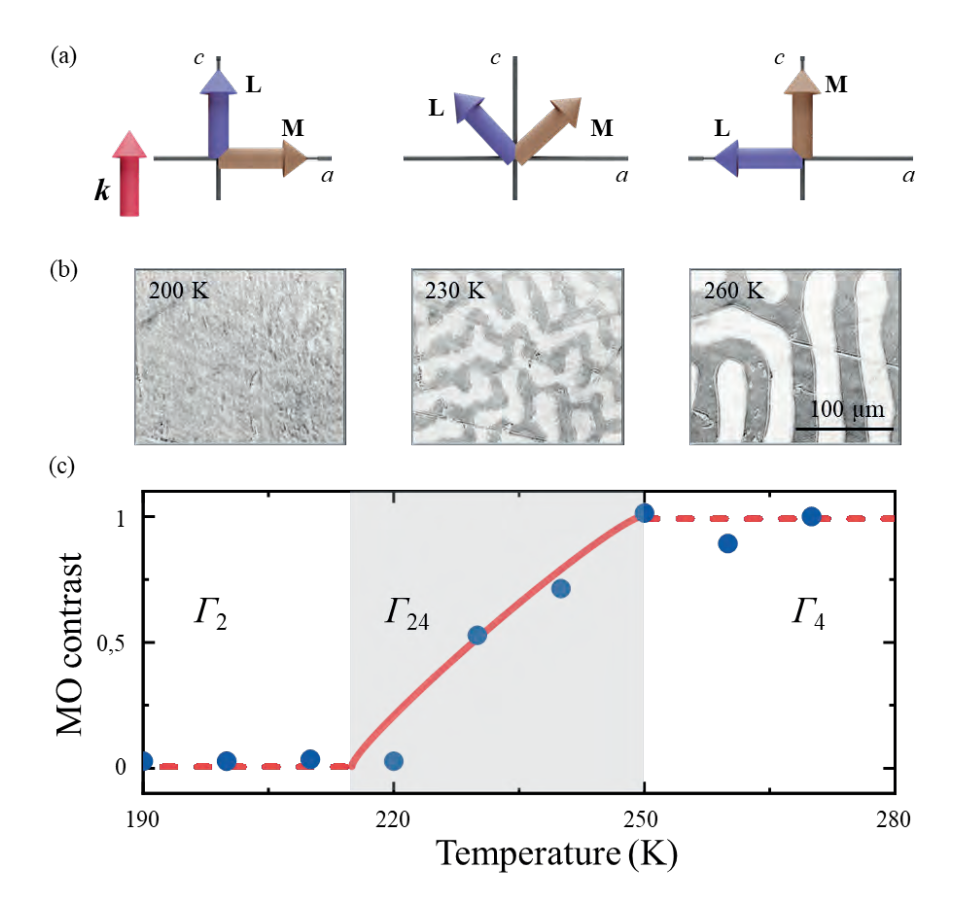


Fig. 5.3. (a) Orientation of the antiferromagnetic vector  ${f L}$  and the net magnetization  ${f M}$  of the sample in low-temperature  $(\Gamma_2)$ , angular  $(\Gamma_{24})$ , and high-temperature  $(\Gamma_4)$  phases. Vector **k** represents the direction of the probe pulse propagation. (b) Magnetic domain structure of (SmTb)FeO<sub>3</sub>, observed in polarized microscope at  $\Gamma_2$  (T = 200 K),  $\Gamma_{24}$  (T = 230 K) and  $\Gamma_4$  (T = 260 K). (c) Temperature dependence of magneto-optical contrast between opposite domains (symbols). The line is the theoretical dependence.

(left panel in Fig. 5.3(b)) to phase  $\Gamma_4$  along one of the two equivalent routes leading either to a state with the magnetization "up" or to a state with magnetization "down", appearing as bright and dark domains on the camera (Fig. 5.3(b)).

To fit the experimental data, we used the model from [12]. Let's introduce the angle  $\varphi$  between the c-axis and the magnetization  ${f M}$ . Two second-order phase transitions occur at  $T_1$  and  $T_2$ . The stable solutions for the angle  $\varphi$  are:

$$arphi=rac{\pi}{2},\quad T\leq T_1;$$
  $\sin^2arphi=rac{T_2-T}{T_2-T_1},\quad T_1\leq T\leq T_2;$   $arphi=0,\quad T\geq T_2.$  (5.1)

Thus  $\varphi$  changes continuously between 0 and  $\pi/2$  with infinite slope at  $T_1$  and  $T_2$ . Magneto-optical contrast, shown in Fig. 5.3(c), were measured with the CCD camera with the presence of external magnetic field needed to saturate the sample. In this case we measured only one projection of the magnetization which is along the k:  $M_k = M \cos \varphi$ . According to the Eq. 5.1 theoretical dependence is derived as:

$$M_z = \left\{ egin{array}{ll} 0, & T \leq T_1; \\ \sqrt{\frac{T - T_1}{T_2 - T_1}}, \ T_1 \leq T \leq T_2; \\ 1, & T \geq T_2. \end{array} 
ight.$$
 (5.2)

## 5.3 Experimental details

To study the magnetization reorientation induced by a double-pulse laser excitation, we used a time-resolved magneto-optical pump-probe technique combined with magneto-optical imaging (Fig. 2.5). The sample is pumped with two 50 fs circularly polarized laser pulses with a central wavelength of 800 nm (photon energy 1.55 eV), generated by a Ti:sapphire amplifier at 1 kHz repetition rate. The time delay between the two pumps  $\tau$  is mechanically controlled in the range from -150 to +150 ps. The pulses follow the same path and pump the sample at an incidence angle of 11°. They are focused in spots with full width at a half maximum of 100 µm. Pump-induced changes in the sample are probed with a linearly polarized pulse with a wavelength converted from 800 to 650 nm using an optical parametric amplifier. The probe is unfocused to cover an area of about 3 mm<sup>2</sup> on the sample with a fluence four orders of magnitude lower than that of each pump pulse. The time delay between the first-arrived pump and probe is mechanically controlled from -0.5 to +1.5 ns. Two complementary sets of experiments are performed. The first used a CCD camera as a detector to obtain magneto-optical images of the sample [13]. In the second set of experiments, a diaphragm is placed in the probe beam, selecting only the pumped area. After this spatial filtering, the probe is detected with a balanced detector and lock-in amplifier, synchronized with a mechanical chopper placed on the pump path. In both cases, the measurements are sensitive to the out-of-plane component of the magnetization parallel to the c-axis. The sample is placed in a cold finger cryostat to control its initial temperature T. The experiments are performed without an external magnetic field. The helicities of the two pumps were set to be right-handed  $\sigma^+$  and left-handed  $\sigma^-$  with quarter-wave plates.

For single-pump experiments, the fluence of the pump was varied between 25 mJ/cm<sup>2</sup> and 165 mJ/cm<sup>2</sup>. Depending on the fluence and initial temperature of the sample, this pump could launch spin precession or even initiate the phase transition. For double-pump experiments, we set the fluences of the pump pulses to 67 mJ/cm $^2$  to such that one pump alone could not launch the SRT at  $T=170{
m K},$ but two pump pulses together were able to initiate and steer the phase transition.

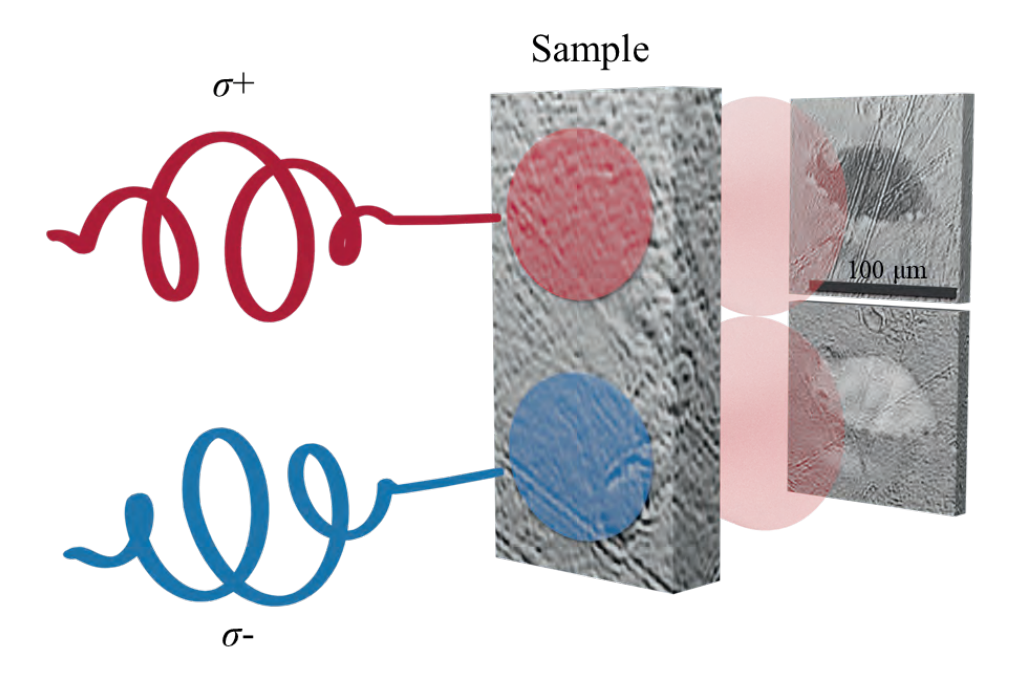


**Fig. 5.4.** Magnetic domains formed after single right-handed  $(\sigma^+)$  and left-handed  $(\sigma^-)$  circularly polarized pump. The initial sample's temperature was 170 K, and the pump fluence was 165 mJ/cm<sup>2</sup>. Pump-probe time delay was 1.5 ns.

# 5.4 Experimental results

The magnetization switching in orthoferrites at SRT with a single femtosecond laser pulse depends on the helicity of the pulse, its fluence, and the initial temperature of the sample [9]. As a starting point, we performed the single-pump switching to choose the pump pulses' parameters for the double-pump experiments. The sample is cooled to 170 K, below the SRT temperature  $T_1$ . Each pump fluence was set to  $F=165 {
m mJ/cm^2}$ . Pump pulses with opposite helicity generate the magnetic domains with opposite magnetization directions [14]. These domains appear as black and white areas (Fig. 5.4).

Next, we perform double-pump experiments with a CCD camera. Fig. 5.5(a) shows that the sign of magnetization in the final state, measured at 1.5 ns after the laser excitation, depends dramatically on the time delay between the pump pulses  $\tau$ .

To obtain a better understanding of the observed dynamics, we performed doublepump experiments with the balance photodetector as a function of temperature Tand time delay  $\tau$ . In Fig. 5.5(b) we plot the experimentally defined diagram showing the magneto-optical contrast of the pumped domain at 1.5 ns after the laser excitation as a function of T and  $\tau$ .

At temperatures equal or higher than  $T_1$ , i.e. T > 220 K, after the application of two pump pulses, a multidomain state forms, and the total signal is zero. At temperatures just below the SRT, i.e. 190 < T < 220 K, the double-pump excitation forms a single domain with the magnetization direction defined by the helicity of the earliest pump pulse independently on the pump-pump time delay  $\tau$ .

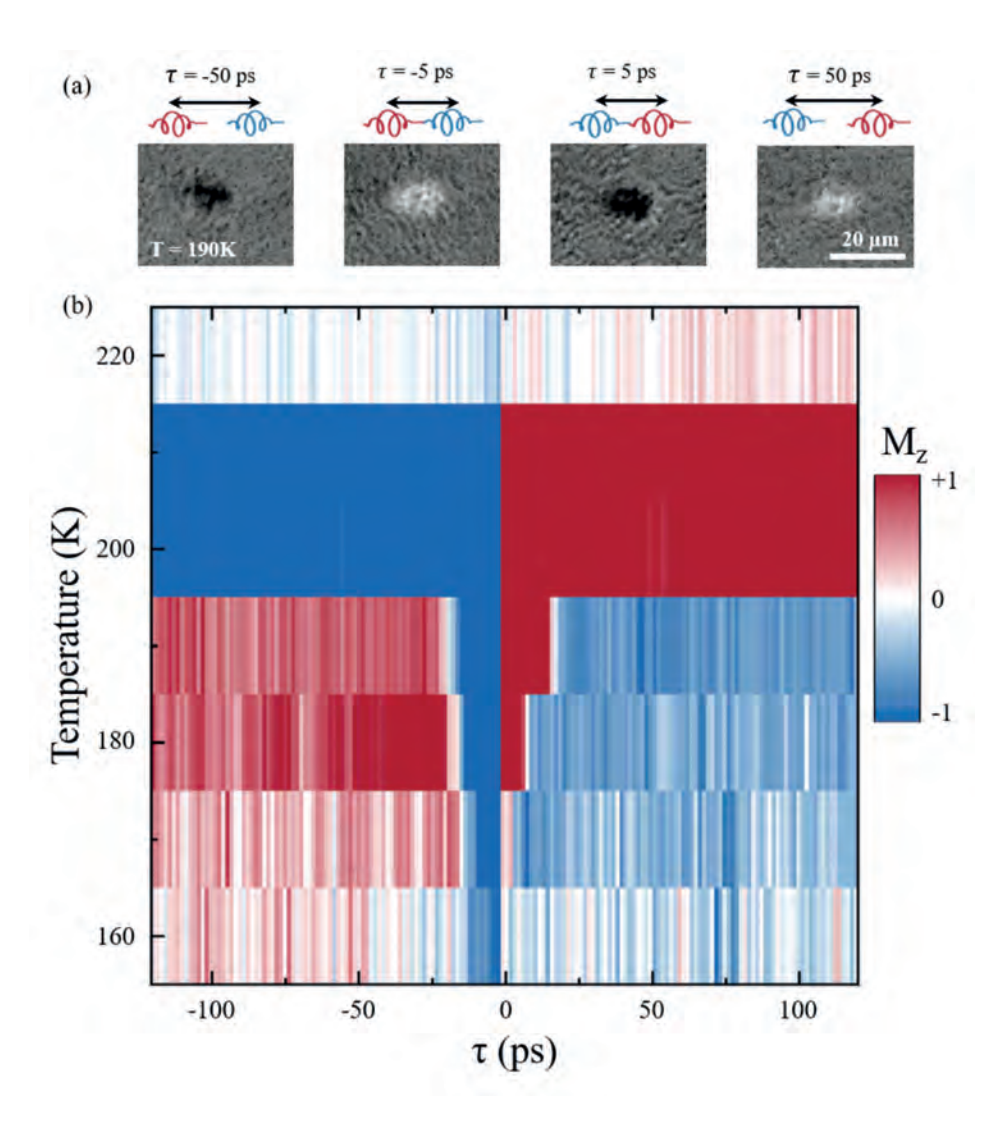


**Fig. 5.5.** (a) Magneto-optical images of the reorientation process at t = 1.5 ns for different pump-pump delays  $\tau$  observed with the CCD camera at T = 190 K. (b) Experimental diagram of magnetization's final state in coordinates of pump-pump delay  $\tau$  and initial temperature of the sample T. Fluences of both pumps were equal to 67 mJ/cm².

At lower temperatures 170 < T < 190 K, the time delay  $\tau$  begins to play a crucial role. If  $\tau$  is less than the critical value  $\tau_c$ , the helicity of the first-arrived pump determines the final orientation of magnetization. However, if  $\tau > \tau_c$ , the magnetization orientation is defined by the helicity of the latest pulse. At lower temperatures of T < 170 K, the optical pump pulses do not sufficiently heat the system to trigger SRT.

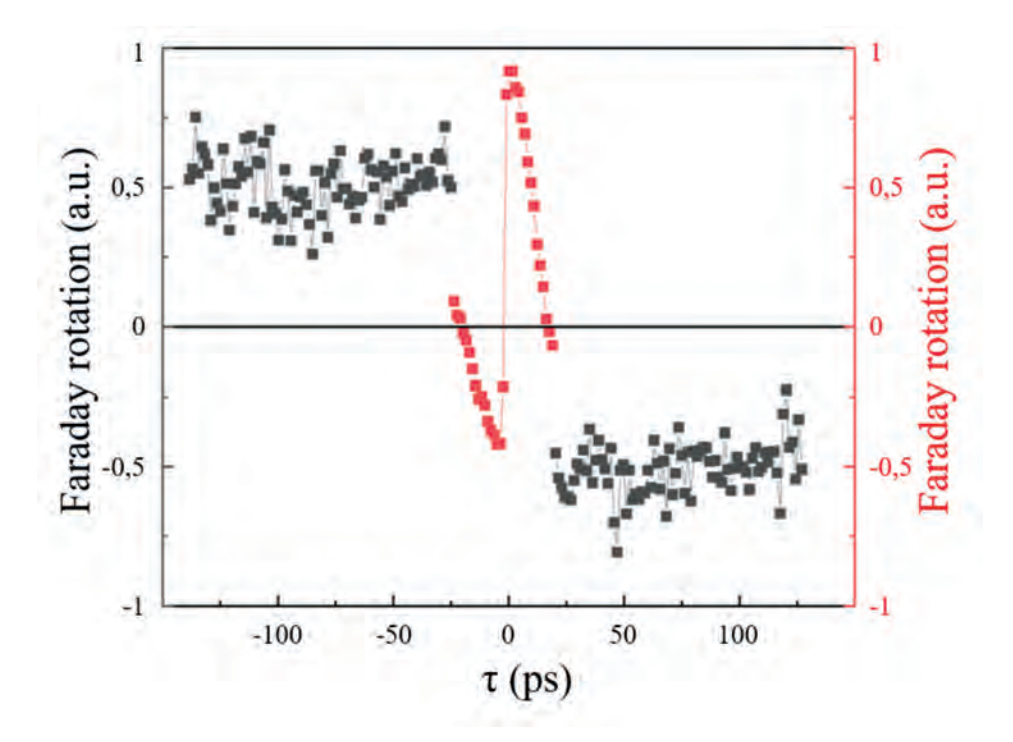


**Fig. 5.6.** Dynamics of the Faraday rotation deduced from Fig. 5.5(b) in the case of T = 190 K. The points represent experimental measurements conducted using a balance photodetector. Data observed at  $|\tau|$  < 15 ps was normalized to different values in order to highlight the regions with opposite signs of the Faraday rotation.

To provide greater clarity and to highlight regions of consistent signs of the Faraday rotation, indicating the formation of a unidirectional domain, we selected one of the slices from the diagram shown in Fig. 5.5(b). This slice was chosen at  $T=190\,\mathrm{K}$ , where the time interval between two pump-pulses  $\tau$  plays a significant role in the domain formation (Fig. 5.6). The integral value of the Faraday rotation in the domain region varies for short ( $\tau<20\,\mathrm{ps}$ ) and long ( $\tau>20\,\mathrm{ps}$ ) delays between pulses, as observed in both the diagram (Fig. 5.5(b)) and the images captured with the CCD camera (Fig. 5.5(a)). For visualization, the obtained dependence of the Faraday rotation on  $\tau$  was normalized to different values for  $\tau<20\,\mathrm{ps}$  and  $\tau>20\,\mathrm{ps}$ . The resulting dependence shows that at a short delay; the Faraday rotation significantly depends on the time between the pulses  $\tau$  and increases in absolute value as this time decreases. Conversely, for long delays between the pulses, the Faraday rotation appears to be independent of the delay time between the pumppulses, remaining constant up to the maximum delay achievable with the setup ( $\tau=150\,\mathrm{ps}$ ).

To manipulate the final magnetization state with the help of  $\tau$ , we performed the same experiments for lower and higher energies of one of pumps, respectively (Fig. 5.7). The first pulse, arriving at negative  $\tau$ , had a constant fluence of  $F=67~\mathrm{mJ/cm^2},$  matching the values used to obtain the diagram in Fig. 5.5. The fluence of the pulse arriving first at positive  $\tau$  varied from 50 to 90 mJ/cm<sup>2</sup>.

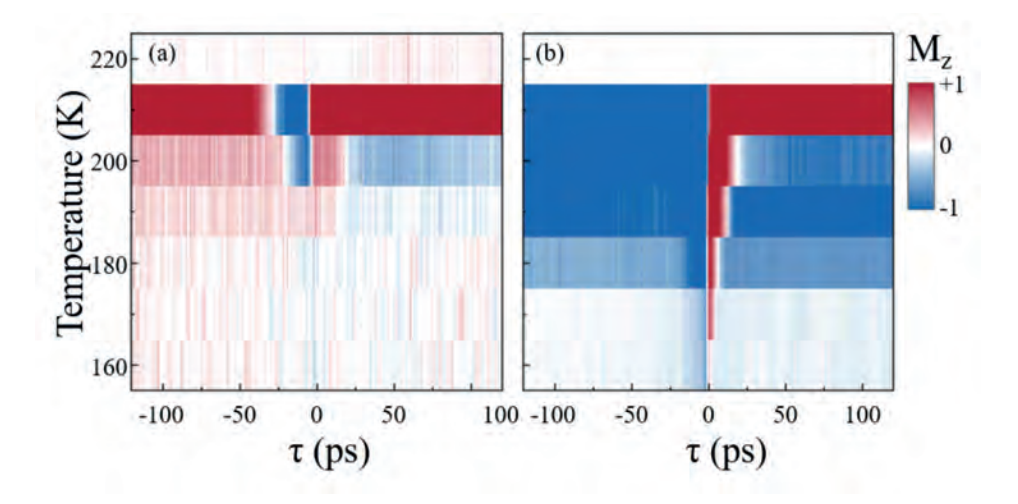


**Fig. 5.7.** Temperature (T) – time delay between pump pulses  $(\tau_{pp})$  diagrams of the reorientation for uncompensated power of pump pulses. P1 and P2 pump pulses arrive first at positive and negative delay times, correspondingly. Diagrams represent dependences for different pump pulses powers: (a)  $P_1$  fluence was 67 mJ/cm<sup>2</sup>,  $P_2$  fluence was 50 mJ/cm<sup>2</sup> (b)  $P_1$  fluence was 67 mJ/cm<sup>2</sup>,  $P_2$  fluence was 90 mJ/cm<sup>2</sup>.

The diagram becomes asymmetric, and the second arrived pump indeed affects the final state. Specifically, if the energy is decreased, in the range 200-220 K, the strongest pump determines the final state at long time delays (au>20ps). An intriguing situation occurs at  $\tau < 20$  ps, where the helicity of the first pump defines the final state, and the second pump only makes the contrast stronger. The same behavior is observed at temperatures 175-200 K, if the energy of one of the pumps is increased. In this case, the first-arrived pump defies the state only for au < 20 ps. After that, the second pump switches the magnetization according to its helicity. Regardless of the energy ratio of the pumps, a multi-domain state emerges with an initial temperature that is higher than  $T_1$ .

Experimental diagrams of magnetization's final state show strong dependence on the initial temperature of the sample T. To understand the reasons for this dependence more deeply, we investigated spin precession triggered by a single circular polarized pump pulse (Fig. 5.8). The pump fluence was set at 25 mJ/cm<sup>2</sup>,

and the sample temperature was varied from 170 K to 250 K. Data were collected using a balanced photodetector, which measured the integral value of the Faraday rotation in the pump-affected area. The temperature dependence was obtained using the  $\sigma^+$  polarization of the pump. Additionally, the phase difference of the oscillations by  $\pi$  was shown for the  $\sigma^-$  polarization of the pump at T=170 K.

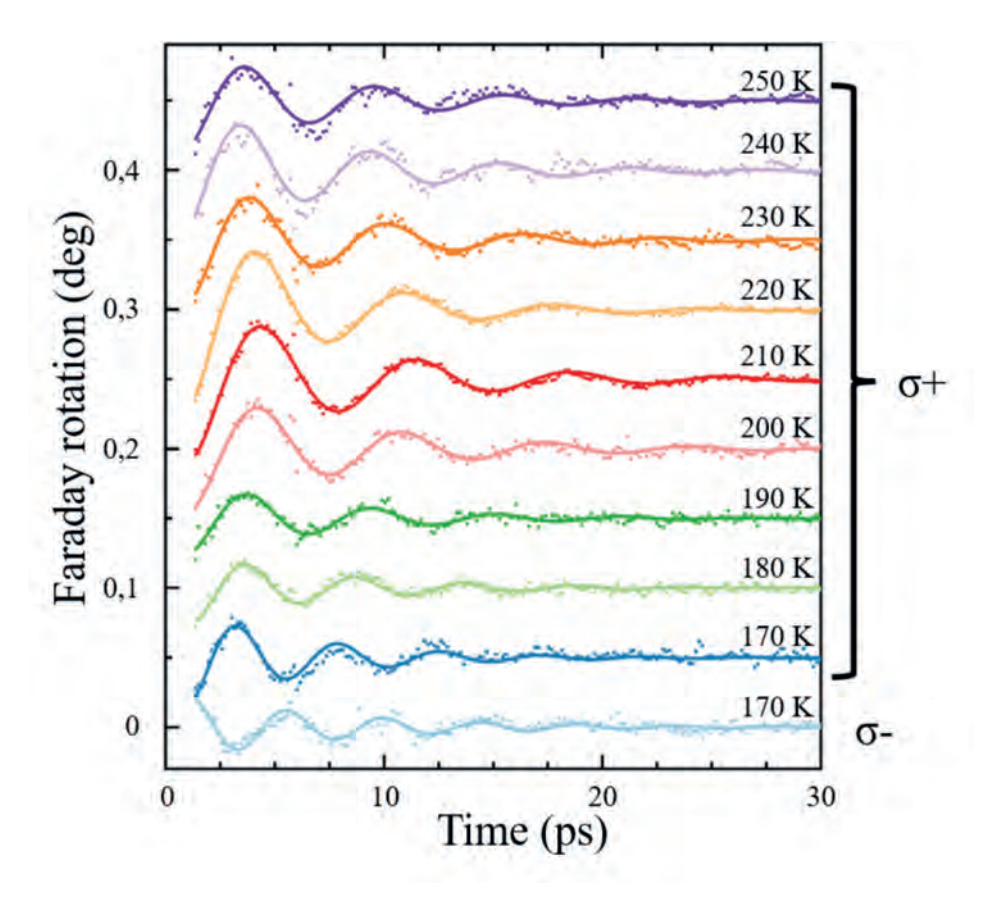


Fig. 5.8. Magnetization dynamics in single-pump experiments at different initial temperatures. The fluence of the pump is 25 mJ/cm<sup>2</sup>. The switching of the pump helicity results in switching of the initial phase of the oscillations, as shown for initial temperature of 170 K. Dots - experimental data points; lines - fits with damped sine function.

# 5.5 Discussion

To simulate laser-induced spin dynamics, we solved the equation of motion for the antiferromagnetic vector L using the principles of Lagrangian mechanics [15,16]. Lagrangian for two exchange-coupled spin subsystems is represented as:

$$\mathcal{L} = \frac{\hbar}{2\gamma H_{\text{ex}}} \left(\frac{d\mathbf{l}}{dt}\right)^2 - \frac{\hbar}{H_{\text{ex}}} \left(\mathbf{H}_{\text{eff}} \cdot \left[\mathbf{l} \times \frac{d\mathbf{l}}{dt}\right]\right) - W(\mathbf{l}), \tag{5.3}$$

where  $\mathbf{l} = \mathbf{L}/|\mathbf{L}|$  is the antiferromagnetic unit vector; t is time after the earliest pump; y is gyromagnetic ratio;  $H_{ex}$  represents the exchange field of the antiferromagnet;  $\mathbf{H}_{\mathrm{eff}}$  is the effective field, consisting of contributions of the Dzyaloshinskii-Moriya interaction  $\mathbf{H}_D$  and external magnetic field  $\mathbf{H}_{ext}$ ;  $W(\mathbf{l})$  can be treated as the potential energy. The contribution of  $\mathbf{H}_{ext}$  can be timeindependent and can include the effective field caused by inverse Faraday effect (IFE) [16]. The Dzyaloshinskii-Moria interaction term is expressed as  $\mathbf{H}_{\mathcal{D}} =$  $H_D[\mathbf{d} \times \mathbf{l}]$ , where  $\mathbf{d}$  is the unit vector along the b-axis. Nonlinear spin dynamics can be excited through the term bilinear over  $\mathbf{H}$  and  $\mathbf{H}_D$ , and the potential energy can be written as the following:

$$W(\mathbf{l}) = W_a(\mathbf{l}) + \frac{\gamma \hbar}{H_{ex}} H_D(\mathbf{H}[\mathbf{d} \times \mathbf{l}]). \tag{5.4}$$

In our experiment, the pulse effective field  $\mathbf{H} = \mathbf{H}(t)$  is caused by the inverse Faraday effect. It is directed along the c-axis and excites the planar motion of the  $\mathbf l$ within the ac-plane. The final differential equation for the angle  $\varphi$  between 1 and the a-axis is of the second order in respect of time [8,17]:

$$\frac{d^{2}\varphi}{dt^{2}}+2\zeta\frac{\mathrm{d}\varphi}{\mathrm{d}t}+\gamma\boldsymbol{H}_{\mathrm{ex}}\frac{d\boldsymbol{W}_{a}\left(\varphi\right)}{\mathrm{d}\varphi}=\gamma^{2}\boldsymbol{H}_{D}\boldsymbol{H}_{p}\left(t\right)\sin\varphi,\tag{5.5}$$

where the total length of  ${\bf L}$  is assumed to be conserved;  $\zeta$  is a damping parameter in the units of frequency;  $H_{p}\left(t
ight)$  is the pulse effective opto-magnetic field with duration of 50 fs and aligned either parallel ( $\sigma^+$ ) or antiparallel ( $\sigma^-$ ) with respect to the c-axis. The function  $W_a\left(\varphi\right)$  is the potential energy described by the magnetic anisotropy of the antiferromagnet. In our model,  $W_a\left(\varphi\right)$  is a function of temperature in accordance with the conventionally accepted model [12].

The energy  $W_a\left(\varphi\right)$  can be expressed as

$$W_a(\theta) = K_2 \sin^2 \varphi + K_4 \sin^4 \varphi \tag{5.6}$$

where  $K_2$  and  $K_4$  are the second-order and fourth-order anisotropy parameters, respectively. For rare-earth orthoferrites, the variation of  $W_{a}\left(\varphi\right)$  can be described with the temperature dependence of  $K_2 = K_2(T)$ , while  $K_4$  can be considered a constant [18]. This approximation is quite accurate for experimental data [19].

To mimic laser-induced heating, we assume that the temperature of the sample is a function of the pump-probe time delay, similarly to the model from [20]. In particular, we take into account that the time dependence of magnetic anisotropy is due to temperature-induced repopulation of the electronic states in highly anisotropic Sm<sup>3+</sup> and Tb<sup>3+</sup> ions. This repopulation occurs on a time scale of electron-phonon interaction for rare-earth ions, which could be estimated to be around 15 ps [20]. Furthermore, we suggest an increase in temperature of 25 K after one pump, as the action of both pumps is enough to induce SRT at  $T=170{
m K}$ . The results of the modeling are similar to those from [10] (Fig. 5.9), but they are clearly different with respect to the experimental observations. In the modeling, we indeed observe a triangle centered around au=0, similar to the experimental diagram in Fig. 5.5(b). This triangle reproduces the insensitivity of spins in the antiferromagnet to the second pump pulse. However, contrary to the experiment, this insensitivity also appears periodically at longer times  $\tau$  in the simulations (Fig. 5.9), but clearly absent in the experiment Fig. 5.5(b).

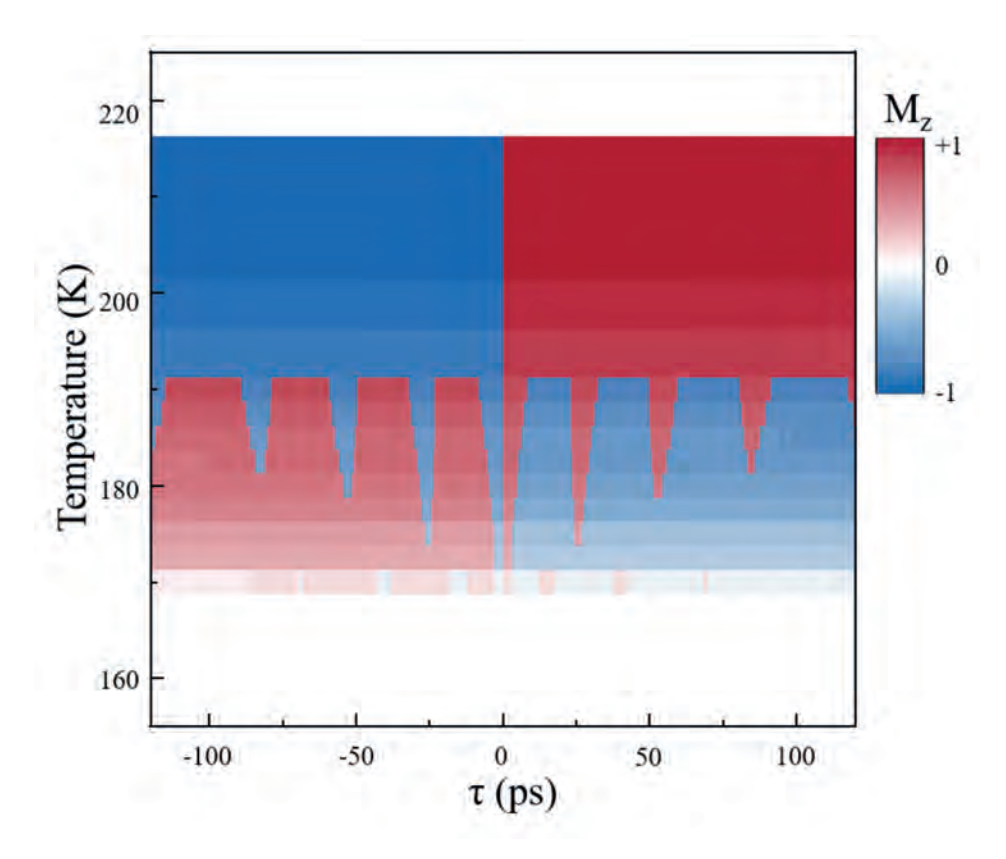


**Fig. 5.9.** Diagram of the final state of magnetization in the coordinates of the pump-pump delay au and the initial temperature of the sample T, calculated with Eq. 5.5 at fixed dimensionless damping parameter  $\zeta/(2\pi f)=0.1$ .

However, we note that none of the models suggested before took into account the fact that the damping parameter  $\zeta$  in the equation of motion (Eq. 5.5) must also have a strong temperature dependence. The opto-magnetic pulse triggers spin oscillations at the frequency of the quasiferromagnetic mode of the antiferromagnetic resonance in the orthoferrite [7]. This mode is known to "soften" down to zero frequency at temperatures of SRT from  $\Gamma_2$  to  $\Gamma_{24}$ , as well as from  $\Gamma_{24}$  to  $\Gamma_4$ . It is a well-known experimental fact that the softening of magnetic resonances is accompanied by a dramatic increase in damping. This is also the case in our experiment. Indeed, we found the damping peak at  $T_1$  in single-pump experiments (Fig. 5.8), extracting the frequency and damping of the spin oscillations as a function of temperature (Fig. 5.10).

To determine the decay coefficient in the system, we fitted the oscillations from Fig. 5.8 with a damped sine function:

$$\theta(t) = \theta_0 + A\cos(\omega t + \varphi)\exp(-\omega_0 \lambda t),$$
 (5.7)

where  $\omega=\omega_0\sqrt{1-\lambda^2}$  is the frequency,  $\omega_0$  is the natural frequency (i.e. in the absence of damping) and  $\lambda=\zeta/\omega_0$  is the dimensionless decay rate. Using this data, we can more accurately determine the position of  $T_1=215{\rm K}$ .

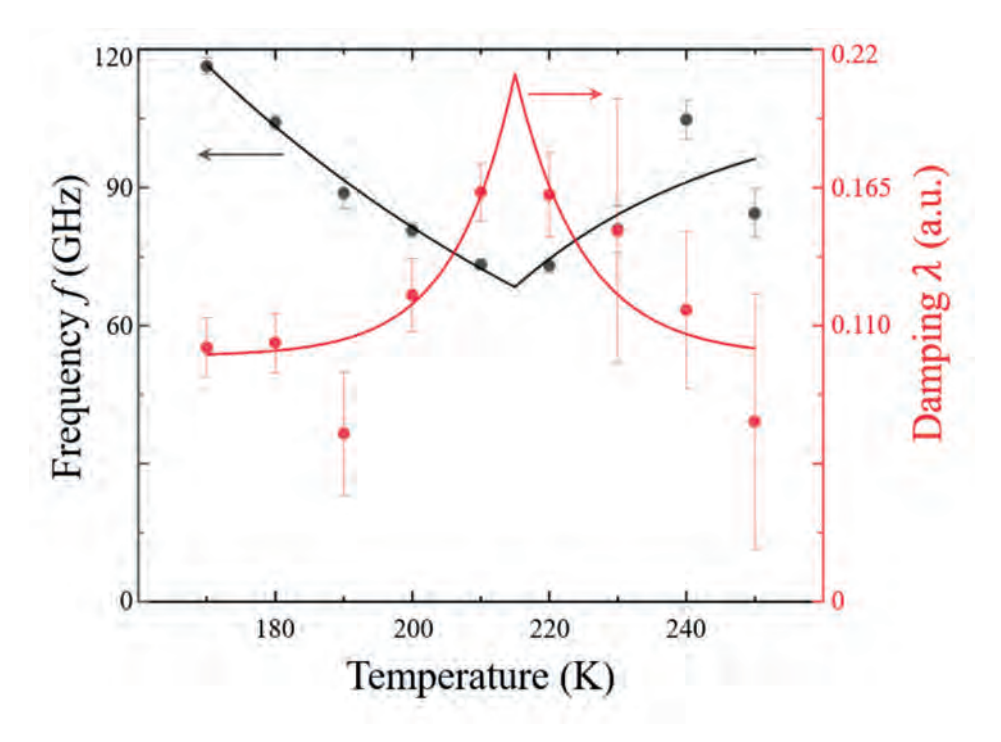


**Fig. 5.10.** Temperature variation of the frequency f and the dimensionless decay rate  $\lambda=\zeta/\left(2\pi f\right)$ , estimated from data on Fig. 5.8. Lines are guides to the eye.

If we add temperature dependence of the damping deduced from Fig. 5.10 to the simulations, the results of the simulations appear to be in a good qualitative agreement with the experiment (Fig. 5.11).

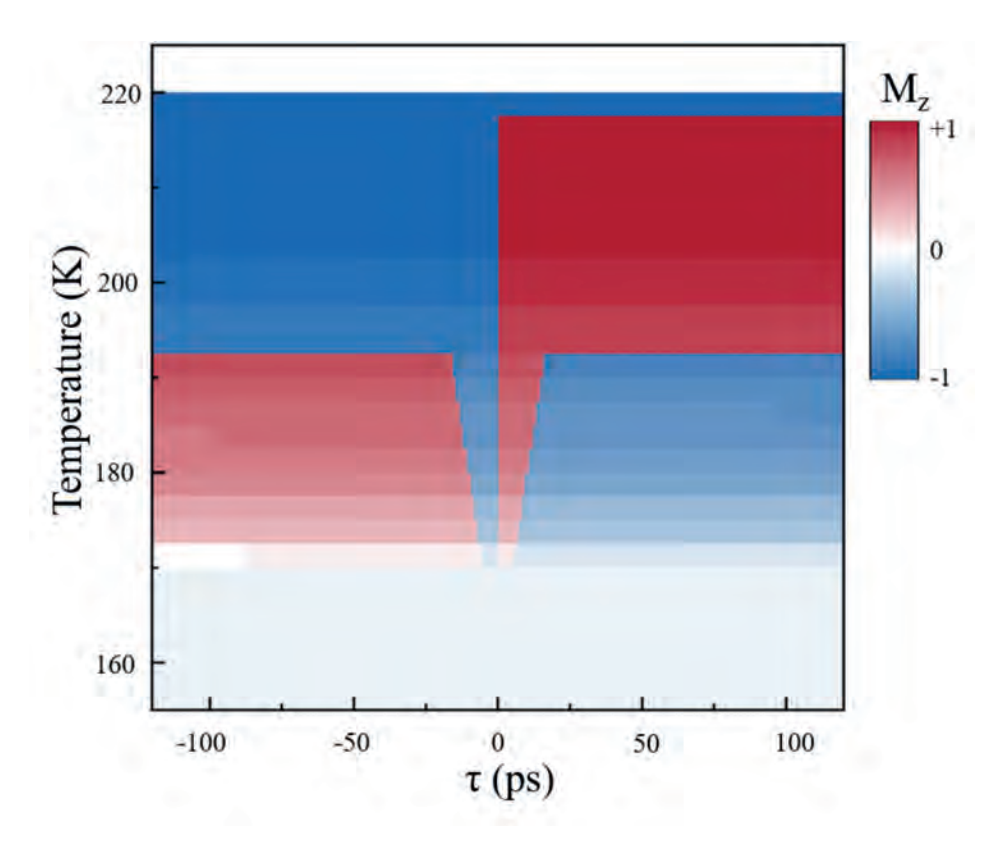


**Fig. 5.11.** The diagram of the final state calculated with Eq. 5.5 with the presence of high damping rate at SRT. The colour code shows the value  $\cos\theta$ , as the experimental scheme is sensitive to out-of-plane component of magnetization and the detected signal is proportional to  $\cos\theta$ .

We would also like to add that, although the energy function (Eq. 5.6) has only two minima in the low-temperature phase  $\Gamma_2$  and two minima in the high-temperature phase  $\Gamma_4$ , in the transition phase  $\Gamma_{24}$ , there are four energy minima and, thus, four possible orientations of the magnetization. These four states can be described as follows: Two minima in the  $\Gamma_2$  phase correspond to  $\varphi_m=\pm\pi/2$ , with potential barriers at  $\varphi_b=0$  and  $\varphi_b=\pi$ . In the  $\Gamma_4$  phase, the minima and maxima of the potential energy are inverted:  $\varphi_m=0$  and  $\varphi_m=\pi$ ;  $\varphi_b=\pm\pi/2$ . In the  $\Gamma_{24}$  phase, there are four potential barriers, while the minima are located at  $\varphi=\varphi_1\left(T\right)$ ;  $-\varphi_1\left(T\right)$ ;  $\pi-\varphi_1\left(T\right)$  and  $\pi+\varphi_1\left(T\right)$ .

When the sample is heated by a laser pulse from the  $\Gamma_2$  phase, potential barriers form in the regions of  $\varphi=\pm\pi/2$ , fixing the magnetization orientation in one of the positions ("up" or "down"). At the same time, the barriers in the regions  $\varphi=0$  and  $\varphi=\pi$  decrease, potentially allowing the magnetization to get transferred from the

state  $\varphi_1\left(T\right)$  to the state  $\pi-\varphi_1\left(T\right)$ . This possibility was also taken into account in the model (Fig. 5.12). The color code now corresponds to the value of the angle  $\varphi$ . Darker areas correspond to the transition through the potential barrier at  $\varphi=0$  or  $\varphi=\pi$ . Such a transition through the potential barrier is possible only within a narrow temperature range when the sample is in the  $\Gamma_{24}$  phase after the impact of two pump pulses. The setup used is sensitive only to  $M_z=\mathrm{Mcos}\varphi$  and does not allow distinguishing between symmetric states such as with

$$arphi>\pi/2$$
 ( $arphi_1=\pi+arphi_0$  and  $arphi_2=\pi-arphi_0$ ).

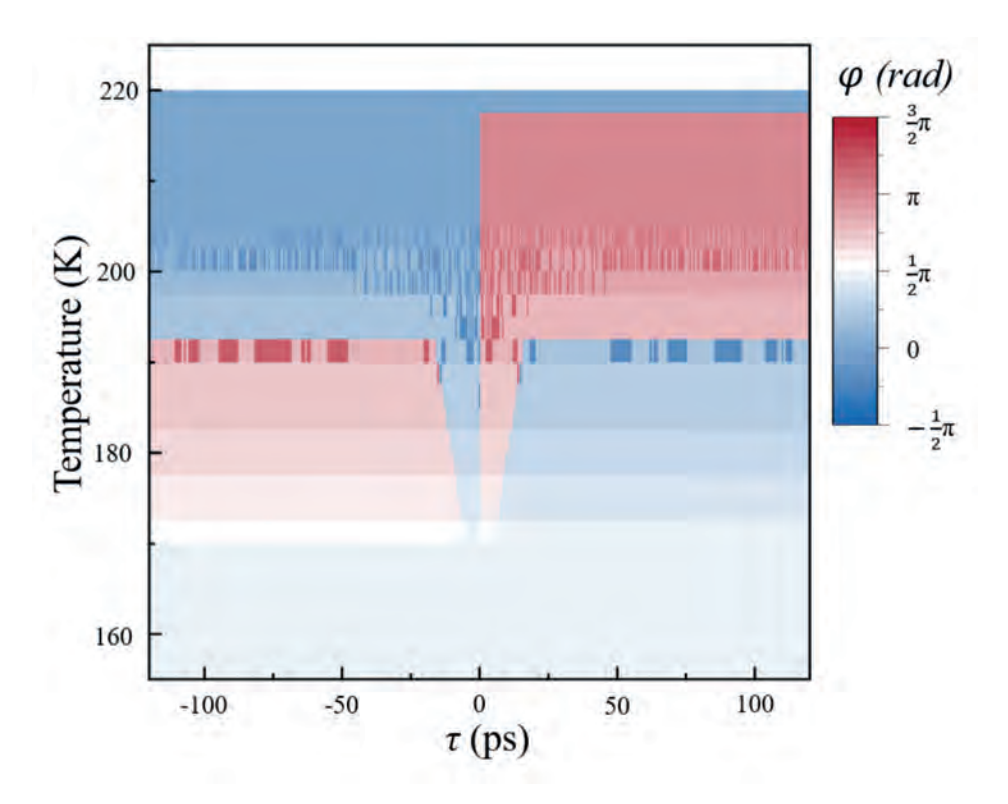


**Fig. 5.12.** The calculated orientation of the magnetization  $\varphi$  as a function of initial temperature T and time delay between two pump pulses  $\tau$ .

Based on the experimental observations (Fig. 5.5) and modeling, we suggest the following path of the reorientation process under double-pump excitation (Fig. 5.13). In the phase  $\Gamma_2$  ( $T < T_1$ ) the equilibrium orientation of  ${\bf M}$  corresponds to  $\varphi_0 = \pm \pi/2$ . To be specific in the illustration, we assume the initial state with  $\varphi_0 = \pi/2$ , and the first-arriving pump with positive helicity  $\sigma^+$  launches the magnetization dynamics through IFE towards  $\varphi > \varphi_0$  (Fig. 5.13, top frame). Subsequently, there are two scenarios for the dynamics determined by  $\tau$ . The first

scenario is realized if the second pump arrives too early, that is,  $\tau$  is smaller than a critical value  $au_{
m cr}$  (Fig. 5.13, left frames). In this scenario, the second pulse cannot reverse the forward motion of the system or accelerate it sufficiently in the backward motion to overcome the potential barrier in phase  $\Gamma_{24}$  before the barrier appears. Thus, the second pump will further heat the sample and thus help further establish the state determined by the helicity of the first pump if  $au < au_{
m cr}$ . The second scenario occurs if  $au > au_{
m cr}$ , that is, the second pump arrives when the system has reversed its momentum and passed a critical coordinate  $arphi_{
m cr}$  in backward motion (Fig. 5.13, right frames). In this scenario, the torque of the second pulse is sufficient to transfer the system to  $\varphi < \varphi_0$  before the potential barrier appears in  $\Gamma_{24}$ . We notice that the same scenarios work for the initial combination of  $\sigma^+$  and  $arphi_0=-\pi/2$ , since the torque induced by IFE does not change sign with the sign of  $\varphi_0$  [21,22]. Thus, the helicity of  $\sigma^+$  works the same

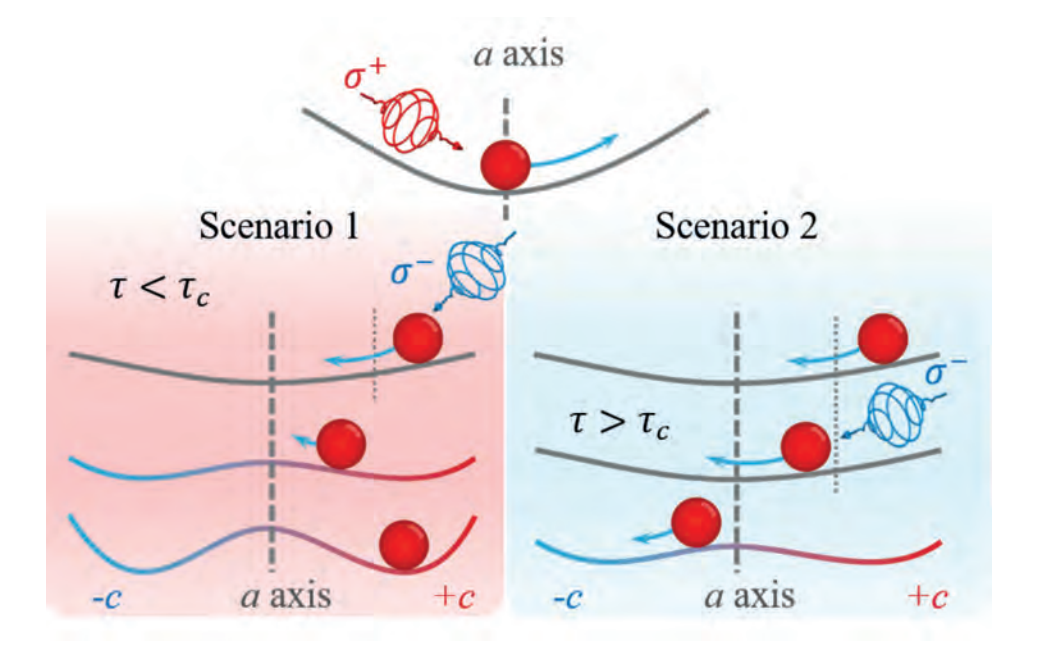
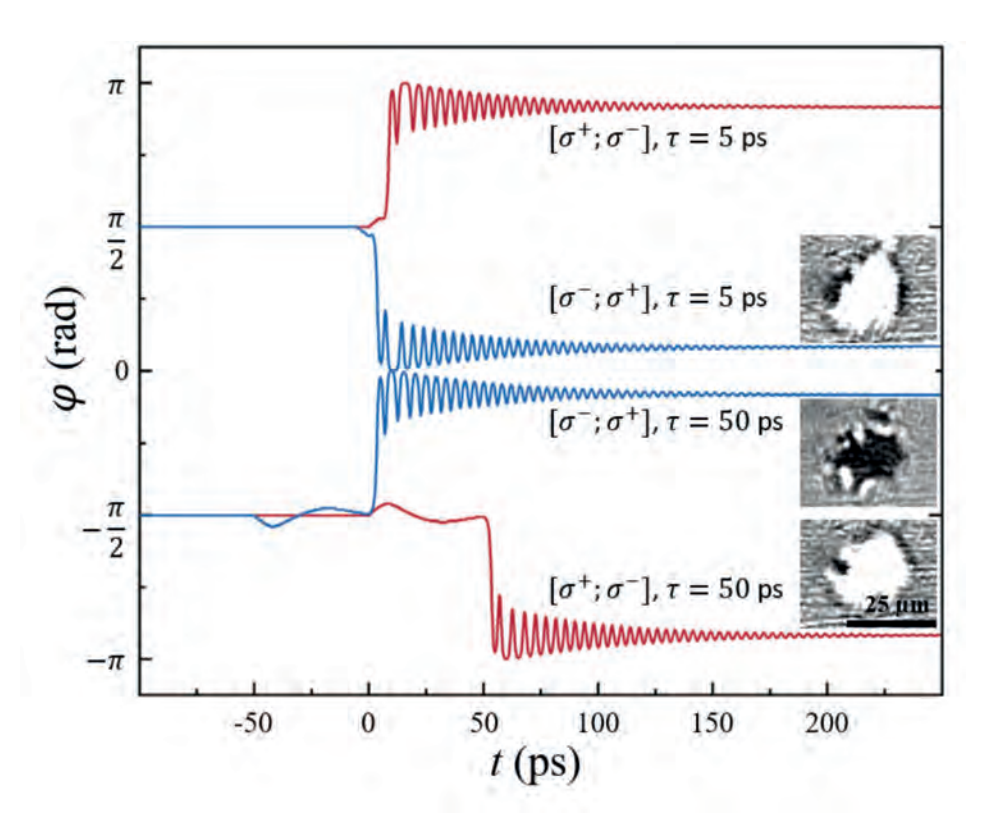


Fig. 5.13. Two scenarios of the coherent magnetization control under double-pump excitation. The final state is defined by pump's helicities and pump-pump delay time  $\tau$ . A detailed description is in the text.

way for both initial orientations of the domains in  $\Gamma_2$ . The change in helicity sign flips the initial torque and the corresponding final state, resulting in a symmetric  $T-\tau$  diagram with respect to  $\tau=0$ .

The validity of the model is further confirmed by theoretically calculated spin dynamics (Fig. 5.14). For T = 190 K,  $\tau$  = 15 ps (upper part of the figure) and 50 ps (lower part of the figure) the dynamics were calculated for the cases when the polarization of the first incoming pulse was  $\sigma^+$  (red) and for  $\sigma^-$  (blue). The initial magnetization direction in the plane of the sample was at  $\varphi=\pi/2$  or  $\varphi=-\pi/2$ . It is seen that the first pulse induces slow spin precession corresponding to the soft mode. The initial phase of the oscillations depends on the polarization of the pulse, which agrees well with the experiment (Fig. 5.8).

Inset of Fig. 5.14 shows images obtained from the CCD camera at the specified temperature and time between the pulses. Comparison of the experimental images and the theory further demonstrate a good agreement and thus supports the validity of the model.



**Fig. 5.14.** Calculated spin dynamics  $\varphi$  for different pulse-to-pulse  $\tau$  at T = 190 K. The color represents the helicity of the first arriving pulse (red for  $\sigma^+$  and blue for  $\sigma^-$ ). The same color code was used on previous graphs and diagrams. Insets show the images obtained with a CCD camera at the same  $\tau$  T and pump polarizations.

#### 5.6 Conclusions

We experimentally and numerically studied coherent control of ultrafast phase transition in antiferromagnetic rare-earth orthoferrite using double-pulse excitation. We show that the final state, formed at 1.5 ns after pump excitation, depends on the time delay between the pump pulses. At a temperature close to the phase transition, the final state is fully defined by the helicity of the earliest pump pulse. At lower temperatures, we distinguish two regions. In particular, we show that at delays larger than a critical time, the state is defined by the helicity of the latest pulse, while at shorter delays, it is the earliest pulse in the pair that defines the final magnetization. We show that earlier published models are unable to reproduce the experimental results and suggest that the reason for the discrepancy is the neglected temperature dependence of the damping. Finally, we note that the peak-like behavior of damping at SRT temperature is more general and inherent to other kinds of phase transitions, where the softening of the corresponding mode appears. Among the examples, one can mention a similar behavior at the Néel temperature [23-25], Morin transition [26] and spin-flop transition [27] of antiferromagnets.

### Literature

- L. D. Landau, A possible explanation of the field dependence of the susceptibility at low temperatures, Phys. Z. Sowjet 4, 675 (1933).
- L. Néel, Propriétés magnétiques des ferrites; ferrimagnétisme et antiferromagnétisme, Annales de physique, pp. 137--198, (1948).
- [3] T. Jungwirth, X. Marti, P. Wadley, and J. Wunderlich, Antiferromagnetic spintronics, Nature nanotechnology 11 (3), 231-241 (2016).
- [4] C. Song, Y. You, X. Chen, X. Zhou, Y. Wang, and F. Pan, How to manipulate magnetic states of antiferromagnets, Nanotechnology 29 (11), 112001 (2018).
- H. Wijn, Y. Endoh, K. Kakurai, A. Katori, M. Seehra, and G. Srinivasan, Perovskites II, Oxides with Corundum, Ilmenite and Amorphous Structures, (1994).
- [6] A. Kimel, A. Kirilyuk, A. Tsvetkov, R. Pisarev, and T. Rasing, Laser-induced ultrafast spin reorientation in the antiferromagnet TmFeO3, Nature 429 (6994), 850-853 (2004).
- [7] A. Kimel, A. Kirilyuk, P. Usachev, R. Pisarev, A. Balbashov, and T. Rasing, Ultrafast non-thermal control of magnetization by instantaneous photomagnetic pulses, Nature 435 (7042), 655-657 (2005).
- [8] A. Kimel, B. Ivanov, R. Pisarev, P. Usachev, A. Kirilyuk, and T. Rasing, Inertia-driven spin switching in antiferromagnets, Nature Physics 5 (10), 727-731 (2009).
- J. De Jong, I. Razdolski, A. Kalashnikova, R. Pisarev, A. Balbashov, A. Kirilyuk, T. Rasing, and A. Kimel, Coherent Control of the Route of an Ultrafast Magnetic Phase Transition via Low-Amplitude Spin Precession, Physical Review Letters 108 (15), 157601 (2012).
- [10] T. Kurihara, H. Watanabe, M. Nakajima, S. Karube, K. Oto, Y. Otani, and T. Suemoto, Macroscopic magnetization control by symmetry breaking of photoinduced spin reorientation with intense terahertz magnetic near field, Physical Review Letters 120 (10), 107202 (2018).
- [11] A. Balbashov and S. Egorov, Apparatus for growth of single crystals of oxide compounds by floating zone melting with radiation heating, Journal of Crystal Growth 52, 498-504 (1981).
- [12] H. Horner and C. Varma, Nature of spin-reorientation transitions, Physical Review Letters 20 (16), 845 (1968).
- [13] Y. Hashimoto et al., Ultrafast time-resolved magneto-optical imaging of all-optical switching in GdFeCo with femtosecond time-resolution and a µm spatial-resolution, Review of Scientific Instruments 85 (6) (2014).
- [14] J. De Jong, A. Kalashnikova, R. Pisarev, A. Balbashov, A. Kimel, A. Kirilyuk, and T. Rasing, Effect of laser pulse propagation on ultrafast magnetization dynamics in a birefringent medium, Journal of Physics: Condensed Matter 29 (16), 164004 (2017).
- [15] A. Zvezdin, Dynamics of domain walls in weak ferromagnets, ZhETF Pisma Redaktsiiu 29, 605 (1979).
- [16] V. G. Bar'yakhtar, B. A. Ivanov, and M. V. Chetkin, Dynamics of domain walls in weak ferromagnets, Soviet Physics Uspekhi 28 (7), 563 (1985).

- [17] B. Ivanov, Spin dynamics of antiferromagnets under action of femtosecond laser pulses, Low Temperature Physics 40 (2), 91-105 (2014).
- [18] A. Kirilyuk, A. V. Kimel, and T. Rasing, Ultrafast optical manipulation of magnetic order, Reviews of Modern Physics 82 (3), 2731-2784 (2010).
- [19] L. Le Guyader, A. Kleibert, F. Nolting, L. Joly, P. Derlet, R. Pisarev, A. Kirilyuk, T. Rasing, and A. Kimel, Dynamics of laser-induced spin reorientation in Co/SmFeO 3 heterostructure, Physical Review B—Condensed Matter and Materials Physics 87 (5), 054437 (2013).
- [20] J. De Jong, A. Kimel, R. Pisarev, A. Kirilyuk, and T. Rasing, Laser-induced ultrafast spin dynamics in ErFeO 3, Physical Review B 84 (10), 104421 (2011).
- [21] F. Hansteen, A. Kimel, A. Kirilyuk, and T. Rasing, Nonthermal ultrafast optical control of the magnetization in garnet films, Physical Review B 73 (1), 014421 (2006).
- [22] L. Shelukhin, V. Pavlov, P. Usachev, P. Y. Shamray, R. Pisarev, and A. Kalashnikova, Ultrafast laser-induced changes of the magnetic anisotropy in a low-symmetry iron garnet film, Physical Review B 97 (1), 014422 (2018).
- [23] D. Bossini, S. Dal Conte, Y. Hashimoto, A. Secchi, R. V. Pisarev, T. Rasing, G. Cerullo, and A. V. Kimel, Macrospin dynamics in antiferromagnets triggered by sub-20 femtosecond injection of nanomagnons, Nature communications 7 (1), 10645 (2016).
- [24] D. Afanasiev et al., Controlling the anisotropy of a van der Waals antiferromagnet with light, Science advances 7 (23), eabf3096 (2021).
- [25] X.-X. Zhang, S. Jiang, J. Lee, C. Lee, K. F. Mak, and J. Shan, Spin dynamics slowdown near the antiferromagnetic critical point in atomically thin FePS3, Nano Letters 21 (12), 5045-5052 (2021).
- [26] R. Lebrun et al., Long-distance spin-transport across the Morin phase transition up to room temperature in ultra-low damping single crystals of the antiferromagnet α-Fe2O3, Nature communications 11 (1), 6332 (2020).
- [27] S. Sorokin et al., Magnetization dynamics in synthetic antiferromagnets: Role of dynamical energy and mutual spin pumping, Physical Review B 101 (14), 144410 (2020).

### CHAPTER 6

# All polarization dependence of all-optical control on magnetization reorientation in (SmTb)FeO<sub>3</sub>

Building upon the results of Chapter 5, where we demonstrated ultrafast double-pulse control of spin-reorientation dynamics in the antiferromagnetic orthoferrite (Sm,Tb)FeO<sub>3</sub>, this chapter explores the role of light polarization in the all-optical control of magnetization reorientation. While Chapter 5 focused on circularly polarized pulses to initiate and control the spin-reorientation transition, here we use linearly polarized pulses to decouple the thermal and opto-magnetic contributions. In this approach, a linearly polarized pulse provides ultrafast heating, whereas a weaker circularly polarized pulse introduces a directional stimulus via the inverse Faraday effect. This configuration allows us to investigate the interplay of heating and effective magnetic field in driving spin dynamics.

Our findings reveal that the response of the system to two successive polarized pulses is highly nontrivial, often violating the expected principle of superposition. This chapter addresses key questions raised previously and highlights the nonlinear and polarization-sensitive nature of ultrafast spin manipulation in orthoferrites.

#### 6.1 Motivation

The effects of light on a magnetic medium can be categorized as polarizationdependent and polarization-independent. The latter are predominantly effects originating from laser induced heating i.e. thermal effects. The study of polarization-dependent effects, along with the advent of modern femtosecond laser systems, enabled the first observation of all-optical helicity-dependent switching [1-5]. In the earlier studies, it was believed that a transfer of angular momentum or the inverse Faraday effect (IFE) [6,7] plays a decisive role in this phenomenon. The switching was eventually explained by ultrafast laser-induced heating combined with magnetic circular dichroism (MCD) [8-10]. MCD is associated with the different absorption of circularly polarized light by magnetic domains with the magnetizations parallel and antiparallel with respect to the wavevector of the light. In this case, a temperature gradient, for instance, can be created across a domain wall, shifting the latter towards the higher temperature [11]. In ferromagnetic samples, switching is only possible with multiple pulses [12]; the first pulse demagnetizes the sample, creating a multi-domain state, and subsequent pulses shift the domain walls to form a new magnetic domain. If IFE can play a role in this process is still a subject of debate [13,14].

Magnetic dynamics can also be triggered by linearly polarized light, which does not carry any angular momentum. In this case, the effect is explained in terms of the inverse Cotton-Mouton effect (ICME) [15-17]. The impulsive action of linearly polarized light on a spin system can be viewed as the emergence of induced magnetic anisotropy in the sample. In a few studies, it has been shown that the amplitude and the phase of the laser-induced spin oscillations vary depending on the orientation of the linear polarization [15,16].

Apart from effects that depend on the polarization, thermal effects should also be considered. For example, an impact of an ultrafast laser pulse on a magnet through heating can lead to demagnetization [18] or changes in the optical properties [19,20]. There are also studies indicating a possibility of switching in GdFeCo irrespective of the polarization of the laser pulse or the magnetization of the sample [21,22]. At the same time, in many studies in ultrafast laser-induced magnetism, light absorption is often explicitly or implicitly ignored [9,23-26]. These effects have been taken into account relatively recently [27]. Refs [6,28] describe that heating is an important part of the switching process.

This chapter serves as a conceptual continuation of Chapter 5. Previously, we focused on the helicity-dependent effects of circularly polarized light on a magnet. Here, we extend our investigation to explore the full dependence of the final state in the spin-reorientation phase transition (SRT) on the pump pulse polarization. Our goal was to assess whether the helicity-independent (thermal) and helicitydependent (nonthermal) effects of the pump could be separated. A circularly polarized pulse heats the sample as well as acts as an effective magnetic field, launching spin precession. Whereas a linearly polarized pulse with a proper orientation of the polarization would only heat the magnet. Moreover, by changing the polarization angle of the second pulse, we could tune the amplitude of the spin dynamics without altering the overall sample heating.

In addition, this chapter considers similar experiments with elliptically polarized laser pulses. Although most experiments avoid arbitrary polarization geometries due to the added complexity in setup and data interpretation [29], recent work has started exploring the effects of elliptically polarized light on magnets [30]. In the present study, we employed elliptically polarized pulses to determine the threshold helicity at which the final state of the magnetization can be fully controlled with the magnetization in the laser exposed area oriented homogeneously either "up" or "down".

This chapter is divided into several sections. Section 6.2 describes the measurement techniques employed and explains how linearly and elliptically polarized light is characterized. Section 6.3 investigates the spin dynamics under the influence of a single linearly polarized pulse. In Sections 6.4-6.6, the control of the SRT using a combination of linearly and circularly polarized pumps is discussed. Section 6.7 examines the evolution of this transition as a function of the time delay between pump pulses. Sections 6.8 and 6.9 focus on the influence of the polarization orientation and the ellipticity of one of the pump pulses, respectively. Finally, **Section 6.10** presents the possibility of utilizing circular and elliptical pump pulses to achieve a nonlinear combination of the final state of the system.

#### 6.2 Measurement methods

In this chapter, we studied the control of the spin-reorientation transition in the rare-earth orthoferrite (SmTb)FeO<sub>3</sub> also investigated in Chapter 5. The same double-pump setup was used to monitor magnetization in the sample. Magnetization measurements were conducted via the Faraday effect using a balanced detector or a CCD camera. This setup is sensitive only to the out-of-plane component of magnetization,  $M_z$ .

However, the pump channel was modified to allow control over the polarization of one of the pump pulses, while the second pulse had a fixed circular polarization.

Polarization control was achieved using either a half-wave or a quarter-wave plate, matched to the pump wavelength (800 nm). The polarization of the light incident on the wave plate was fixed as linear p-polarization.

Thus, the sample was pumped using the following polarization types (Fig. 6.1): elliptical, and circular. To systematically analyze the obtained measurements, we define the parameters of these polarization states:

- Linearly polarized light ( $\pi$  pulse) corresponds to a fixed orientation of the electric field vector  ${f E}$  (Fig. 6.1(a)). Therefore, it is characterized by the polarization angle  $\beta$ . For instance,  $\beta=0^{\circ}$  corresponds to the p-polarized light, while  $\beta = 90^{\circ}$  corresponds to the s-polarized light.
- Elliptically polarized light ( $\epsilon$  pulse) describes an ellipse traced by the electric field vector  $\mathbf{E}$  (Fig. 6.1(b)). It is characterized by the ellipticity degree, defined as  $\epsilon = \tan \arcsin b/a$ , where b and a denote the minor and major axes of the polarization ellipse, respectively. Another parameter, similar to linear polarization, is the angle  $\beta$ . In this case,  $\beta$  is measured relative to the major axis of the polarization ellipse. Notably, rotating the quarter-wave plate changes both the ellipticity and the angle  $\beta$ . Since these two parameters are intrinsically linked, in this chapter, we will use only the ellipticity parameter  $\epsilon$ . The case  $\epsilon = 0$  corresponds to linear polarization.
- The maximum value of ellipticity,  $\epsilon_{\max}=\pm 1$ , corresponds to circular polarization ( $\sigma$  - pulse) (Fig. 6.1(c)). In this case, the angle  $\beta$  is no longer meaningful, and only the helicity remains, determining the direction in which E traces a circle.

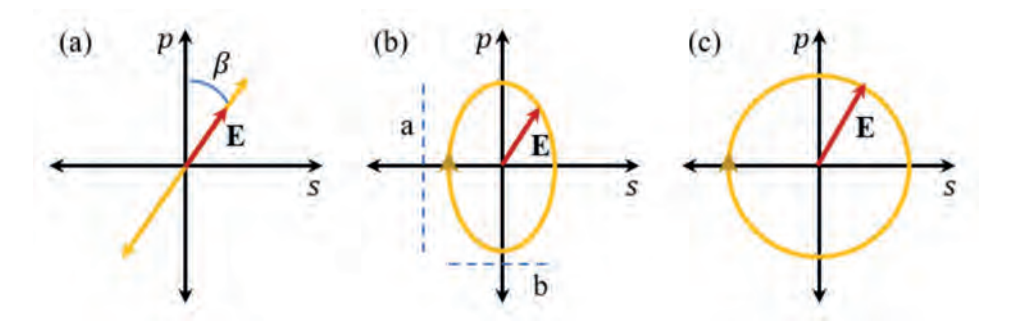
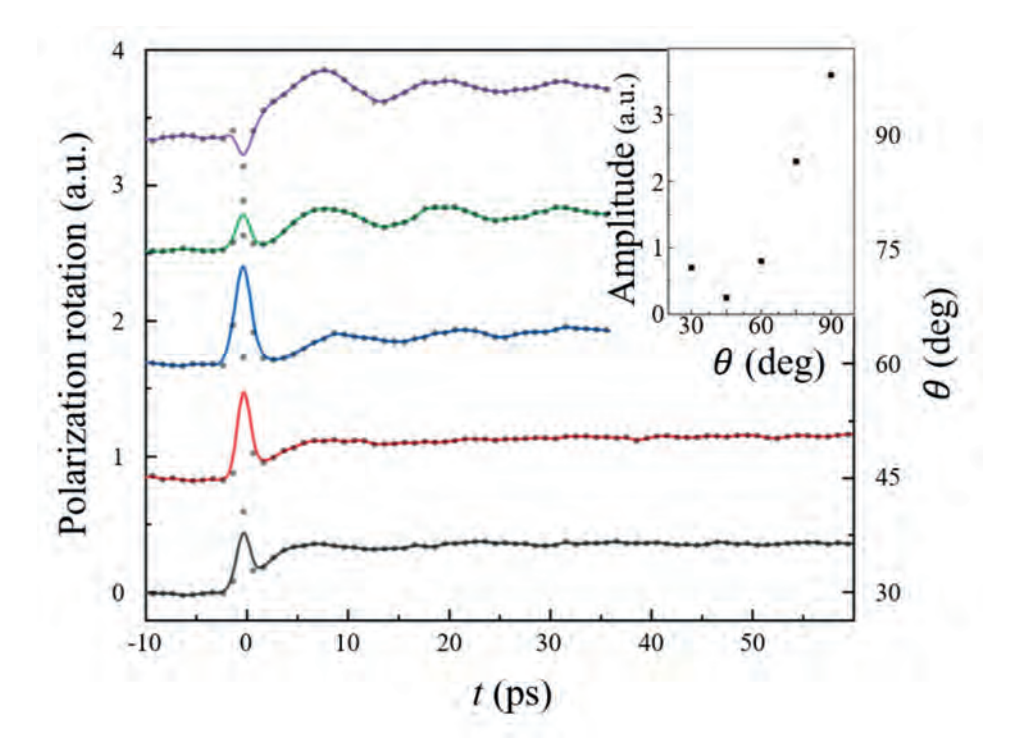


Fig. 6.1 . Schematics of light polarization. (a) linearly polarized, (b) elliptically polarized, (c) circularly polarized light.

## 6.3 Spin dynamics triggered by a single linear polarized pump pulse

Initially, experiments were conducted using a single linearly polarized pump pulse the power of which was an order of magnitude lower than the one necessary to form a photo-induced domain (see Chapter 5). The lower-power approach was employed to investigate the possibility of distinguishing the magnetic signal from temperature-related effects caused by laser heating. The setup utilized a balanced photodetector and a single linearly polarized pump pulse. The pump polarization orientation  $(\beta)$  was controlled by rotating a half-wave plate. The temporal evolution of the probe polarization rotation is shown in Fig. 6.2, where each curve corresponds to a specific pump polarization angle,  $\beta$ .

Changes in polarization rotation could be attributed to optical or magnetic effects. As demonstrated in the previous studies [19,20], a step-like change in the signal is generally linked to variations in the sample's overall optical properties rather than to its magnetic characteristics. Oscillations are most noticeable under s-polarization ( $\beta=90^\circ$ ) conditions of the pump. The oscillation frequency coincides with that in Chapter 5 triggered by circularly polarized pump pulses. As established in Chapter 5, the oscillation phase is contingent upon the orientation of the external magnetic field, implying its magnetic origin — namely, laser-induced magnetization precession. Consequently, a pump polarization of  $eta=45^\circ$  was identified, at which the oscillation amplitude falls almost below the sensitivity threshold of the setup, indicating minimal magnetic influence on the system (Fig. 6.2, inset). Subsequent experiments are anticipated to utilize this particular pump pulse orientation in dual pumping configurations to decouple thermal and magnetic effects on the system (domain formation).



**Fig. 6.2.** Magnetization dynamics in (Sm,Tb)FeO $_3$  induced by a linearly polarized pump pulse with different polarization orientations. The polarization angle  $\beta$  is indicated on the right y-axis:  $\beta=0^\circ$  corresponds to  $\pi$ -polarization and  $\beta=90^\circ$  to s-polarization. Symbols represent experimental data; solid lines show the fit. The inset displays the dependence of the oscillations' amplitude on  $\beta$ .

Next, a single-shot experiment employing a CCD camera was conducted, as illustrated in Figure 6.3. Individual pulses with linear polarization ( $\beta=45^\circ$  and  $\beta=0^\circ$ ) as well as circular polarization ( $\sigma^-$  and  $\sigma^+$ ) were used. The gray color corresponds to the sample's initial state. As the sample is initially at  $T=170{\rm K} < T_1$ , it is in the  $\Gamma_2$  phase, and the magnetization  ${\bf M}$  is aligned in the sample plane. As the setup is sensitive only to the out-of-plane  $M_z$  component, the total magnetic signal is zero. The black and white colors signify the presence of magnetization oriented along  $M_z>0$  or  $M_z<0$  with respect to the wave vector of the probe beam. These images were recorded at the probe delay of t=1.5 ns, significantly longer than the characteristic timescale of the magnetization dynamics, ensuring that the spin system had reached a metastable state. The presence of visible domains indicates that the sample is at least in the  $\Gamma_{24}$  phase  $(T>210{\rm K})$ .

Although no magnetic oscillations were observed in the stroboscopic data (Fig. 6.2), a stable magnetically ordered domain still formed under the linearly

polarized pump with  $\beta=45^{\circ}.$  The magnetization direction in the illuminated region varied for  $\beta=0^{\circ}$  (i.e.  $\pi$ -polarized). Small inclusions or defects in the formed pattern presumably originate from inhomogeneities in the sample. A similar effect was also observed under circularly polarized pumping, although it was less pronounced, likely because the domain size is smaller in that case.

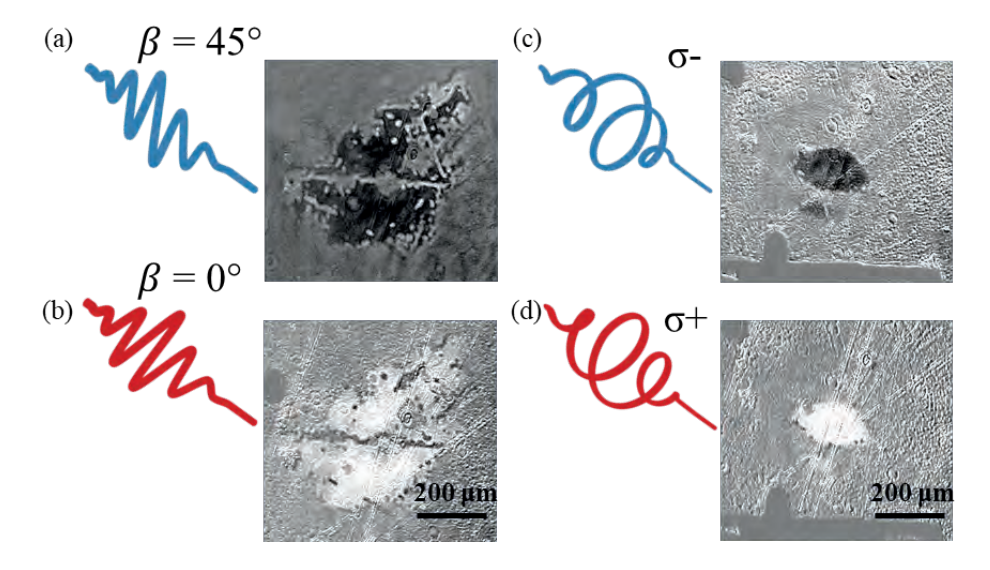


Fig. 6.3. CCD images acquired at t=1.5 s after excitation with a single linearly (a,b) and circularly polarized (c,d) pump. The initial sample temperature was 170 K, and the pump fluence was 165 mJ/ cm<sup>2</sup>.

Despite the minimal observed magnetic dynamics at  $\beta=45^\circ$ , a single, uniform magnetic domain is nonetheless formed (Fig. 6.3(a)). Several factors may account for this. First, the setup may have imperfect sensitivity to small changes in  $M_z$ . Even a weak influence on  $M_z$  could initiate spin dynamics, especially since raising the sample temperature and causing a transition to the  $\Gamma_{24}$  phase makes the inplane orientation unstable and thus must result in spin dynamics. Second, there may be a slight miscut of the crystal so that its crystallographic axes are not exactly in the sample plane. Although the cut was nominally along the c-axis, the real sample may deviate from an ideal c-cut, causing the in-plane spin dynamics to have a component out of the crystal plane. Both factors likely contributed to the observed results in this experiment.

## 6.4 Spin dynamics triggered by circular and linear polarized pumps

Having examined how linear polarization affects the final magnetic state during the SRT, the next step was to investigate the combined effect of a  $\pi$  – pulse (oriented at  $\beta=45^{\circ}$ ) and a  $\sigma$  - pulse ( $\sigma^+$  helicity). When sufficiently intense, each pulse alone can generate a domain with opposite magnetization, thus enabling control of the critical delay  $au_{
m cr}$ , beyond which the system becomes insensitive to a second pump pulse.

Figure 6.4(a) presents a diagram of the final magnetic state as a function of the delay between the two pump pulses,  $\tau_{\rm DD}$ , and the sample temperature T. Here and henceforth, a  $\sigma$  – pulse arrives first for  $\tau_{\rm pp}<0,$  and a  $\pi$  – pulse arrives first for  $au_{
m pp}>0$ . The labels for magnetization are chosen such that  $M_z=+1$  corresponds to white domains and  $M_z=-1$  to black domains. Note that  $M_z=0$  can imply either zero net change in the probe polarization or the presence of a multidomain state.

From this diagram, one can infer that at high temperatures  $T>T_1=215\mathrm{K}$ , the system already exhibits a nonzero out-of-plane magnetization  $(M_z / 0)$  and is divided into magnetic domains with opposite  $M_z$ . Since the sizes of these domains are much smaller than the probe spot, the total polarization rotation is zero. The effect imparted by the two pump pulses is insufficient to create a magnetic domain. Further heating moves the system toward the second transition temperature  $T_2$ , where the magnetization aligns predominantly along the z-axis  $(M_z = |\mathbf{M}|)$ . Conversely, at lower temperatures  $T \leq 170 \mathrm{K}$ , the combined heating from the two pulses does not push the system above the SRT; the magnetization remains in-plane ( $M_z = 0$ ) and thus remains undetectable with our setup.

At intermediate temperatures, a well-defined magnetization state emerges. Near  $T_1$ (specifically  $200 \mathrm{K} \leq T \leq 215 \mathrm{K}$ ), the final state depends only on whether the circularly or linearly polarized pulse arrives first. Despite the difference in pulse powers and the amplitude of the induced oscillations, once the first pulse has acted, the second cannot switch the system to another state. At slightly lower temperatures ( $170 {
m K} < T < 200 {
m K}$ ), the diagram becomes asymmetric. When  $au_{
m pp} < 0$  (the  $\sigma$  – pulse arrives first), the  $\sigma$  – pulse always determines the final state, regardless of when the second pump pulse arrives. However, for  $au_{
m pp}>0$  (the  $\pi$  - pulse arrives first), the delay  $au_{
m pp}$  becomes crucial. If  $au_{
m pp} < au_{
m cr}$ , the system remains insensitive to the second pulse, and the final state is determined by the  $\pi$  – pulse. In contrast, when  $au_{
m pp} > au_{
m cr}$  , the later-arriving  $\sigma$  – pulse ultimately dictates the final magnetization state (in agreement with the images in Fig. 6.4(c).

Figure 6.4(b) presents a diagram of the magnetization's final state for two  $\sigma$  – pulses at a similar fluence (67 mJ/cm<sup>2</sup>), as described in Chapter 5 (Fig. 5.6). While at high temperatures ( $T \geq 200$  K) the diagrams coincide, differences are observed in the regions where the  $au_{\rm cr}$  effect is present ( $180 \le T < 200$  K). When two  $\sigma$  pulses of different helicities have the same fluence, it does not matter which pulse arrives first - the second pulse can switch the system to a state with opposite magnetization if  $au_{\rm pp} > au_{\rm cr}$ .

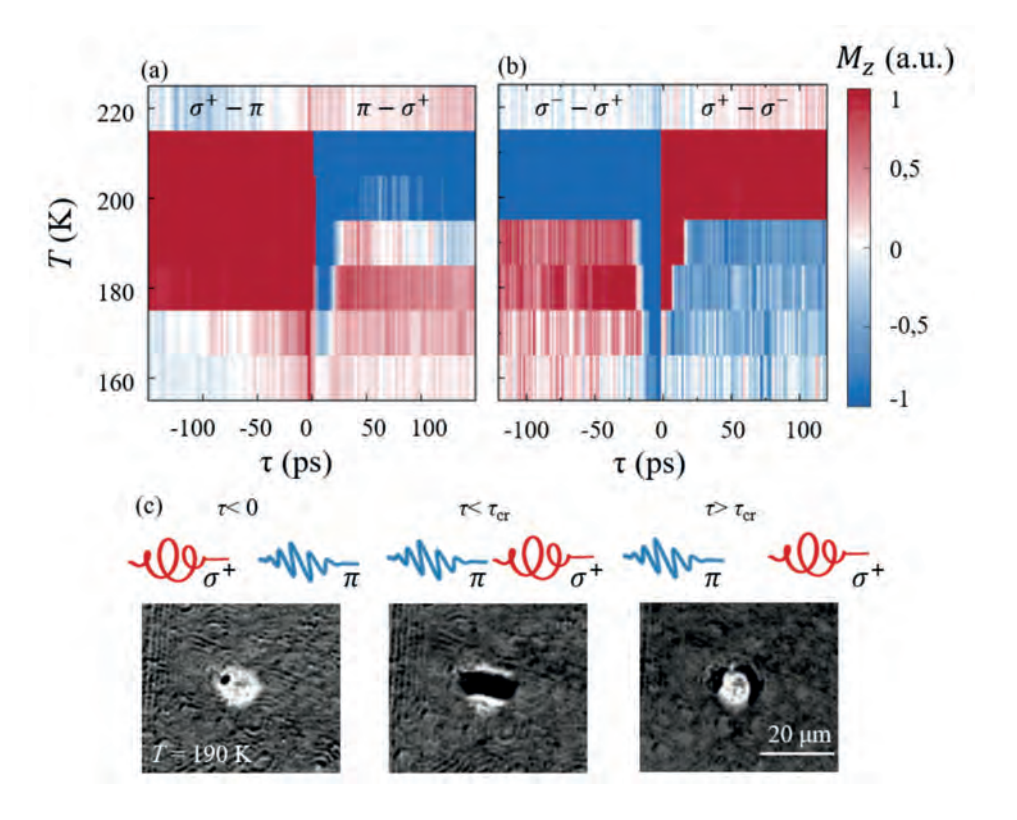
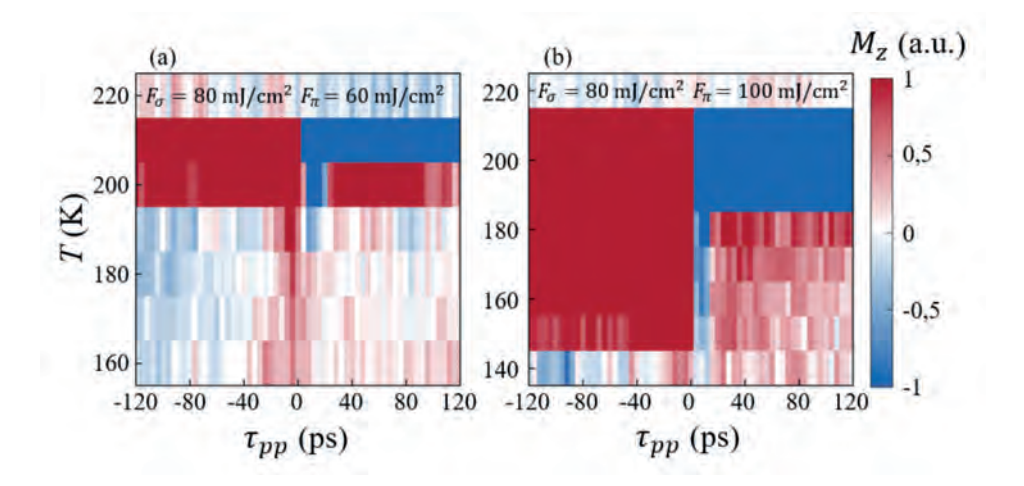


Fig. 6.4. (a) Experimental diagram of the magnetization final state in coordinates of pump-pump delay  $au_{pp}$  and initial temperature of the sample T.  $\sigma$  – pulse arrives first for  $au_{pp} < 0$ ,  $\pi$  – pulse arrives first for  $au_{pp}>0$ . The fluence of both pumps was approximately equal to 80 mJ/cm $^2$ . (b) Experimental diagram for two circular polarized pumps (from Chapter 5). (c) Images of the reorientation process at t=1.5 ns and different  $au_{pp}$  observed with CCD camera at T = 190 K.

Next, we explored the possibility of modifying  $au_{
m cr}$  by using either stronger or weaker linearly polarized pulses. To this end, we varied the power of the linearly polarized pulse, and the resulting diagrams are depicted in Fig. 6.5. Even when the power of the  $\pi$  – pulse is reduced (see Fig. 6.5(a)), there remains a temperature region near  $T_1$  in which the first pulse fully determines the final state for delays  $\tau_{\rm pp} < \tau_{\rm cr}$ . Likewise, whether we increase or decrease the power of the  $\pi$  – pulse, the overall diagram preserves the same asymmetry for  $T < T_1$ , provided T is high enough for the system to undergo the first SRT. Specifically, the circularly polarized pulse still dominates, fixing the final state for both  $\tau_{\rm pp} < 0$  and  $\tau_{\rm pp} > \tau_{\rm cr}$ . These diagrams resemble that in Fig. 6.4(a). Two main regions are also preserved: a high-temperature region, where the second pulse cannot affect the system, and a low-temperature region, where the second pulse can change the final magnetization direction after  $\tau_{\rm cr}$ .



**Fig. 6.5.** Experimental diagram of the magnetization final state in coordinates of pump-pump delay  $\tau_{pp}$  and initial temperature of the sample similar to those in Fig. 6.4(a), but measured at different pulse fluences. The fluence of the  $\sigma$  – pulse (arrives first for  $\tau<0$ ) was fixed at 80 mJ/cm². Fluence of the  $\pi$  – pulse was (a) 60 mJ/cm² and (b) 100 mJ/cm².

To quantify their similarity, Fig. 6.6(a) shows the dependence of the final magnetization  $M_z$  on the pump-pump delay  $\tau_{\rm pp}$  at the highest temperature where  $\tau_{\rm cr}$  appears. The fluence of the  $\sigma$  – pulse was fixed at 80 mJ/cm². The  $\pi$  – pulse had fluences of 60 mJ/cm² (blue), 80 mJ/cm² (red) and 100 mJ/cm² (black), corresponding to temperature thresholds of 200 K, 180 K and 150 K, respectively. Overlaying these curves reveals that  $\tau_{\rm cr}$  remains unchanged, irrespective of  $\pi$  – pulse fluence. Finally, Fig. 6.6(b) shows that the minimum temperature above which  $\tau_{\rm cr}$  vanishes also remains the same for all studied fluence levels.

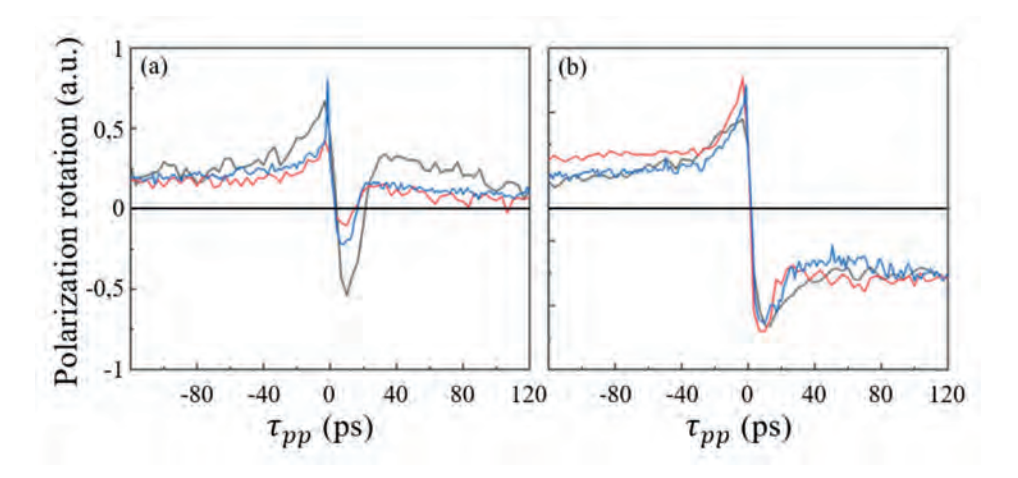


**Fig. 6.6.** Combination of low temperature (a) and high temperature (b) slices of the diagrams in Fig. 6.5. These graphs are used to emphasise that all the diagrams are similar and can be overlapped with the temperature shift. Blue color corresponds  $F_2$ = 60 mJ/cm², red color  $F_2$  = 80 mJ/cm², black color  $F_2$  = 100 mJ/cm². The temperatures chosen are explained in the text.

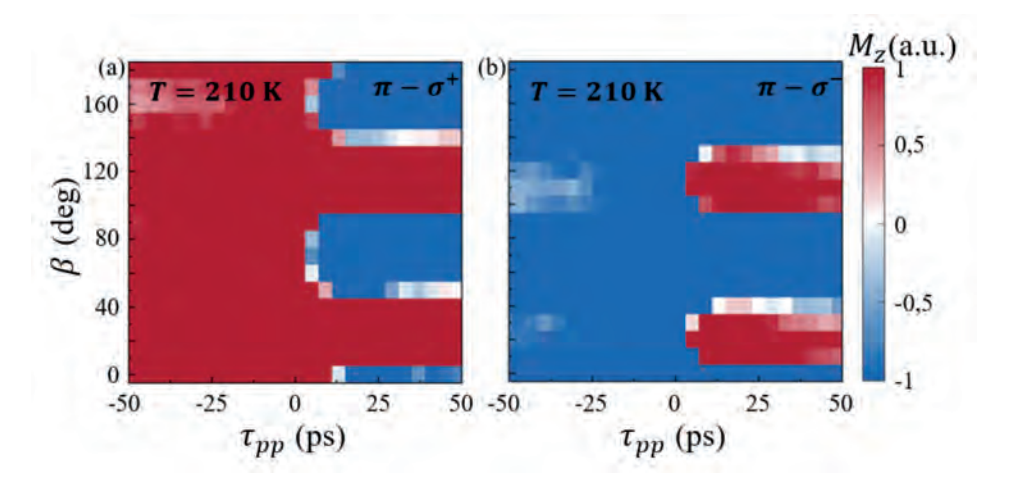


**Fig. 6.7.** Experimental diagram of the magnetization final state in coordinates of pump-pump delay  $\tau_{\rm pp}$  and orientation of the linearly polarized light  $\beta$ . The final magnetization state for double-pump experiment with a single  $\sigma$  – pulse and a single  $\pi$  – pulse. The initial sample temperature was T=210 . The  $\pi$  – pulse polarization angle  $\beta$  was varied using a half-wave plate. The helicity of the  $\sigma$  – pulse was (a)  $\sigma^+$  and (b)  $\sigma^-$ .

# **6.5 Controlling spin reorientation with a linearly polarized pulse**

The next objective is to explore how the rotation of the linear polarization affects the final magnetization state. One pulse was circularly polarized with a fixed fluence of 80 mJ/cm² and arrived first at  $au_{
m pp} < 0$  ps. The second pump was the  $\pi$  – pulse with a fixed fluence of 80 mJ/cm<sup>2</sup> and variable orientation of the polarization plane  $(\beta)$ . A half-wave plate was used to rotate the polarization plane, oriented such that  $\beta=0^\circ$  corresponded to the initial p-polarization. Initially, measurements were carried out at a high temperature of  $T=210\mathrm{K}$ , when the  $au_{\mathrm{cr}}$  effect is absent with the  $\sigma$  – pulse helicity as  $\sigma^+$  (Fig. 6.7(a)) and  $\sigma^-$  (Fig. 6.7(b)). Since the helicity of the  $\sigma$  – pulse was kept constant in each individual diagram, the signal at  $au_{
m pp}$  <0 always has the same sign, corresponding to a monodomain saturated state  $M_{\it z}=1$  or a multidomain state with a dominating magnetization direction  $M_{\it z}<$ 1. At  $au_{
m pp}>0$ , the polarization orientation of the  $\pi$  - pulse comes into play, and the diagram is divided into equal sections at polarization intervals of roughly 90°. In half the cases, the magnetization remains positive  $(M_z>0)$ , and in the other half, it becomes negative ( $M_{z} < 0$ ). This allows us to deduce the orientation of the magnetization induced by linearly polarized light with various orientations of the polarization, similar to other studies [15,16]. Unlike these works that focused on the amplitudes and the phases of spin oscillations, in our case, it seems that the amplitude of the oscillations is less important than the phase. We observe sharp transitions in magnetization from one saturated state  $(M_z=+1)$  to another  $(M_z=-1)$  when changing eta. It is worth noting that eta chosen for the measurements resulting in Fig. 6.4(a), corresponds to the polarization which does not trigger oscillations of the spin system. This is also the polarization corresponding precisely to the transition zone from  ${M}_z=+1$  to  ${M}_z=-1.$ 

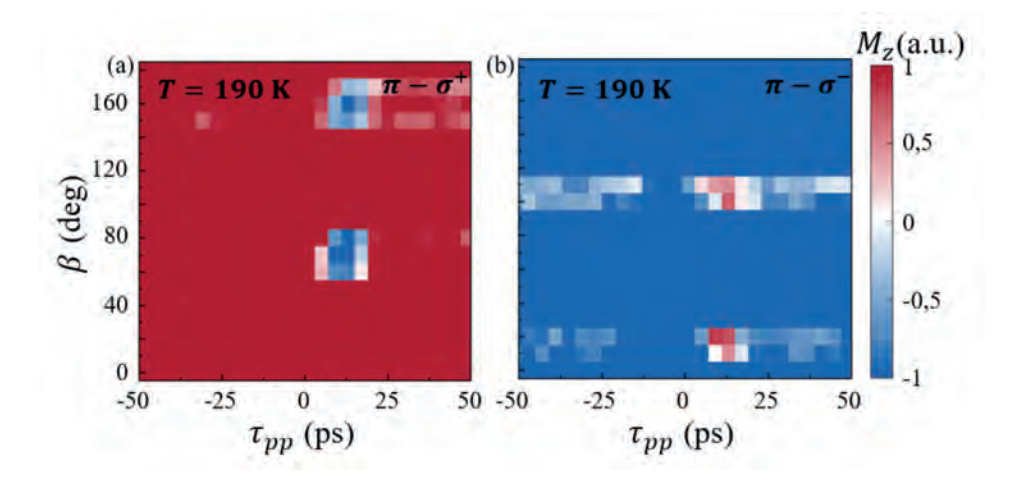


**Fig. 6.8.** Experimental diagram of the magnetization final state in coordinates of pump-pump delay  $\tau_{\rm pp}$  and orientation of the linearly polarized light  $\theta$ . The final magnetization state for the double-pump experiment with a  $\sigma$  – pulse and a  $\pi$  – pulse. The initial sample temperature was T=190 . The  $\pi$  – pulse polarization angle  $\beta$  was varied using a half-wave plate. The helicity of the  $\sigma$  – pulse was (a)  $\sigma^+$  and (b)  $\sigma^-$ .

Fig. 6.8 Experimental diagram of the magnetization final state in coordinates of pump-pump delay  $\tau_{pp}$  and orientation of the linearly polarized light  $\theta$ . The final magnetization state for the double-pump experiment with a  $\sigma$  - pulse and a  $\pi$  pulse. The initial sample temperature was T=190 K. The  $\pi$  - pulse polarization angle  $\beta$  was varied using a half-wave plate. The helicity of the  $\sigma$  - pulse was (a)  $\sigma^+$ and (b)  $\sigma^-$ .

We next examined how the polarization affects the region of the diagram (Fig. 6.4(a)) that is susceptible to  $au_{cr}$  by fixing the sample temperature at T= $190 {
m K}.$  Diagrams for the  $\sigma^+$  polarized and the  $\sigma^-$  polarized pump are shown in Fig. 6.8(a) and (b), respectively. The second pump was a  $\pi$  – pulse with a variable  $\beta$ . We observe regions where the second,  $\sigma$  – pulse does not affect the system for  $au_{
m pp}$  < $\tau_{\rm cr}$ . As the polarization angle  $\beta$  changes, these regions repeat with a period of  $90^{\circ}$ . However, compared to the diagrams for  $T=210\mathrm{K}$  (see Fig. 6.7), these regions are significantly narrower.

#### 6.6 Discussion

The study of double-pump excitation using  $\sigma$  – pulses (Chapter 5) demonstrated that the spin-reorientation transition in orthoferrite remains insensitive to the second pump pulse if the time between the two pulses is shorter than the critical time  $au_{
m pp} < au_{
m cr}$  . The value of  $au_{
m cr}$  was approximately 20 ps and was found to depend on the initial sample temperature.

In the current chapter, we observed that the system exhibits the same insensitivity to the second pump pulse, even when the polarization of the first pump pulse is linear. Moreover,  $au_{
m cr}$ , in the case of a  $\pi$  - pulse is the same as in the case of  $\sigma$  pulse – around 20 ps. However, when the first pump is a  $\sigma$  – pulse and the second pump is a  $\pi$  - pulse, we do not observe any  $\tau_{\rm cr}$ . The system, in general, does not respond to the second pulse, regardless of the time interval between the pulses.

According to the theoretical model described in Chapter 5, the thermal effect of the first pump pulse creates a potential barrier that separates the two magnetization directions perpendicular to the sample plane. It is likely that the effect of linearly polarized light on the system is insufficient in the presence of this potential barrier. Therefore, if the  $\pi$  - pulse arrives second, it does not affect the magnetic state of the system.

Circularly polarized light affects the spin system through the inverse Faraday effect (IFE), i.e., by generating an effective magnetic field along the wave vector of light. Linearly polarized light, on the other hand, acts via the inverse Cotton-Mouton effect (ICME), which induces effective anisotropy. The orientation of this induced anisotropy, and consequently magnetic dynamics, depends on both the orientation of the  $\pi$  - pulse polarization plane and the crystal structure of the sample. Thus, even at the minimum of the  $M_z$  dynamics ( $\beta=45^\circ$ , Fig. 6.2), the pump pulse excited dynamics in the XOY- plane.

Given that the critical time  $au_{
m cr}$  is the same in the experiments with two  $\sigma$  - pulses as well as with  $\sigma$  - and  $\pi$  - pulses, it can be assumed that the ICME induces magnetic dynamics as strong as those triggered by the IFE. Additionally, it is important to consider the dependence of the magnetization final state diagram on the fluence of the  $\pi$  - pulse. As seen in Figs. 6.5 and 6.6, even significant variations in the  $\pi$  - pulse fluence do not affect the value of  $\tau_{\rm cr}$ . This suggests that the value of  $\tau_{\rm cr}$  is likely intrinsic to spin dynamics in orthoferrite.

#### 6.7 Full coherent control of SRT with polarized pulses

#### 6.7.1 Experimental data

To investigate full coherent control of SRT with polarized pulses, we performed a double-pump experiment similar to that shown in Figs. 6.7 and 6.9. This time, quarter-waveplate rotation controlled the ellipticity  $\epsilon$  of one pump, while the other pump remained fixed at  $\sigma^+$  (see Fig. 6.9). The  $\sigma$  – pulse arrives first at the left part of the diagram ( $au_{
m pp} < 0$ ), the  $\epsilon$  – pulse arrives first at the right part of the diagram  $( au_{
m pp}>0)$ . The sample temperature was set to  $T=200{
m K}$ . The resulting diagram is divided into regions favoring one of the two domains,  $M_z=+1$  or  $M_z=-1$ , with transitions occurring around  $\epsilon=-0.9$  and  $\epsilon=0.3$ . Within these boundary zones, the system exhibits an insensitivity to the second pulse for  $\tau_{\rm pp} < \tau_{\rm cr}$ . Away from these boundary regions, one of the pulses always dominates, regardless of the pumping sequence or time delay.

These transitions lie close to the circular polarization  $\epsilon=-1$  or to the linear polarization  $\epsilon = 0$ . At  $\epsilon = -1$ , the linear component of the polarization changes its orientation to the orthogonal one; while at  $\epsilon = 0$ , the helicity shifts from  $\sigma^+$  to  $\sigma^-$ . In principle, these changes reverse the direction of the effective magnetic fields induced due to opto-magnetic effects (ICME, IFE) and thus yield opposite final magnetization states. A similar transition might be anticipated at  $\epsilon=0$  at the bottom part of the diagram, yet it does not appear in the data.

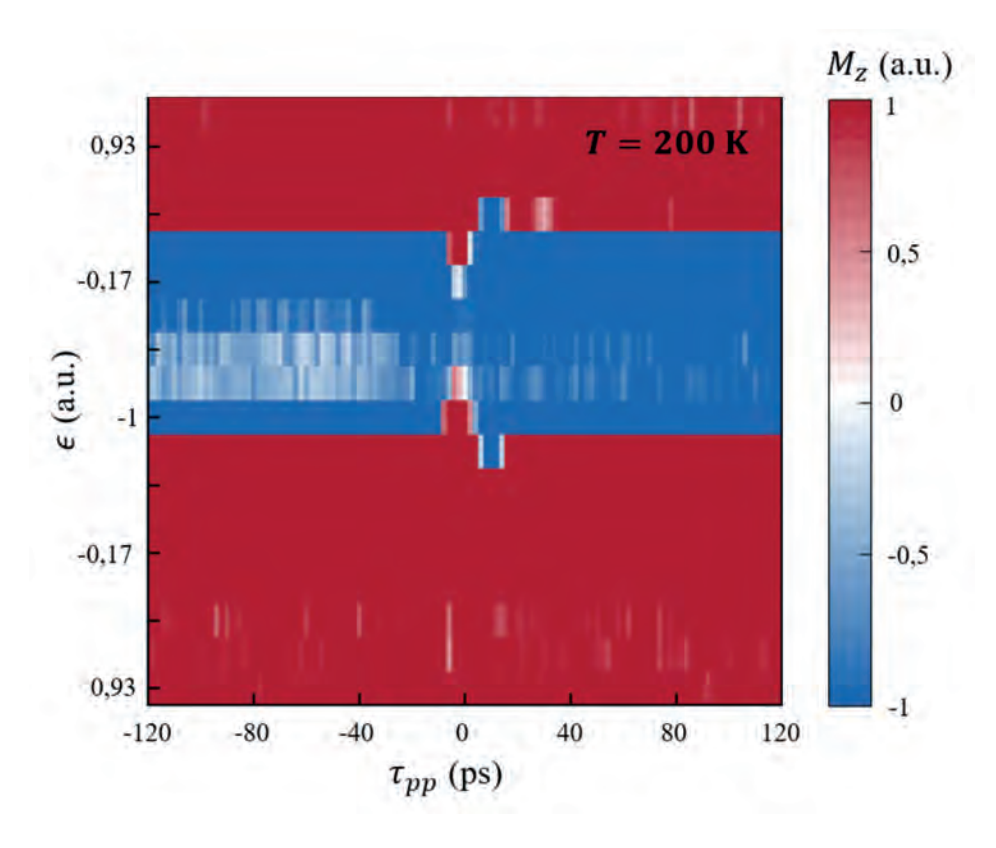


**Fig. 6.9.** Experimental diagram of the magnetization final state in coordinates of pump-pump delay  $\tau_{pp}$  and polarization of the second pump  $\epsilon$ . The helicity of the first pump was fixed as  $\sigma$ +, ellipticity  $\epsilon$  of the second pump was controlled with a quarter-waveplate. Initial temperature T = 200 .

At a lower temperature  $T=190 {\rm K}$  (see Fig. 6.10), two important details emerge. First, near at  $\epsilon < 0$ , the system's signal is nearly zero, where one could expect one more transition from  $M_z=1$  to  $M_z=-1$ . However, because our setup records the integrated signal over the illuminated sample area,  $M_z=0$  may indicate either no magnetization response or a balance of oppositely oriented domains that sum up to zero. Second, at  $\epsilon=0.5$ , we observe not only a critical time  $\tau_{\rm cr}$ , but an additional "blue" region appears for  $\tau_{\rm pp}>\tau_{\rm cr}$ . This slice in the  $\epsilon$ -diagram is shown separately in Fig. 6.10(b), with  $\epsilon=0.5$  in red and  $\epsilon=0.17$  in blue. At  $\epsilon=0.5$ , the final magnetization orientation exhibits two oscillations.

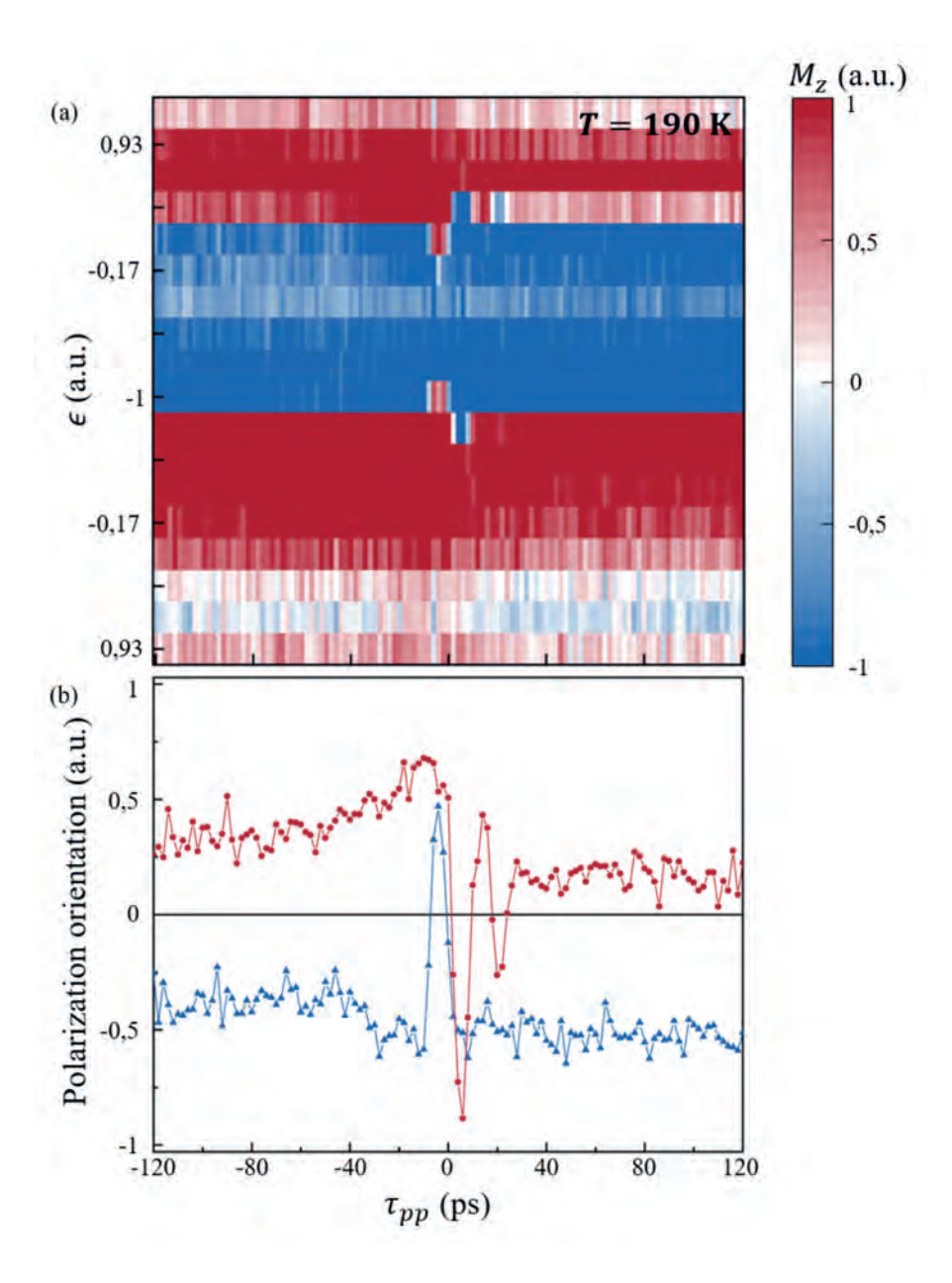


**Fig. 6.10.** (a) Experimental diagram of the magnetization final state in coordinates of pump-pump delay  $\tau_{pp}$  and polarization of the second pump  $\epsilon$ . The helicity of the first pump was fixed as  $\sigma$ +, and the ellipticity  $\epsilon$  of the second pump was controlled with a quarter-waveplate. Initial temperature T=190K. (b) Two slices of the diagram in Fig. (a) at  $\epsilon=0.17$  blue) and  $\epsilon=0.5$  red), used to emphasize the presence of the oscillations at  $\epsilon=0.5$ .

#### 6.7.2 Discussion

According to the theoretical analysis presented in Chapter 5, oscillations in the orientation of the magnetization within a newly formed domain are expected, stemming from precessional dynamics. From the experimental data, we know that the spins undergo precession after being excited by the first pump pulse. If the second pump pulse arrives at a time corresponding to a maximum in this precession, it may either facilitate or impede the transition of the system into the energy minimum with the opposite magnetization. In the geometry of our setup, we observed such a sign change in the detected signal indicating a flip in  $M_z$ .

When using two circularly polarized pulses, however, the lack of any observable precessional dynamics at delays  $\tau > 30$  ps was attributed to strong damping. Consequently, no substantial oscillation amplitude was detected at those longer time delays. In contrast, in the present measurements a clear oscillation with a period of about 20 ps arises under elliptically polarized pumping. Although these results strongly suggest a sign change in  ${\cal M}_z$ , explaining why a specific ellipticity yields a pronounced effect remains challenging. Without additional experiments, two possible scenarios can be proposed:

- 1. Non-orthogonal incidence and modified polarization The pump beams are incident on the sample at an angle of 15° from the sample normal and also pass through the cryostat window. Consequently, a purely circular beam may become elliptically polarized. If that elliptical polarization happens to be close to circular, the resulting stronger IFE could result in a stronger effective magnetic field, thus enhancing the amplitude of the precession.
- Combined influence of the IFE and ICME 2. Elliptical polarization can be viewed as a superposition of circular and linear polarization components. Accordingly, its impact on the spin system should be described by a combination of the IFE and ICME. If, at a particular polarization ellipticity, these two mechanisms cooperatively produce a stronger driving torque, the resulting precessional amplitude of the magnetization may be larger than in the purely linear or circular cases.

An additional feature in the diagram (see Fig. 6.10(a)) is the bright region corresponding to ellipticities of about 0.9 to 0.5, where the net  $M_z$  appears to be zero. Since our setup detects a spatially integrated Faraday rotation, a zero net signal can arise either from a complete absence of magnetization or from a balanced multidomain state with roughly equal areas of  $+M_z$  and  $-M_z$ .

# 6.8 Spin dynamics beyond the principle of superposition

By employing a CCD camera, we were able to visualize the nonlinear effects that arise when two pump pulses act on the sample (Fig. 6.11). The left panels show domains produced individually by the first and the second pumps when their power was set to twice the value used in the double-pulse experiment. The polarization ellipticity of the first pump is schematically indicated on the left side of the figure, while the ellipticity is listed from top to bottom at 0.77, -0.5, -1, -0.77, -0.17 and 0.93. In each case, the second pump had  $\sigma^+$  helicity, generating a

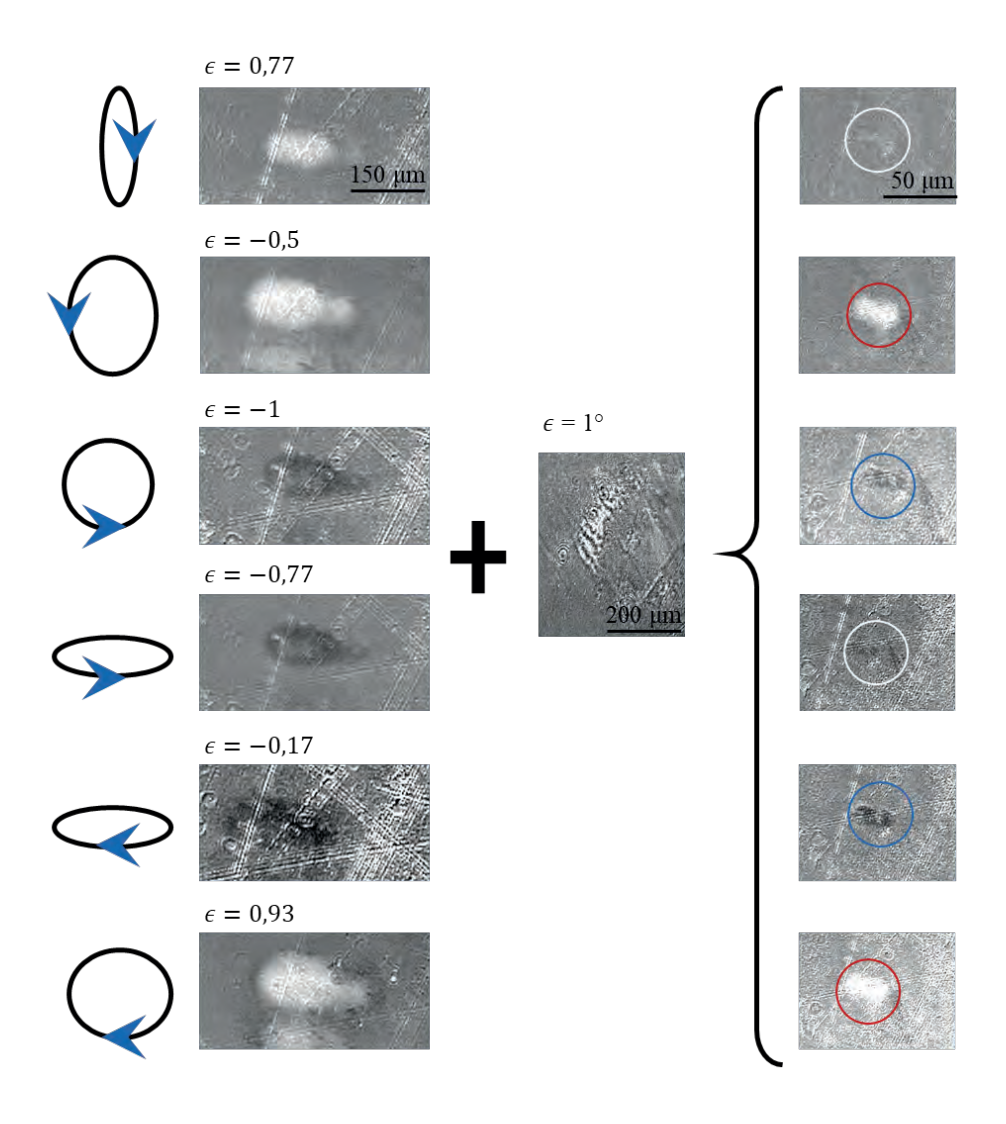


Fig. 6.11 . Ellipticity of the first pump pulse (first column), domain observed in a single-shot experiment after excitation of the high power first pump pulse (second column) and the second pump pulse (third column), and magnetic state observed in a double-pump experiment (fourth column).

white domain state ( $M_z=+1$ ). On the right, images from the double-pump experiment are displayed from a fixed pump-pump delay  $au_{
m pp}=80{
m ps}.$  We highlight with a red ring those images in which the final state is a white domain ( $M_z=+1$ ), with a blue ring those featuring a black domain ( $M_z=-1$ ), and with a white ring those showing no domain formation ( $M_z = 0$ ).

When the ellipticity  $\epsilon=\pm 0.77$  is used, the contrast of the resulting final state is negligible. We recall that all images were captured at a pump-probe delay of 1.5 ns, a timescale at which the sample temperature is expected to become stabilized. Since the pump power does not depend on its polarization ellipticity and assuming the material does not exhibit strong dichroism, the sample temperature should be approximately the same in all the cases. Consequently, the sample should be in the  $\Gamma_{24}$  phase, where the magnetization is canted out of the plane  $(M_z \ / \ 0)$  even in zero external magnetic field. Nonetheless, the system can fragment into multiple domains with  $M_z=\pm 1.$  If those domains are smaller than the detection limit of the CCD in our setup (about 0.7 micrometers per pixel), i.e. around 350 nm for half a pixel, then the measured image would average to a uniform gray level, yielding no discernible contrast.

The final set of the measurements investigated how the system switches between  $M_z=+1$  and  $M_z=-1$  under changing ellipticity pump polarization (Fig. 6.12). In this experiment, we used a single, sufficiently powerful pulse to drive the sample into the  $\Gamma_{24}$  phase, and we tuned the quarter-waveplate to explore various elliptical polarizations. The sample temperature was  $T=170\mathrm{K}$ .

- 1. Transition from  $M_z=+1$  (white) to  $M_z=-1$  (black): As  $\epsilon$  varies from -0.985 to -1, the observed domain gradually shifts from white to black, as shown in the left part of Fig. 6.12. The magnetization change begins at the domain periphery and propagates inward, effectively generating only two domains: a central white domain with  ${M}_z=+1$  and an annular black ring domain with  ${M}_z=-1.$  Further changing of  $\epsilon$  allows the ring-like domain to expand until a uniform, single domain state of  $M_z = -1$  is reached.
- 2. Transition from  ${M}_z=-1$  (black) to  ${M}_z=+1$  (white): A similar two-domain scenario occurs when the system switches back from black to white domain (see Fig. 6.12, right part). This time, a new domain emerges at the center of the illuminated spot, while the outer region remains in the initial state. As  $\epsilon$  continues to change, the central domain expands until the entire area becomes monodomain with  $M_{\it z}=$ +1.

Notably, the process is temporally symmetric. Whether switching from  $M_z=\pm 1$ to -1 or vice versa, the domain with  $M_{\it z}=+1$  consistently appears as a circular region at the center of the spot while the domain with  $M_z=-1$  manifests as a ring at the edges. Hence, these observations cannot be explained by simple thermal differences between the spot's center and its periphery. The underlying cause remains uncertain, potentially reflecting:

- Systematic deviations or alignment errors in the optical elements at higher pump power;
- Different ratio of the IFE and the ICME under varying laser intensities.

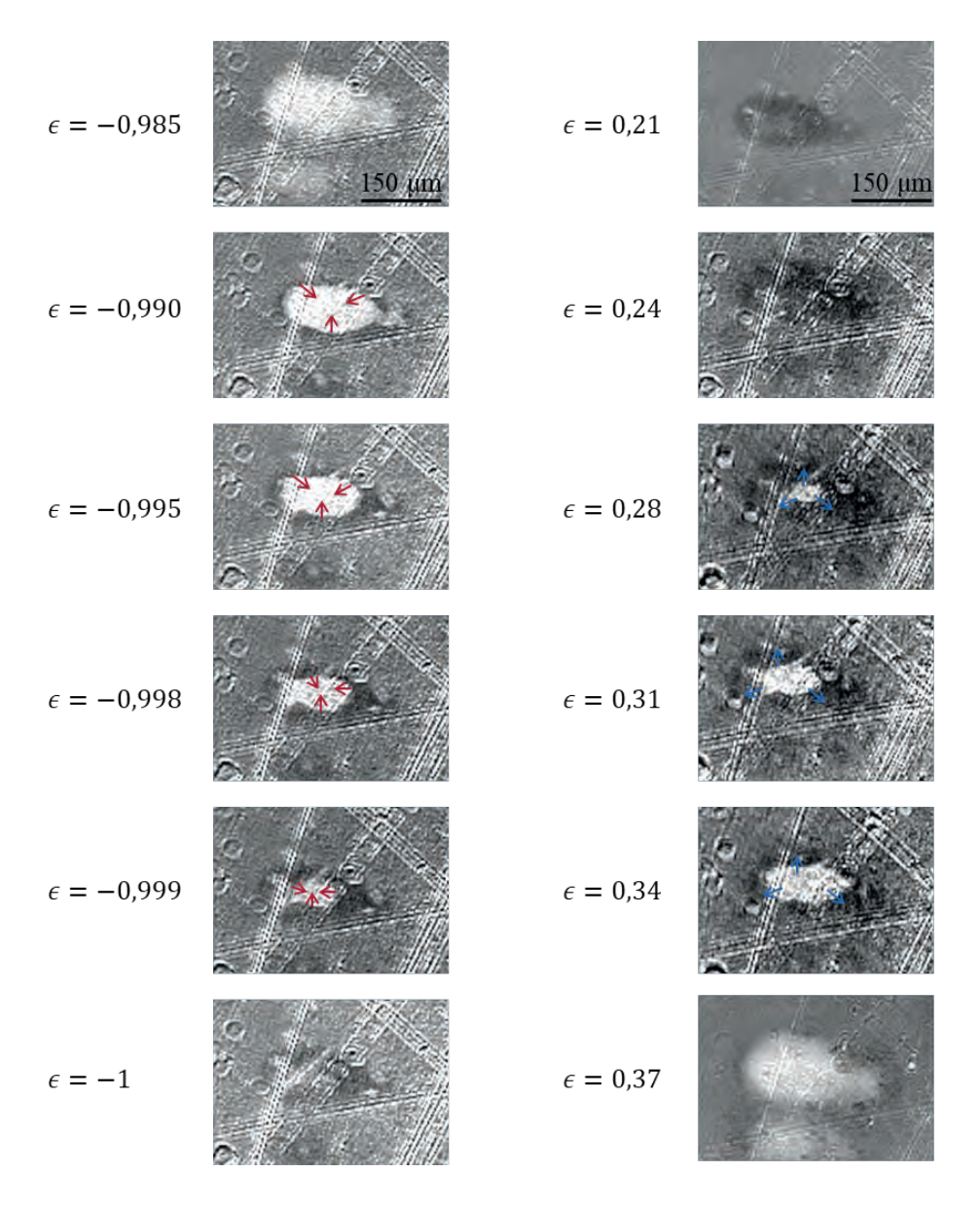


Fig. 6.12. Replacing of a white domain with a black domain (left) and a black domain with a white (right) under the changes of the pump ellipticity  $\epsilon$  in single shot experiment. The polarization of the pump changed between each pulse.

## 6.9 Conclusions

In this chapter, we investigated how linearly and elliptically polarized pump pulses can coherently control the spin reorientation phase transition (SmTb)FeO<sub>3</sub>.

When combining linear and circular polarizations, we observed the same time window of insensitivity to the second pump pulse as reported in Chapter 5. Specifically, if the second pulse arrives at a delay  $\tau_{\rm pp} < \tau_{\rm cr}$ , the system remains unaffected by its polarization, and the resulting domain magnetization is defined by that of the first pulse. Crucially, reducing or increasing the power of the linearly polarized pump pulse did not eliminate the insensitivity window.

Next, we explored how varying the orientation of the linear polarization in one of the pulses affects the final magnetization. The results revealed a  $90^{\circ}$  periodicity in the polarization dependence. This periodicity persisted even when the system was insensitive to the second pulse as  $au_{
m pp} < au_{
m cr}$ . Furthermore, if the linearly polarized pulse arrived second, its effect on the spin system was negligible.

Experiments using elliptically polarized light revealed two new phenomena. First, under specific ellipticities, we detected pronounced oscillations. Those were predicted theoretically for two circularly polarized pulses in Chapter 5. Second, at another ellipticity, the net magnetization signals vanished entirely, which we attributed to formation of a multidomain state with very small domain sizes. Employing higher resolution optical techniques or alternative detection methods such as those in the X-ray spectral range, could help to test this hypothesis.

By utilizing a CCD camera, we confirmed that the system can form either a singledomain state with a specific magnetization orientation or a multidomain state whose net magnetization is zero, depending on the ellipticity of one of the pump pulses.

Finally, more detailed single-sot experiments with fine adjustments of the ellipticity of pump pulses revealed that the transition from one magnetization direction to another does not proceed via a random multidomain state but instead goes via a concentric two-domain pattern. In such a pattern, a white (e.g.,  $M_z > 0$ ) central domain either expands or shrinks until a complete transition occurs, ultimately reaching a uniform magnetization of the opposite sign.

#### Literature

- [1] C. D. Stanciu, F. Hansteen, A. V. Kimel, A. Kirilyuk, A. Tsukamoto, A. Itoh, and T. Rasing, Alloptical magnetic recording with circularly polarized light, *Physical review letters* 99 **(4)**, 047601 (2007).
- [2] T. Satoh *et al.*, Spin oscillations in antiferromagnetic NiO triggered by circularly polarized light, *Physical Review Letters* 105 **(7)**, 077402 (2010).
- [3] T. Satoh, Y. Terui, R. Moriya, B. A. Ivanov, K. Ando, E. Saitoh, T. Shimura, and K. Kuroda, Directional control of spin-wave emission by spatially shaped light, *Nature Photonics* 6 (10), 662-666 (2012).
- [4] S. Mangin *et al.*, Engineered materials for all-optical helicity-dependent magnetic switching, *Nature materials* 13 **(3)**, 286-292 (2014).
- [5] C.-H. Lambert *et al.*, All-optical control of ferromagnetic thin films and nanostructures, *Science* 345 **(6202)**, 1337-1340 (2014).
- [6] G. Kichin, M. Hehn, J. Gorchon, G. Malinowski, J. Hohlfeld, and S. Mangin, From multiple-to single-pulse all-optical helicity-dependent switching in ferromagnetic Co/Pt multilayers, *Physical Review Applied* 12 (2), 024019 (2019).
- [7] T. Cornelissen, R. Córdoba, and B. Koopmans, Microscopic model for all optical switching in ferromagnets, *Applied Physics Letters* 108 **(14)** (2016).
- [8] J. Gorchon, Y. Yang, and J. Bokor, Model for multishot all-thermal all-optical switching in ferromagnets, *Physical Review B* 94 **(2)**, 020409 (2016).
- [9] A. Khorsand, M. Savoini, A. Kirilyuk, A. Kimel, A. Tsukamoto, A. Itoh, and T. Rasing, Role of magnetic circular dichroism in all-optical magnetic recording, *Physical review letters* 108 (12), 127205 (2012).
- [10] Y. Tsema, G. Kichin, O. Hellwig, V. Mehta, A. Kimel, A. Kirilyuk, and T. Rasing, Helicity and field dependent magnetization dynamics of ferromagnetic Co/Pt multilayers, Applied Physics Letters 109 (7) (2016).
- [11] W. Jiang et al., Direct imaging of thermally driven domain wall motion in magnetic insulators, *Physical review letters* 110 **(17)**, 177202 (2013).
- [12] R. Medapalli *et al.*, Multiscale dynamics of helicity-dependent all-optical magnetization reversal in ferromagnetic Co/Pt multilayers, *Physical Review B* 96 **(22)**, 224421 (2017).
- [13] R. John *et al.*, Magnetisation switching of FePt nanoparticle recording medium by femtosecond laser pulses, *Scientific reports* 7 **(1)**, 4114 (2017).
- [14] V. López-Flores, J. Arabski, C. Stamm, V. Halté, N. Pontius, E. Beaurepaire, and C. Boeglin, Time-resolved x-ray magnetic circular dichroism study of ultrafast demagnetization in a CoPd ferromagnetic film excited by circularly polarized laser pulse, *Physical Review B* 86 (1), 014424 (2012).

- [15] A. Kalashnikova, A. Kimel, R. Pisarev, V. Gridnev, A. Kirilyuk, and T. Rasing, Impulsive generation of coherent magnons by linearly polarized light in the easy-plane antiferromagnet FeBO 3, Physical review letters 99 (16), 167205 (2007).
- [16] A. Kalashnikova, A. Kimel, R. Pisarev, V. Gridnev, P. Usachev, A. Kirilyuk, and T. Rasing, Impulsive excitation of coherent magnons and phonons by subpicosecond laser pulses in the weak ferromagnet FeBO 3, Physical Review B 78 (10), 104301 (2008).
- [17] L. Shen, L. Zhou, J. Shi, M. Tang, Z. Zheng, D. Wu, S. Zhou, L. Chen, and H. Zhao, Dominant role of inverse Cotton-Mouton effect in ultrafast stimulation of magnetization precession in undoped yttrium iron garnet films by 400-nm laser pulses, Physical Review B 97 (22), 224430 (2018).
- [18] E. Beaurepaire, J.-C. Merle, A. Daunois, and J.-Y. Bigot, Ultrafast spin dynamics in ferromagnetic nickel, Physical review letters 76 (22), 4250 (1996).
- [19] L. Soumah, D. Bossini, A. Anane, and S. Bonetti, Optical Frequency Up-Conversion of the Ferromagnetic Resonance in an Ultrathin Garnet Mediated by Magnetoelastic Coupling, Physical review letters 127 (7), 077203 (2021).
- [20] F. Hansteen, A. Kimel, A. Kirilyuk, and T. Rasing, Nonthermal ultrafast optical control of the magnetization in garnet films, Physical Review B 73 (1), 014421 (2006).
- [21] T. Ostler et al., Ultrafast heating as a sufficient stimulus for magnetization reversal in a ferrimagnet, Nature communications 3 (1), 666 (2012).
- [22] M. S. El Hadri, P. Pirro, C.-H. Lambert, S. Petit-Watelot, Y. Quessab, M. Hehn, F. Montaigne, G. Malinowski, and S. Mangin, Two types of all-optical magnetization switching mechanisms using femtosecond laser pulses, Physical Review B 94 (6), 064412 (2016).
- [23] L. Pitaevskii, Electric forces in a transparent dispersive medium, Sov. Phys. JETP 12 (5), 1008-1013 (1961).
- [24] P. Pershan, JP Van der ziel, and LD Malmstrom, Phys. Rev 143, 574 (1966).
- [25] D. Popova, A. Bringer, and S. Blügel, Theory of the inverse Faraday effect in view of ultrafast magnetization experiments, Physical Review B 84 (21), 214421 (2011).
- [26] A. Kimel, A. Kirilyuk, P. Usachev, R. Pisarev, A. Balbashov, and T. Rasing, Ultrafast non-thermal control of magnetization by instantaneous photomagnetic pulses, Nature 435 (7042), 655-657 (2005).
- [27] M. Berritta, R. Mondal, K. Carva, and P. M. Oppeneer, Ab initio theory of coherent laser-induced magnetization in metals, Physical review letters 117 (13), 137203 (2016).
- [28] X. Lu et al., Roles of heating and helicity in ultrafast all-optical magnetization switching in TbFeCo, Applied Physics Letters 113 (3) (2018).
- [29] E. B. Alexandrov and V. S. Zapasskii, Laser magnetic spectroscopy, (1986).

[30] Y. Quessab, R. Medapalli, M. El Hadri, M. Hehn, G. Malinowski, E. Fullerton, and S. Mangin, Helicity-dependent all-optical domain wall motion in ferromagnetic thin films, *Physical Review B* 97 **(5)**, 054419 (2018).

# Summary

During the last two decades, the world leaders in the magnetic recording industry – Seagate and Western Digital – have been working on Heat-Assisted Magnetic Recording (HAMR). Today, HAMR hard drives are already entering the market. Which technology will be the next challenge in the field, and what the recording industry will work on after HAMR, are questions that are increasingly often being asked. Heat-Assisted Magnetic Recording employs the ferromagnetic metal FePt as a recording medium. Dielectric materials have very low electrical conductivity and, consequently, substantially lower heat conductivity than metals. As a result, heat-diffusion, which affects bit size, is expected to be a significantly smaller problem for HAMR using a dielectric recording medium than for HAMR employing metals. Ferri- and antiferromagnets are known to have much faster spin dynamics than ferromagnets. Hence, in the search for revolutionary new solutions, it is natural to explore the possibilities of heat-assisted control of spins in ferri- and antiferromagnetic dielectrics. This thesis addresses exactly that problem.

In particular, we experimentally investigate spin dynamics triggered in ferri- and antiferromagnetic dielectrics using femtosecond laser pulses and a pump-probe technique. First, because the media absorb light, such pulses act as ultrafast heaters. Secondly, due to opto-magnetic effects, when the pulses are properly polarized, they act as equally short pulses of effective magnetic field.

Polarization microscopy was the primary method used to probe the magnetic state of the studied magnets. With this technique we were able to obtain images of the magnetic domains as well as diffraction patterns of light scattered by these domains. Using femtosecond laser pulses as ultrashort flashes of light, we were able to capture magneto-optical snapshots of the studied samples. By varying the delay between the pump and probe pulses, we took snapshots at different time delays after the pump pulse, thereby revealing the pump-induced dynamics of the magnetic domains.

The first half of this thesis focuses on thin films of ferrimagnetic iron garnets. Initially, we investigated the laser-induced motion of domain walls. To monitor domain wall displacements with femtosecond temporal and nanometer spatial resolution, we developed a setup based on the diffraction of femtosecond laser pulses by the magnetic domain. We showed that this approach enabled us to detect domain wall displacements up to 6 nm with a temporal resolution of 100 fs.

In Chapter 4, for instance, we studied HAMR scenarios in the iron garnet. In particular, we explored the efficiency of HAMR by varying the sample temperature,

the magnitude of the external magnetic field, and the pump fluence. Experimentally, it was demonstrated that magnetization switching is achievable only within a narrow range of these parameters. For instance, an increase in the initial sample temperature requires a reduction in the applied magnetic field. Alongside these experiments, theoretical modeling was presented to define the range of external parameters within which magnetization switching is feasible. The possibility of switching is directly linked to the height of the potential barrier separating the two-bit states with opposite magnetization. This potential barrier depends on both the initial temperature and the external magnetic field. It must be sufficiently low to allow switching; however, if the barrier is too small, the stability of the two magnetization states is broken, rendering switching impossible.

The second part of this thesis explores the coherent control of the spinreorientation transition (SRT) in the antiferromagnetic mixed orthoferrite (SmTb)FeO<sub>3</sub> Using double pulse excitation i.e. performing pump-pump-probe experiments, we demonstrate that by changing the fluences, polarizations, and delay between the pulses, we can control the final state of the pump-pumpinduced spin dynamics. Interestingly, we discovered that right after the excitation of the antiferromagnet with the first pump pulse, it remains insensitive to the second pulse for delays of about 20 ps. This interval does not depend on the pulse polarization or its power; instead, it appears to be determined by intrinsic parameters of the orthoferrite. This finding reveals a fundamental limit on the rate of optical control of magnetism in this antiferromagnet.

To conclude, this thesis demonstrates various scenarios and mechanisms that may potentially be realized for HAMR on dielectric ferri- and antiferromagnetic media. Many of the phenomena discussed in this thesis had not been predicted before and were initially quite puzzling. Although we resolve these puzzles by suggesting appropriate approximations and simple theoretical models, the research has led to many more interesting questions regarding HAMR in dielectric ferri- and antiferromagnets. What are the routes for the fastest and most energy-efficient writing of magnetic bits? Which electronic, photonic, or magnonic excitations - or combinations thereof - allow one to steer spins in dielectric ferri- and antiferromagnets along these routes? What is the smallest bit that can be written on a ferri- and/or antiferromagnetic dielectric? In any case, it is clear that the physics of HAMR, employing ferromagnetic metals, is quite different from that of HAMR aiming to use ferri- or antiferromagnetic dielectrics. We expect that in the coming years, these research questions and the broader topic of HAMR on dielectric ferri- and antiferromagnets will attract much more attention in the field of ultrafast magnetism.

# Samenvatting

Tijdens de afgelopen twee decennia hebben de wereldleiders in de magnetische opname-industrie - Seagate en Western Digital - gewerkt aan Heat-Assisted Magnetic Recording (HAMR). Tegenwoordig komen HAMR-harddrives al op de markt. Welke technologie de volgende uitdaging zal vormen en waar de opname-industrie na HAMR aan zal werken, zijn vragen die steeds vaker worden gesteld. Heat-Assisted Magnetic Recording maakt gebruik van het ferromagnetische metaal FePt als opname-medium. Dielektrische materialen hebben een zeer lage elektrische geleidbaarheid en bijgevolg een aanzienlijk lagere warmtegeleiding dan metalen. Hierdoor wordt verwacht dat warmteverspreiding, wat de bitgrootte beïnvloedt, een aanzienlijk kleiner probleem zal vormen voor HAMR met een dielektrisch opname-medium dan voor HAMR met metalen. Ferri- en antiferromagneten staan bekend om hun veel snellere spindynamica in vergelijking met ferromagneten. Daarom is het in de zoektocht naar revolutionaire nieuwe oplossingen vanzelfsprekend om de mogelijkheden te onderzoeken voor warmte-ondersteunde controle van spins in ferri- en antiferromagnetische dielektrica. Deze scriptie pakt precies dat probleem aan.

In het bijzonder onderzoeken we experimenteel de spindynamica die wordt opgewekt in ferri- en antiferromagnetische dielektrica met behulp van femtoseconde laserpulsen en een pump-probe techniek. Ten eerste werken deze pulsen, doordat de media licht absorberen, als ultrasnelle verwarmingselementen. Ten tweede, door opto-magnetische effecten, fungeren de pulsen – wanneer ze correct gepolariseerd zijn – als even korte pulsen van een effectief magnetisch veld.

Polarisatiemicroscopie werd als primaire methode gebruikt om de magnetische toestand van de bestudeerde magneten te onderzoeken. Met deze techniek konden we beelden verkrijgen van de magnetische domeinen evenals diffractiepatronen van licht dat door deze domeinen werd verstrooid. Door femtoseconde laserpulsen als ultrakorte lichtflitsen te gebruiken, konden we magneto-optische momentopnames van de bestudeerde monsters vastleggen. Door de vertraging tussen de pump- en probepulsen te variëren, maakten we momentopnames bij verschillende tijdsvertragingen na de pump-puls, waardoor de pump-geïnduceerde dynamiek van de magnetische domeinen zichtbaar werd.

Het eerste deel van deze scriptie richt zich op dunne films van ferrimagnetische ijzergarnetten. Aanvankelijk onderzochten we door laser geïnduceerde beweging van domeinwanden. Om domeinwandverplaatsingen met femtoseconde temporele en nanometer-ruimtelijke resolutie te monitoren, ontwikkelden we een opstelling gebaseerd op de diffractie van femtoseconde laserpulsen door magnetische

domeinen. We toonden aan dat deze benadering ons in staat stelde domeinwandverplaatsingen tot 6 nm te detecteren met een temporele resolutie van 100 fs.

In hoofdstuk 4 bestudeerden we bijvoorbeeld HAMR-scenario's in de ijzergarnet. In het bijzonder onderzochten we de efficiëntie van HAMR door de temperatuur van het monster, de sterkte van het externe magnetische veld en de pump-fluence te variëren. Experimenteel werd aangetoond dat magnetisatieschakeling alleen binnen een smal bereik van deze parameters haalbaar is. Zo vereist een verhoging van de initiële monster temperatuur een verlaging van het toegepaste magnetische veld. Naast deze experimenten werd theoretische modellering gepresenteerd om bereik definiëren het van externe parameters te waarbinnen magnetisatieschakeling mogelijk is. De mogelijkheid tot schakeling is direct gekoppeld aan de hoogte van de potentiële barrière die de twee bittoestanden met tegenovergestelde magnetisatie scheidt. Deze potentiële barrière is afhankelijk van zowel de initiële temperatuur als het externe magnetische veld. Ze moet voldoende laag zijn om schakeling toe te laten; als de barrière echter te klein is, wordt de stabiliteit van de twee magnetisatietoestanden opgeheven, waardoor schakeling onmogelijk wordt.

Het tweede deel van deze scriptie onderzoekt de coherente controle van de spinreoriëntatietransitie (SRT) in de antiferromagnetische gemengde orthoferriet (SmTb)FeO3. Met behulp van dubbele puls excitatie, oftewel pump-pump-probe experimenten, tonen we aan dat door het veranderen van de fluences, polarisaties en de vertraging tussen de pulsen, we de uiteindelijke staat van de door pumppump geïnduceerde spindynamica kunnen beheersen. Opmerkelijk is dat we ontdekten dat direct na de excitatie van de antiferromagneet met de eerste pumppuls, deze gedurende ongeveer 20 ps ongevoelig blijft voor de tweede puls. Dit interval is niet afhankelijk van de puls-polarisatie of -kracht; in plaats daarvan lijkt het te worden bepaald door intrinsieke parameters van de orthoferriet. Deze bevinding onthult een fundamentele limiet voor de snelheid van optische controle over de magnetisme in deze antiferromagneet.

Samenvattend demonstreert deze scriptie diverse scenario's en mechanismen die potentieel gerealiseerd kunnen worden voor HAMR op dielektrische ferri- en antiferromagnetische media. Veel van de in deze scriptie besproken fenomenen waren eerder niet voorspeld en waren aanvankelijk behoorlijk verwarrend. Hoewel we deze raadsels oplossen door geschikte benaderingen en eenvoudige theoretische modellen voor te stellen, heeft het onderzoek geleid tot vele andere interessante vragen met betrekking tot HAMR in dielektrische ferri- en

antiferromagneten. Wat zijn de routes voor het snelst en meest energie-efficiënt schrijven van magnetische bits? Welke elektronische, fotonische of magnonische excitatie – of combinaties daarvan – stelt ons in staat om spins in dielektrische ferri- en antiferromagneten in deze richtingen te sturen? Wat is de kleinste bit die kan worden geschreven op een ferri- en/of antiferromagnetische dielektrica? Hoe dan ook, het is duidelijk dat de fysica van HAMR met ferromagnetische metalen aanzienlijk verschilt van die van HAMR dat gericht is op ferri- of antiferromagnetische dielektrica. We verwachten dat deze onderzoeksvragen, en het bredere onderwerp van HAMR op dielektrische ferri- en antiferromagneten, de komende jaren veel meer aandacht zullen krijgen binnen het veld van ultrasnelle magnetisme.

.

# Research Data Management

This thesis research has been carried out in accordance with the research data management policy of the Institute for Molecules and Materials (IMM) of Radboud University, the Netherlands.<sup>1</sup> The following datasets have been produced during the research:

- Chapter 3: A. Dolgikh, T.B. Shapaeva, K.T. Yamada, M.V. Logunov, T.H. Rasing and A.V. Kimel, Magneto-optical diffraction of visible light as a probe of nanoscale discplacement of domain walls at femtosecond timescales, Review of Scientific Instruments 94(10), 2023. https://doi.org/ 10.1063/5.0152670.
  - CNCZ, Radboud University (2025). \uscm-ssi-srv.science.ru.nl\uscm-ssi2\Alexander Dolgikh\Upload\Project 1 Diffraction
- Chapter 4: A. Dolgikh, D. Afanasiev, V.V. Yurlov, M.V. Logunov, A.K. Zvezdin and A.V. Kimel, Ultrafast heat-assisted magnetization dynamics in a ferrimagnetic insulator, *Phys. Rev. B* 107(9), 094424, 2023. https://doi.org/ 10.1103/PhysRevB.107.094424.
  - CNCZ, Radboud University (2025). \\uscm-ssi-srv.science.ru.nl\uscm-ssi2\Alexander Dolgikh\Upload\Project 2 HAMR
- Chapter 5: N.E. Khokhlov, A.E. Dolgikh, B.A. Ivanov and A.V. Kimel "Double pulse all-optical coherent control of ultrafast spin-reorientation in antiferromagnetic rare-earth orthoferrite" APL Materials 12(5), 2024. https:// doi.org/10.1063/5.0197976.
  - CNCZ, Radboud University (2025). \uscm-ssi-srv.science.ru.nl\uscm-ssi2\Alexander Dolgikh\Upload\Project 3 double pump
- Chapter 6: CNCZ, Radboud University (2025). \uscm-ssi-srv.science.ru.nl\uscm-ssi2\Alexander Dolgikh\Upload\Project 3 double pump

# **List of Publications**

- N.E. Khokhlov, A.E. Dolgikh, B.A. Ivanov, A.V. Kimel, "Double pulse all-optical coherent control of ultrafast spin-reorientation in antiferromagnetic rare-earth orthoferrite", APL Materials, 12 (5), 051119 (2024).
- [2] **A. Dolgikh**, T.B. Shapaeva, K.T. Yamada, M.V. Logunov, T.H. Rasing, A.V. Kimel, "Magneto-optical diffraction of visible light as a probe of nanoscale displacement of domain walls at femtosecond timescales", *Review of Scientific Instruments*, 94(**10**), 103001 (2023).
- [3] **A. Dolgikh**, D. Afanasiev, V.V. Yurlov, M.V. Logunov, A.K. Zvezdin, A.V. Kimel, "Ultrafast heat-assisted magnetization dynamics in a ferrimagnetic insulator", *Physical Review B*, 107(**9**), 094424 (2023).

# Curriculum Vitae



Name: Alexander Evgenievich Dolgikh

**Date of birth**: 17/03/1995 **Nationality**: Russian

E-mail: sane4ekup@gmail.com

2019 – 2024 **PhD** in Physics, Radboud University, Nijmegen

2016 – 2018 **MSc** in Physics, Moscow Institute of Physics Technology, Moscow

2012 – 2016 **BSc** in Physics, Moscow State University, Moscow

2008 – 2012 School, School №218, Moscow

2001 – 2008 School, School №240, Moscow

